

Wright State University

CORE Scholar

[Browse all Theses and Dissertations](#)

[Theses and Dissertations](#)

2016

Development, Design, Manufacture and Test of Flapping Wing Micro Aerial Vehicles

Todd J. Smith
Wright State University

Follow this and additional works at: https://corescholar.libraries.wright.edu/etd_all



Part of the [Engineering Commons](#)

Repository Citation

Smith, Todd J., "Development, Design, Manufacture and Test of Flapping Wing Micro Aerial Vehicles" (2016). *Browse all Theses and Dissertations*. 1695.
https://corescholar.libraries.wright.edu/etd_all/1695

This Dissertation is brought to you for free and open access by the Theses and Dissertations at CORE Scholar. It has been accepted for inclusion in Browse all Theses and Dissertations by an authorized administrator of CORE Scholar. For more information, please contact library-corescholar@wright.edu.

Development, Design, Manufacture and Test of Flapping Wing Micro Aerial Vehicles

A dissertation submitted in partial fulfillment
of the requirements for the degree of
Doctor of Philosophy

by

TODD J. SMITH
B.S.M.E., Wright State University, 2010
M.S.Egr., Wright State University, 2013

2016
WRIGHT STATE UNIVERSITY

WRIGHT STATE UNIVERSITY
GRADUATE SCHOOL

November 22, 2016

I HEREBY RECOMMEND THAT THE DISSERTATION PREPARED UNDER MY SUPERVISION BY Todd J. Smith ENTITLED Development, Design, Manufacture and Test of Flapping Wing Micro Aerial Vehicles BE ACCEPTED IN PARTIAL FULFILLMENT OF THE REQUIREMENTS FOR THE DEGREE OF Doctor of Philosophy.

George Huang, Ph.D., P.E.
Dissertation Director

Frank W. Ciarallo, Ph.D.
Director, Ph.D. in Engineering Program

Robert E. W. Fyffe, Ph.D.
Vice President for Research and
Dean of the Graduate School

Committee on
Final Examination

George Huang, Ph.D., P.E.

James Menart, Ph.D.

Zifeng Yang, Ph.D.

Richard Cobb, Ph.D.

Michael Oppenheimer, Ph.D.

ABSTRACT

Smith, Todd J., Ph.D., Engineering Ph.D. Program, Department of Mechanical and Materials Engineering, Wright State University, 2016. *Development, Design, Manufacture and Test of Flapping Wing Micro Aerial Vehicles*.

The field of Flapping Wing Micro Air Vehicles (FWMAV) has been of interest in recent years and as shown to have many aerodynamic principles unconventional to traditional aviation aerodynamics. In addition to traditional manufacturing techniques, MAVs have utilized techniques and machines that have gained significant interest and investment over the past decade, namely in additive manufacturing. This dissertation discusses the techniques used to manufacture and build a 30 gram-force (gf) model which approaches the lower limit allowed by current commercial off-the-shelf items. The vehicle utilizes a novel mechanism that minimizes traditional kinematic issues associated with four bar mechanisms for flapping wing vehicles. A kinematic reasoning for large amplitude flapping is demonstrated namely, by lowering the cycle averaged angular acceleration of the wings. The vehicle is tested for control authority and lift of the mechanism using three servo drives for wing manipulation. The study then discusses the wing design, manufacturing techniques and limitations involved with the wings for a FWMAV. A set of 17 different wings are tested for lift reaching lifts of 38 gf using the aforementioned vehicle design. The variation in wings spurs the investigation of the flow patterns generated by the flexible wings and its interactions for multiple flapping amplitudes. Phase-lock particle image velocimetry (PIV) is used to investigate the unsteady flows generated by the vehicle. A novel flow pattern is experimentally found, namely “trailing edge vortex capture” upon wing reversal for all three flapping amplitudes, alluding to a newly discovered addition to the lift enhancing effect of wake capture. This effect is believed to be a result of flexible wings and may provide lift enhancing characteristics to wake capture.

List of Symbols

α	Angle of Attack
β	Control Mechanism Angle
C_L	Coefficient of Lift
C_D	Coefficient of Drag
δ_{LW}	Left Wing Control Input
δ_{RW}	Right Wing Control Input
F_x	Vertical Force
F_y	Spanwise or Side Force
F_z	Axial Force
\bar{F}_x	Cycle Averaged Vertical Force
\bar{F}_y	Cycle Averaged Spanwise or Side Force
\bar{F}_z	Cycle Averaged Axial Force
γ	Flapping Plane Angle
I_A	Wing Second Moment of Area
M_x	Yaw Moment
M_y	Pitch Moment
M_z	Roll Moment
\bar{M}_x	Cycle Averaged Yaw Moment
\bar{M}_y	Cycle Averaged Pitch Moment
\bar{M}_z	Cycle Averaged Roll Moment
ρ	Density of Air
ϕ	Wing Position
$\dot{\phi}$	Wing Angular Velocity
$\ddot{\phi}$	Wing Angular Acceleration
ω	Flapping Frequency

Contents

1	INTRODUCTION	1
1.1	Introduction	1
1.2	Purpose	2
1.3	Literature Review	2
1.3.1	Fixed Wing Flight	3
1.3.2	Rotor Craft Flight	4
1.3.3	Flapping Wing Flight	6
1.3.4	Flight in Nature	9
1.3.5	Insect Wing Investigations	14
1.4	Conclusions	17
1.5	Original Contributions and Organization of Dissertation	18
2	DESIGN PRINCIPLES	20
2.1	Introduction	20
2.2	Electro-Mechanical Actuation	20
2.3	Power Sources	25
2.4	Transmitters and Receivers	26
2.5	Gearing and Power Transmission	27
2.6	Basic Building Materials	27
2.7	Four-Bar Mechanisms	29
2.8	Computer Aided Design (CAD)	31
2.9	Summary	32
3	DESIGN	33
3.1	Introduction	33
3.2	Inspiration	34
3.3	Evolution of a Horizontal Flapper	36
3.3.1	Achieving Large Flapping Angles	37
3.3.2	Vehicle Kinematics	40
3.3.3	Pitch Controllable 180 Degree Amplitude Flapper	45
3.3.4	Version 2 Lift Off	47
3.3.5	Mechanical Design	48

3.3.6	Taking Control: Addition of Independent Angle of Attack Control .	56
3.3.7	Taking Control: Addition of Roll Control	67
3.3.8	Collaboration with AFRL: Combining Novel Drive Mechanism with Split Cycle Control Scheme	70
3.4	Summary	71
4	WING DEVELOPMENT	73
4.1	Learning From Nature	73
4.2	Coalesced Wing Design	76
4.3	Wing Design and Manufacture	77
4.4	Sizing and Stiffness Considerations	79
4.5	Summary	80
5	EXPERIMENTAL TESTING	81
5.1	Introduction	81
5.2	Load Cell Testing	82
5.2.1	Experimental Setup	82
5.2.2	Experimental Results	84
5.2.3	Experimental Conclusions	98
5.3	Phase-Lock Particle Image Velocimetry (PIV)	99
5.3.1	Experimental Setup	100
5.3.2	Experimental Results	102
5.3.3	Experimental Conclusions	141
6	CONCLUSION	142
6.1	Research Contributions	143
6.2	Recommendations for Future Work	144
	Bibliography	145
A	Appendix A	154
A.1	Wing AOA Tracking Plots	154
A.2	Wing Velocity Plots	160
B	Appendix B	167
B.1	Four-Bar MATLAB Code	167

List of Figures

1.1	Fixed Wing Micro Air Vehicles	3
1.2	Micro Helicopters	4
1.3	Quadrotor Platforms	5
1.4	Harvard RoboBee and Wing, from Ref [34]	8
1.5	Cicada Wing Tip Path, from Wan [55]	13
2.1	Electromagnetic Actuators	23
2.2	Blade Coreless Motors	24
2.3	Servo Actuators	25
2.4	10 mAh Full River Battery [4]	25
2.5	Metal Gear Train	28
2.6	Types of Four Bar Linkages [75]	30
3.1	Ladybug Flapping Cycle	35
3.2	Rocker Linkage Drives the Wings Stroke Rotation [77]	37
3.3	Conceptual Sketch of Mechanism	38
3.4	Double Sided Bevel Gear Sets	39
3.5	Four Bar Linkage Incremental Geometry	41
3.6	Mechanism Kinematics, Crank Angle vs. Normalized Wing Angle	42
3.7	Angular Velocity and Acceleration of Rocker Arm	42
3.8	Normalized Angular Position of Larger Amplitude Mechanisms	43
3.9	Normalized Absolute Value Angular Velocity of Larger Amplitude Mechanisms	43
3.10	Normalized Absolute Value Angular Acceleration of Larger Amplitude Mechanisms	43
3.11	Mechanism Kinematics for Flapping Amplitudes and Frequencies	45
3.12	Version 1 of Horizontal Flapper	46
3.13	Snapshots of High Speed Video of Tethered Flight	48
3.14	Horizontal Flapper Dimensions	49
3.15	Isometric Sectioned View of Horizontal Flapper	50
3.16	Flapper Gear Train	51
3.17	Flapper Gear Train	52
3.18	Bevel Gear Set Dimension, Side View	53

3.19	Bevel Gear Set Dimension, Top View	53
3.20	224 Tooth Gear	54
3.21	224 Tooth Sector Gear	55
3.22	20 Tooth Gear	55
3.23	20 tooth sector gear	56
3.24	CAD Model Demonstrating 180 Degrees of Flapping	58
3.25	Angle of Attack controlled Flapper on a Nano-17 Load Cell	59
3.26	Angle of Attack Control Concept	59
3.27	Angle of Attack Control CAD	60
3.28	Angle of Attack Plotted on Wing Angle vs. Control Angle (Idealized)	61
3.29	CAD of Modified Angle of Attack Control Mechanism	61
3.30	Modified Angle of Attack Control Mechanism	62
3.31	Vehicle Coordinate System	65
3.32	Simulated Z-Direction Trim Results	66
3.33	Simulated Trim and Non-Trim M_y Moment	66
3.34	Wing Lift Reduction due to Wing Bending	68
3.35	Roll Control Model	68
3.36	Roll Control Servo	69
3.37	Roll Control Trim Adjustment	70
3.38	Two Motor Design with Full Aluminum Chassis and Gears [79]	72
4.1	Comstock-Needham System [80]	74
4.2	Insect Wing Division	75
4.3	Coalesced Wing Design [66]	77
4.4	Wing Layup and Cure	79
5.1	AOA Adjustment Vehicle Load Cell Results	85
5.2	Strobe Light Foam Wing at 3V	87
5.3	Wing Lift Testing Results [83]	90
5.4	Wing 2D AOA Mapping	93
5.5	Wing 2E AOA Mapping	95
5.6	Wing 2F AOA Mapping	96
5.7	Wing 2H AOA Mapping	97
5.8	Phase-Lock PIV Schematic	101
5.9	Mechanism Kinematics for Flapping Amplitudes and Frequencies	103
5.10	PIV Wing Locations	104
5.11	PIV Wing Locations	105
5.12	PIV 30° in 180 Amplitude Vorticity	106
5.13	PIV 15° in 180 Amplitude Vorticity	107
5.14	PIV 0° in 180 Amplitude Vorticity	108
5.15	PIV 0° out 180 Amplitude Vorticity	109
5.16	PIV 15° out 180 Amplitude Vorticity	110
5.17	PIV 30° out 180 Amplitude Vorticity	111
5.18	PIV 35° out 180 Amplitude Vorticity	112
5.19	PIV 45° out 180 Amplitude Vorticity	113

5.20	PIV 180 Amplitude Quiver Plot	114
5.21	PIV 30° in 150 Amplitude Vorticity	115
5.22	PIV 15° in 150 Amplitude Vorticity	116
5.23	PIV 0° in 150 Amplitude Vorticity	117
5.24	PIV 0° out 150 Amplitude Vorticity	118
5.25	PIV 15° out 150 Amplitude Vorticity	119
5.26	PIV 30° out 150 Amplitude Vorticity	120
5.27	PIV 150 Amplitude Quiver Plot	121
5.28	PIV 30° in 120 Amplitude Vorticity	122
5.29	PIV 15° in 120 Amplitude Vorticity	123
5.30	PIV 0° in 120 Amplitude Vorticity	124
5.31	PIV 0° out 120 Amplitude Vorticity	125
5.32	PIV 15° out 120 Amplitude Vorticity	126
5.33	PIV 30° out 120 Amplitude Vorticity	127
5.34	PIV 120 Amplitude Quiver Plot	128
5.35	PIV 180 Amplitude Y Velocity	130
5.36	PIV 150 Amplitude Y Velocity	131
5.37	PIV 120 Amplitude Y Velocity	132
5.38	Wing Positions at Mid-Stroke	134
5.39	PIV Mid-Stroke 180 Amplitude Vorticity	135
5.40	PIV Mid-Stroke 150 Amplitude Vorticity	136
5.41	PIV Mid-Stroke 120 Amplitude Vorticity	137
5.42	PIV Mid-Stroke 180 Amplitude Y Velocity	138
5.43	PIV Mid-Stroke 150 Amplitude Y Velocity	139
5.44	PIV Mid-Stroke 120 Amplitude Y Velocity	140
A.1	Wing 4E AOA Mapping	155
A.2	Wing 4F AOA Mapping	156
A.3	Wing 2G AOA Mapping	157
A.4	Wing 4G AOA Mapping	158
A.5	Wing 4H AOA Mapping	159
A.6	PIV 180 Amplitude X Velocity	161
A.7	PIV 150 Amplitude X Velocity	162
A.8	PIV 120 Amplitude X Velocity	163
A.9	PIV Mid-Stroke 180 Amplitude X Velocity	164
A.10	PIV Mid-Stroke 150 Amplitude X Velocity	165
A.11	PIV Mid-Stroke 120 Amplitude X Velocity	166

List of Tables

2.1	Motor Data [69]	22
5.1	2 Volt Symmetric Control	86
5.2	3 Volt Symmetric Control	86
5.3	2V Load Cell Results: Individually Controlled Wing	88
5.4	3V Load Cell Results	88

Acknowledgment

I would like to take this opportunity to extend my thanks to my wife and kids for all their support and love. To my parents and sister who have always supported me through this educational journey. To the Center for Micro Air Vehicle Studies laboratory and the students and staff who I have worked with for many years. I would also like to extend my thanks to the Air Force Research Laboratory for their support on this project and me through all my years working on Micro Air Vehicles. Last but not least I would like to extend my deepest thanks to Dr. George Huang for his hard work and support as well as my committee for the support and constructive criticism that has truly made this dissertation a work that is a contribution to the field of Flapping Wing Micro Air Vehicles.

Dedicated to
My wife Elizabeth
whose love and support has made the completion of
this work possible and to our two wonderful children
Alexia and Colton

INTRODUCTION

1.1 Introduction

Unmanned aerial vehicles (UAVs) have gained significant attention over the past few decades. The ability to remove the pilot from the vehicle and maintain a presence in the sky for military applications is literally a life saving effort, not to mention the added efficiency of not needing the space for a cockpit nor the payload of a human and the required life support. Furthermore, the absence of a pilot allows for high force maneuvers that a human cannot withstand. Over the past decade the push has been to move from the larger UAVs which fly over cities, down into cities and even into buildings. These vehicles have been termed Micro Aerial Vehicles (MAVs) [1]. Removing the restriction of a human passenger allows the aircraft to dramatically shrink to this new size of flight vehicle. While military applications for such a vehicle may appear dominant, as seen in some new video games and movies, one cannot fail to recognize the usefulness to the local law enforcement and civilian opportunities. The ability to see around the corner in a hostage situation or into a fallen building or collapsed cave for survivors can be life saving for all parties involved. The speed and size requirements of such vehicles pushes the technology and aerodynamics to another level of complexity. The low Reynolds numbers associated with the relatively slow flying vehicles had only been investigated by the biologists who study birds and insects [2]. MAVs researchers have been working to understand the aerodynamics of these natural fliers and to learn and replicate such advanced flying as that seen in hummingbirds, dragonflies and fruit flies to name a few.

1.2 Purpose

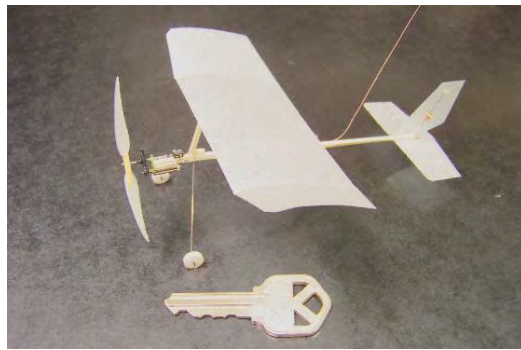
Significant knowledge and experience has been gained by developing, designing and manufacturing MAVs with a vast amount of tools and materials. The following contents aid in the determination of size and capability of desired near future MAVs and the tools available to develop, design, manufacture and test such mechanisms. Additionally, the aerodynamics associated with such mechanisms of similar size and weight are investigated to help understand the unsteady and dynamic nature of the vehicle's flight mechanisms. The testing of the flight weight vehicle can provide insights to aerodynamic and inertial coupling that cannot be seen in water tunnel testing. Furthermore, using the flight mechanism shows the effects of aerodynamic/inertial coupling on mechanism and motor constraints that cannot be seen with large flapping actuators typically used for bench testing. Testing was performed in a manner to provide results for as accurate forces and flows as possible for the MAV flight regime.

1.3 Literature Review

The study of MAVs ranges vastly from biological to computational to experimental studies of design, control, stability, flow, efficiency, etc. The focus of papers ranges from the construction of a flapping vehicle capable of carrying sensors to the understanding of the most basic flight mechanisms found in nature by birds and insects. Fixed wing and helicopter styled vehicles are also found in the area of MAVs. The dynamics for these platforms are fundamentally different from that of flapping wing vehicles. It is theorized that at low Reynolds numbers the flapping wing vehicle can be more efficient than rotor-craft [3]; Furthermore, a flapping wing vehicle is more likely to be hidden in plain sight than typical rotor-craft [1].

1.3.1 Fixed Wing Flight

Fixed wing flight, on a small scale, has been an area of interest for hobbyists for years. To date, some of the smallest fixed wing aircraft can be found at the Micro Flier Radio website [4]. The smallest is a 0.5 g rubber band powered fix wing vehicle made primarily of carbon fiber and mylar. The smallest controllable is a 0.7 g 3 channel, 4 in span fixed wing plane. The plane utilizes a 3.2 mm diameter pager motor and is powered by the Full River 10 mAh battery. ParkZone also sells a fixed wing aircraft named the Vapor, which is



(a) Micro Plane [4]



(b) ParkZone Vapor [5]

Figure 1.1: Fixed Wing Micro Air Vehicles

typically used by beginners. The plane is 16.4 g and has a wingspan of 15 in. These planes are stable and easy to fly due to good balancing and a large dihedral built into the wings. The vehicles are three control channel planes giving rudder, elevator and throttle control. The plane can carry a payload of 7-10 g which is sufficient for micro cameras and their transmitters. Zufferey modified a 5.2 g Didel SA “micro Celine” fixed wing aircraft for autonomous flight [6]. The plane was instrumented with two cameras, two rate gyros, an anemometer and Bluetooth micro control board. The overall mass was increased to 10.3 g including all sensors, control boards and batteries. Speed and turning are controlled by the on-board controllers and altitude was controlled by a pilot. The plane was flown in a room with illuminated black and white texture that was projected onto the walls. The plane was

successful in using vision-based feedback to control the plane around the room.

The advantages of fixed wing flight are that they are typically more efficient than helicopter or flapping flight while flying forward. By using their forward velocity to generate lift, a more efficient cruise can be attained. Problems for fixed wing flight occur in small winding areas such as indoor hallways and rooms. Hovering is atypical for fixed wing fliers making indoor or close quarter flight undesirable.

1.3.2 Rotor Craft Flight

The hobby industry has been shrinking the helicopter and multi-copter platforms as well. Blade makes a 17 g helicopter can fly via means of a three channel remote. The Scout CX can be seen in Figure 1.2(a). Air Hogs makes a 10 g two channel helicopter with adjustable center of gravity to adjust for forward flight. The Pocket Copter can be seen in Figure 1.2(b). Similar helicopters can be found as toys from the Blade and Air Hogs brands.



(a) Micro Helicopter [7]



(b) Air Hogs Pocket Copter [8]

Figure 1.2: Micro Helicopters

Trirotors, Quadrotors, Hexacopters, and Octocopters have also been of interest. The most common is the quadrotor and consists of four motor and propeller assemblies. Videos of these vehicles performing acrobatic maneuvers can be found all over the internet. One

of the most notable is a demonstration by University of Pennsylvania in a motion sensing room [9]. Nine vehicles simultaneously play an excerpt of the James Bond Theme song using various instruments [10]. The group has also done formation and acrobatic flight demos. Raffaello D'Andrea is also involved with quadrotor flight, controls and capability. Raffaello is a Professor of Dynamic Systems and Control at the Swiss Federal Institute of Technology in Zurich [11]. He has done several talks on of which can be found on youtube, one such is a TED talk [12]. These vehicles are primarily used for hobbyists and control allocation researchers.



(a) AR Parrot Drone [13]



(b) Blade Nano QX Quadrotor [14]

Figure 1.3: Quadrotor Platforms

The AR Parrot drone, shown in Figure 1.3(a), can be purchased for home use and flown via means of an iPad, iPod touch, iPhone, or Android device [15]. Internal stabilization makes for an easily flown platform for beginners or can be modified for a more unstable, acrobatic flight for expert pilots by disabling the accelerometer stabilization. The drone has two high definition cameras onboard that are used for maintaining position and recording forward speed. Either can be used to record video or take pictures. The basic AR Parrot drone can be purchased for around \$220 and version 2.0 can be purchased for \$300 on Amazon.com.

There are numerous micro fixed and rotary MAVs available. Rotorcraft are typically loud and more easily seen. While they have proven to be capable of carrying sensors, and control algorithms are widespread, researchers believe that a more natural flier may be better suited for some missions [2].

1.3.3 Flapping Wing Flight

Bio-inspired is a commonly used term in the field of flapping wing micro air vehicles. Natural fliers can fly incredible maneuvers at many scales while mechanical flapping vehicles to date are marginal at best. The manufacture of a vehicle capable of flight has proven to be a delicate, difficult process. To date there are several flying flapping wing micro air vehicles, of which are mostly bird-like flying vehicles. Bird-like fliers do not take advantage of the most desirable characteristics found in insects and small birds such as snap acceleration and efficient hover capability [2]. Most of the flying models do however find flight characteristics somewhere between rotorcraft and fixed-wing fliers. Furthermore, the flapping wing fliers appear more natural than the aforementioned approaching the desired “hidden in plain sight.”

Bird-Like Fliers

Bird-Like vehicles use their wings to produce thrust and are controlled by a rudder and elevator. Some are capable of hover with slight drift. Center of gravity adjustments can be done to adjust the vehicle to be advantageous for forward or hovering flight. Hsu and Huang designed such a flapping wing micro air vehicle [16]. The vehicle weighs near 10 g, has a flight time of 10-20 min and a payload capacity of 3 g. The flapper is remote piloted and can be outfitted with a camera and transmitter. Delft University has three different flapping wing micro air vehicles. All fly on the same concept of thrust from the flapping wings and control by rudder and elevator. The smallest is the Delfly Micro which weighs 4 g, has a wing span of 10 cm and is outfitted with a camera [17]. Mueller performed lift and

thrust testing on a flapper designed by Banala of which has a weight of 13.2 g, a payload capability of 2.5 g and a maximum flapping frequency of 7.2Hz [18]. This flapper does not have a second set of wings changing the definition to an ornithopter. Further examples of forward flying, bird-like flapping micro air vehicles can be found by Tan, Ang, Fenelon, Pornsin and Mazaheri [19–24]. Galiski and Hu performed bench testing on non-flight worthy mechanisms of birdlike flapping [25–27]. Peng and Yang performed simulation experiments on birdlike flappers [28,29]. Yang used a flight weight flapper for wind tunnel testing in conjunction with the simulation.

While all of these vehicles are a change from the conventional flier, namely because they do not use a propeller for thrust, they do retain characteristics similar to the conventional fliers. A tendency to hover better than a fixed wing and fly forward better than a helicopter or multi-copter while attempting to find the hidden in plain sight aspect has certainly provided interest and good press for these types of vehicles.

Insect-Like Fliers

Although the aforementioned vehicles are a change from the conventional fliers such as an airplane or helicopter, a more radical type of flier was desired for the concept of the flapping wing micro air vehicle. A flier which imitated that of bees, wasps, flies, dragon flies and fruit flies to name a few. The closest realization to the reality of this type of flier is the Hummingbird I and Hummingbird II of the DARPA sponsored project done by AeroVironment Inc [30]. The model is composed of two wings which are used to lift and control the vehicle. The wings are driven by a main spar and controlled using an attachment point at the inner lower corner of each wing. The wings can be made stiffer by moving the control point into the body of the mechanism, and angle of attack can be changed by moving the connection point fore or aft of the vehicle. The control scheme is a clever use of a single control point per wing. The mechanism is a huge success in the field of MAVs. The demand of longer flight time and greater payload requires bio-inspiration

to further the field. It is likely that a more efficient flapping method exists. One feature lacking in the Hummingbird I and II is that the wing is not allowed to provide the dynamic feature of rotation circulation commonly found in nature [31]. This feature is a product of wing rotation at the end of the wing stroke due to the stiffness of the wing and the release of the aerodynamic load on the wing during supination and pronation. The wing rotation is thought to increase lift through inertial and aerodynamic forces and readies the wing for the next half stroke providing the correct wing orientation.

Wood of Harvard University is making a pico-scaled air vehicle [32–35]. The vehicle is created using MEMS technology and uses piezoelectric actuators to flap and control the vehicle. The vehicle has a mass between 53-125 milligrams (mg), depending on the model. The vehicle is now capable of controlled tethered flight. A difficulty with piezo-

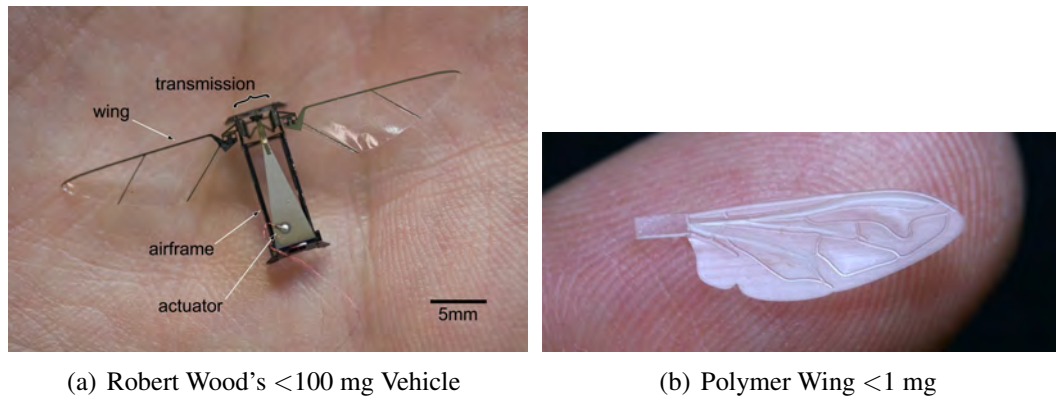


Figure 1.4: Harvard RoboBee and Wing, from Ref [34]

electric flight is carrying and transforming a power source capable of producing the high voltages needed for piezoelectric actuators. Many challenges lay ahead in the piezoelectric air vehicle field but great successes have been accomplished by Wood et al.

In addition to Wood, Arabagi has designed a piezoelectric air vehicle that has a mass of 0.65 g [36]. This vehicle has a lifting power of 0.1 g but the group hopes to find greater than one lift to weight ratio using a scaling analysis and appropriately designing a new bird for the task.

Yoon uses a voice coil to actuate a set of wings [37]. The model is 3 g. By using two

coils to actuate the wing Yoon is able to control the angle of attack (AOA) of the wing by adjusting the phase between the two coil signals. The model has a wingspan of 75 mm with a wing to body mass ratio of 2.5%. While lift forces generated were less than 0.2 g, the group was able to study the effect of AOA on lift for their model. The lift was proportional to the AOA from 0 deg to 60 deg. The group reported that the coil required 0.26 A at 6 V. Furthermore the power source would weigh in at 1.2 g and could supply an estimated seven minutes of flight time assuming the mechanism capable of flight.

One should not take these accomplishments lightly as they truly take a momentous amount of skill, intellect and effort to create flight in this flight regime of MAVs. However, a step outside will quickly demonstrate the long path ahead that lay for MAVs as an eagle or a fruit fly swim through the air so elegantly. Surely nature has much more to teach us.

1.3.4 Flight in Nature

While all natural fliers use wings to fly, not all accomplish flight in the same way [38, 39]. For example, an eagle does not flap the same as a hummingbird, nor does a butterfly flap the same as a dragonfly. To decide what type of flapping to emulate, several were investigated. Horizontal, vertical, two wing phase interaction and figure-8 are the major styles of flapping investigated. It should be noted that a single flapping style is not necessarily used exclusively for one flier's flight. For example, it is typical for horizontal fliers to exhibit clap and fling and passive figure-8 in their flapping cycles [40]. Furthermore, large birds have variations of vertical flapping styles for takeoff, cruise and landing. Understanding flapping styles is advantageous for designing and developing sufficiently sophisticated mechanisms to be flight worthy while minimizing complication.

Vertical Flapping

For vertical or avian flapping, the wings are moved up and down in an airplane orientation with head forward. This type of flapping is more typical for forward flight found in birds.

Butterflies also flap their wings in a vertical orientation but take advantage of clap and fling flight and do not rely on forward velocity to maintain lift. The wings of the butterfly are large in comparison to its body. By inspection of high speed video, the butterfly moves vertically significantly during the latter end of the downstroke [41]. While dragon flies do flap their wings vertically, their major lift mechanism comes from the interactions between the fore and aft wings and will be briefly discussed later [42]. Birds adjust their wings for upstroke and downstroke to reduce the negative effects of the upstroke [43]. The wings are extended to achieve the largest area for the downstroke and pulled closer to the body for the upstroke. Emulating flappers of this kind are made by Festo among many other of their nature emulated robots [44].

Horizontal Flapping

Horizontal flapping is commonly found on small birds and insects. Horizontal flapping refers to the wings being thrust fore and aft of the body in a head up orientation. Hummingbirds, lady bugs and bumblebees can be seen moving their wings as such. Possibly the most apparent and dynamically simple lift portion of this flapping method is the swinging of the wing from back to front and front to back. The rotation of the wing creates a leading edge vortex (LEV), which for laminar flow remains attached to the wing [31, 38, 45–47]. Usherwood investigates the aerodynamics of revolving wings [48, 49]. The wings are rotated in a single direction and measured for forces during the first half revolution from rest and steady flow conditions. No wing to wing interactions occurred during this testing, nor does wing reversal. A motor is used to rotate the wings and a balance strain gauge setup is used to measure force. Several aspect ratios, angles of attack and Reynolds numbers are investigated showing very slight differences in coefficients of lift and drag. Wings were fabricated to model the shape of a female hawkmoth wing which was then scaled up by a factor of 10 reaching a final span of 500 mm.

DeLuca uses a piezoelectric actuator to flap engineered hawk-moth wings [50]. The

wings are dynamically similar to the hawk-moth in size, shape, bending stiffness and torsion stiffness. A force balance is used to measure the lift and drag on the wing. High speed cameras are used to measure the deflection of the wing throughout the flapping cycle. In addition to wing tracking and force measurements, flow measurements were performed using stereo phase-lock PIV for eight locations in the stroke. These measurements are made from the side of the vehicle at four locations along the span of the wing. The wing utilizes an AOA wing stop and does not rely solely on wing flexibility to achieve large AOAs. The stops are set to 30 degrees, 45 degrees and 60 degrees. While flexibility may provide different results at wing reversal due to aerodynamic, inertial and stiffness combining to provide different flow patterns, the LEV should remain apparent and similar during the wing stroke. DeLuca's results do show the LEV remains attached through the stroke but do not investigate wing reversal flow patterns.

In addition to the sweep of the wing, other effects have an influence on the lifting capability namely clap and fling, rotation circulation and wake capture [31,39,45,47]. These four phenomena provide more lift than is accounted for by conventional aerodynamics. A study done on a two winged flapper compared a blade element model with load cell results to see an increase in lift of as much as 67% from clap and fling, rotation circulation and wake capture [51]. Clap and fling is a phenomenon that occurs with wing interactions. The wings force air out the bottom during the clap portion and create a low pressure above the wings during the fling portion creating lift through supination and pronation [45]. While quantifying the added benefit is difficult to separate from other effects, researchers have computationally and experimentally investigated the clap and fling with both rigid and flexible wings [52,53]. Lehmann scales a fruit fly wing in a mineral bath. The wing is rigid and shows an increase in mean lift up to 17% when a mirrored wing is added. Particle image velocimetry (PIV) was used to measure fluid flow for these experiments. Miller computationally calculates an increase in mean lift of 35% for a 2D simulation with rigid wings and Reynolds numbers less than 128. In addition to added effects of pushing flow

out the bottom and creating low pressure on top it was noted that the translation motion showed greater lift as well with the added wing [53].

Rotation circulation is theorized to provide an added lift at the end of the stroke due to the rotation of the wing [31, 39, 47]. Dickinson describes the effect as being similar to that of the Magnus effect which is used in baseball to generate a curve due to the spinning of the ball. The effects are dependent upon the timing of the rotation relative to the stroke reversal. If the rotation occurs before the stroke reversal, an increase in lift should occur, replicating a backspin. If the rotation occurs after the stroke reversal the effect would be a negative lift, replicating a topspin [31]. Walker investigates this effect by means of three simulation methods: unsteady blade element model, quasi-steady model and computational fluid dynamics (CFD) modeled forces with a dynamically scaled *Drosophila* wing. Data suggests that the effects are aerodynamically caused by the same fluid-dynamic mechanism that occurs during wing translation and not a novel effect due to wing rotation alone [54].

A more intuitive effect is wake capture. This phenomena occurs upon and shortly after wing reversal. As the wing slows and reverses itself, the flow created in the previous flapping stroke is still moving. The wing “catches” this flow giving an effective wing velocity, increasing lift. A person can experience this when treading water, when your hands reverse you push back on the fluid momentum giving a greater effective force. From a blade element perspective, the velocity of the wing relative to the working fluid would be greater than the wing velocity relative to the body of the flier, increasing lift. Dickinson investigates the role of wake capture using advanced, symmetrical and delayed rotation to translation. Results showed that an advanced wing rotation gave greater lift at stroke reversal than symmetrical. Furthermore, a delayed stroke reversal causes a negative lift due to the impinging flow on the backside of the wing angled wing [31].

While not directly apparent, these experiments show the importance of a flexible wing versus a stiff, passively rotating wing. A flexible wing will reorient itself for the next stroke when the strain energy overcomes the aerodynamic forces at the end of the stroke. Depend-

ing upon the wing stiffness, this can allow for an advanced rotation to translation, taking full advantage of the wake capture and possibly rotation circulation. A passively rotating wing relies on inertia and/or the previous wake to reorient itself for the upcoming stroke causing a symmetrical or delayed rotation to translation relationship, wasting precious lifting capability.

Figure-8 Flapping

Figure-8 flapping is believed to be a passive result of wing motion versus a driven motion [51]. When the figure-8 was driven and not passive, half of the stroke cycle was spent transitioning the wing without creating any aerodynamic forces [40]. While few papers were found describing cicada flight or figure-8 flapping in general, one such paper was found that performs free flight reconstruction of the wings via three high speed cameras [55]. Their investigations show the wingtip trajectory and associated pitch. Figure 1.3.4 shows that the figure-8 is not exaggerated, however the insect creates lift on the downstroke and thrust on the upstroke. While a seemingly efficient means of producing the desired results of flapping wings using pure drag force to stay aloft, the mechanics are significantly more complicated from a design and control standpoint.

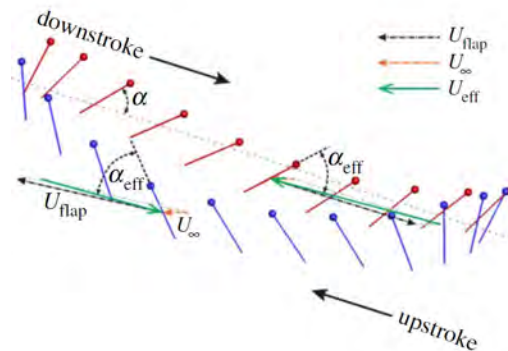


Figure 1.5: Cicada Wing Tip Path, from Wan [55]

Two Wing Phase Interaction

Two wing phase interaction utilizes the wake from the first wing to create added lift for the second wing. Typically the fore wing is flapped first and the hind wing second. Dong uses a 3 camera system high speed system to record dragonflies in free flight. The resulting video was reconstructed and input into a CFD program to investigate flow and lift characteristics of the insect [42]. Dong's calculations show a positive lift throughout the entire flapping cycle. Broering uses a 2-D CFD model to investigate the effect of phase angle and wing spacing on tandem wings [56]. As one would expect, the phase angle and spacing had significant effects on maximum lift and maximum efficiency. Three phase changes were used in the simulation and 4 wing spacing values were chosen. To truly understand the potential benefits of tandem wing interactions more data points must be taken. Dileo uses a bench model and load cell to investigate wing interactions using two independent motors and flexible wings made out of carbon fiber reinforced polyester film [57].

1.3.5 Insect Wing Investigations

The importance of wings cannot be overlooked for flapping wing vehicles. Mass, size, aspect ratio and stiffness all play important roles in the wings of flapping vehicles and insects [30, 52, 58–66]. Many researchers have looked at the wings of insects and studied them for all of the traits aforementioned.

Combes and Daniel compare the span-wise and chord-wise stiffness of insect wings across 16 species of insects [60]. The results show that span-wise stiffness is 1 to 2 orders of magnitude larger than chord-wise stiffness. Furthermore the study shows that wing size accounts for over 95% of the variability in stiffness's measured, indicating a stiffness "sweet spot" for a given size wing. The span-wise and chord-wise stiffness increases linearly with the span and chord lengths respectively among the wings measured [59]. In part two of the paper the spatial distribution of the stiffness of the wings is investigated. It is approximated that the stiffness can be modeled using an exponential decline across the

leading edge in the span-wise direction and from the leading edge to the trailing edge in the chord-wise direction.

Agrawal scales a man-made synthetic wing to match that of a *Manduca Sexta* or Hawkmoth for shape [67]. Only a single wing is flapped. The wing is flapped at .9 Hz compared to 26 Hz, thus requiring the wing to be scaled much larger than the Hawkmoth. The resulting forces are near 1 g of lift. Two wings are constructed, neither of which are identical in any way to the Hawkmoth other than shape. One of the wings is rigid and the other is flexible. The wings are given a prescribed AOA and the lift and thrust are measured. The rigid wing produces the largest lift of 1.42 g at an AOA of 40 deg. The maximum lift produced by the flexible wing is 1.13 g at AOA of both 40 and 50 deg. The flexible wings performed better than the rigid wing in every thrust force generated. Relevance of flexible vs. rigid wing is difficult to note for this experiment because little is described about stiffness in comparison with the insect and there is no study done to investigate varying the stiffness for a more optimal wing. Furthermore, prescribing a wing AOA can be questioned for bio-mimicking and dynamic wing lift mechanisms.

O'Hara also studied Hawkmoth wings and attempts to replicate the wing characteristics in a manmade wing using a laser cut Pre-Preg, consisting of three layers [64]. The three layers give flexibility in different orientations adjusting the torsional stiffness of the manufactured wing to match stiffness properties of the *Manduca Sexta* wing with the mass properties already defined by the venation layout. The engineered wing was then covered with Mylar and hot pressed to attach the film. The first bending mode for the insect wing is 65 Hz while the manufactured wing is 62.1 Hz and first torsion mode for the bio wing is at 110 Hz for the insect wing and 120 Hz for the manufactured wing as shown by FEA. O'Hara achieves a lift of approximately 1 gf for the wing at 22 Hz. The manufactured wing measurement was within 7% of the insect wing. The wings were tested using a bench model piezoelectric actuator. O'Hara shows promising results for matching an insect wings size, weight, planform and performance using reasonable techniques and a precision laser

cutter. The resulting mechanism and wings are used in DeLuca's work on force and flow measurement [50].

Hu and Deng also investigate the lift capability of Hawkmoth wings [65]. These are compared with man-made wings which are made from carbon tow, epoxy and Mylar film. The wings are tested using a four-bar mechanism over a frequency range from 15-50 Hz. Lift coefficients were calculated from knowledge of the wing, flapping frequency and lift. The largest lift coefficient occurred near 40 Hz with a value of approximately 2.1 gf. The lift for the cicada wing is approximately 45 mN or 4.6 gf. The man made wing saturates near 40 Hz with a lift near 3.9 gf. The wings are comprised of 3 veins of carbon fiber. At this size it is difficult to create multiple veined structures without dramatically increasing the mass of the wing. Hu concludes that for the given Hawkmoth to take flight a coefficient of lift of 2.6 would be necessary. This indicates that an increase in lift while on the insect occurs and could possibly be due to wing interactions, velocity profiles or hind wing performance.

Mountcastle and Daniel confirm that fresher more compliant Hawkmoth wings provide better performance [68]. They use a motor to actuate the wings and measure the flow using PIV at a frame rate of 2100 fps. The fresh wings generated 2.5-4 times the amount of average inflow as compared with the same wings tested after drying and stiffening.

In addition to the wings themselves, the investigation of whether the inertial or aerodynamic forces dominate wing bending is of concern. A flight controller will rely on the difference between inertial and aerodynamic force dominance for tailless control. Combes and Daniel compare the wings of a hawkmoth while flapped in air and helium [58]. The significance being that the helium is only 15% as dense as air. Deflections are not significantly different between the air and helium thus implying the aerodynamic forces are minor compared to the inertial forces on the wings of a hawkmoth. The study was done for hovering flight. It is possible that forward flight could change the effects of aerodynamic and inertial forces on the wings. The study also alludes to the use of inertial models to gain

insight on wing deformations vs. aerodynamic or coupled aerodynamic-inertial models drastically reducing computation time. It should also be noted that the Hawkmoth typically has wing mass to body mass ratio of between 2% and 4%; For many insects this ratio is near or below 1%. It is certainly possible that this ratio can control the dominance effect of aerodynamic vs. inertial load dominance on a wing. The ratio of mass moment of inertia to area moment of inertia is certainly instrumental in determining this relationship.

1.4 Conclusions

Nature, to date, has set the standard for flight efficiency and maneuverability at the “micro” level. Application of the flight principles found in nature to MAVs is necessary for the betterment of the field. While flight accomplishments to date are impressive, there is still much to be learned and added to the technology by learning from nature. Forward flying bird like vehicles require too much air speed to be truly maneuverable and are most efficient with that airspeed that is lacked in small volumes such as hallways and collapsed buildings. Fixed wing fliers fail in the same way but worse, relying on air speed even more than the flapping wing fliers. Rotorcraft are typically loud and cannot fulfill the desirable hidden in plain sight sought by many MAV applications. The piezoelectric flier developed by Wood and his team fails to leave the bench top until sufficient power sources and or electronics are capable of providing on board functions while maintaining control and lift great than vehicle weight. While AeroVironment has created a flying two winged tailless vehicle, it does not exhibit the flapping characteristics provided by a flexible wing so clearly seen in every biological study done. Surely a more natural wing and control scheme can provide a more efficient, responsive vehicle.

Major knowledge gaps exist at the stroke reversal where the most complex flow patterns occur. Specifically the aerodynamic, inertial and stiffness characteristics are all influenced by one another, presumably for beneficial lift. Additionally, wing to wing in-

teractions are thought to increase lift at wing reversals. While many researchers theorize what is happening, namely, rotation circulation, wake capture and clap and fling, little has been done to understand the benefits and fundamental flow patterns associated with them. Understanding the lift mechanisms and their contributions to overall lift of the vehicle is important in determining how much effort must be placed on "tuning" the wings, mechanism and their interactions. The ultimate goal of the research effort is to design a flight weight mechanism that is bio-inspired and attempts to generate the effects found in nature and investigate the flow patterns at the wing reversal.

1.5 Original Contributions and Organization of Dissertation

In order to investigate the flapping characteristics found in nature, a vehicle was designed that can emulate natural movements. Chapter 2 describes some commercial-off-the-shelf (COTS) items that are typically used to provide a baseline of what is available for a researcher/designer. A novel bio-inspired design is fully explored from drive mechanism to mechanical control schemes to achieve motions similar to nature in Chapter 3. The drive mechanism design is explained for a full understanding of achieving a four bar mechanism capable of generating large flapping amplitudes. The mechanism is designed to use the flapping styles and control methods found in nature, specifically being large flapping angles of up to 180 degrees, servo driven wing angle of attack control and servo driven roll control. Furthermore, methods of wing design and manufacture are investigated in Chapter 4. Design of the wings are derived from biological venation patterns across several types of insects. Wings are experimentally optimized to achieve smooth flapping and large angles of attack similar to what is found in nature. Mechanisms and wings are tested via load cells, high speed cameras and particle image velocimetry (PIV) in Chapter 5 to see the effectiveness of the vehicle and its subsystems, most notably the wings performance and interaction. Comparisons of several wing venation patterns are made using load cells

and high speed imagery to attain physical orientations of the wings throughout the flapping cycle. Additionally, experimental optimization is done on the wings to achieve flapping wings that appear similar to insect deformations and velocity profiles as inspected by high speed video. PIV is used to determine flow patterns of one such wing venation at multiple flapping amplitudes. The data presents a phenomena of trailing edge vortex capture upon wing reversal. This flow interaction may explain another part of the lift enhancing mechanisms used in flapping wing fliers as a supplemental effect of wake capture.

DESIGN PRINCIPLES

2.1 Introduction

The building blocks of design are used to combine basic concepts into desired mechanisms. Mechanisms as a whole can be very complex to understand, much less design. When taken on an component or subset basis these complications dwindle to a simple, easily understood design. Generally these designs more easily modeled for kinematics and inertial effects. In addition to the ability to simplify the mechanism for design and modeling purposes, the available tools for actuation and power storage must be known to determine available power, weight and size regime of the vehicle and possible control methods. The radio controlled hobby industry is the current push for smaller, lighter more efficient batteries, actuators and motors. Many cell phone technologies have also pushed the advancement of batteries, motors, controller boards and cameras. However, cell phone components are not as easily accessible as the RC-hobby electronics. The high speeds that are typical of small DC brushed or brushless motors require a transmission reduction to reduce speed and increase torque to the actuator. All of these methods and a suite of their options will be discussed in the proceeding sections.

2.2 Electro-Mechanical Actuation

There are three distinct types of mechanical actuation. The first type generally provides the thrust or lift for the vehicle in the form of a brushed or brushless DC motor. These

motors are typically low torque, high speed motors. Commercially, cost effective brushed coreless motors can be found as small as 4 mm diameter and weigh in as low as 0.66 g. These motors are typically less than ten dollars apiece. Brushed motors require no more than a DC voltage to be applied and varied to adjust speed. This is convenient for testing using a basic DC power supply with a sufficient current rating. Micromo and Faulhauber sell similar sized motors. These motors typically come with motor specifications such as efficiency and torque constants, however, cost will significantly increase. One such motor was purchased including an encoder on one end and planetary gear set on the other side. While significantly more complex than the bare coreless motor, these motors cost approximately \$400 apiece. Brushless motors are slightly larger but can be found as light as 1.6 g. “The Mighty Motor” as it is called is used by TU Delft’s Delfly II and provides sufficient power to fly the 16 g four wing flapper. Sizes of brushless motors increase stepwise to larger more powerful sizes. The current motor of choice on the two winged flapper is a 3.5 g motor capable of 33,000 rpm no-load speed. The motor can be run on either 1 or 2 cells and has a rated maximum burst current draw of 3 amperes (A) and rated continuous current draw of 2 A. The brushless motors require motor controllers to commutate the coils in the motor. This adds another need of control to the system, however COTS solutions are readily available to be used with many transmitter/receiver setups. The smallest found to date are from Micro Flier Radio at 0.080 g for a 1 cell, 1 A maximum speed controller. As current rating increases so does the weight of the speed controller but even at a 2 cell 7 amp maximum current rating the controller weighs only 1.45 g as a bare board (not including the wires).

Table 2.1 has been compiled by homefly.com. The table has 17 different brushless motors that are tested ranging in mass from 1.5 g to 12 g. The lightest capable of up to 22 g of thrust with a 2 cell battery and the largest capable of 205 g of thrust on a 3 cell battery. All thrusts are generated using propellers and several sizes and pitches are used to maximize thrust and motor safety. The best 3.5 g motor and propeller setup provided a

Table 2.1: Motor Data [69]

motor	weight(g)	prop (in)	thrust(g)	V (V)	I (A)	prop (cm)
10-1-36T	1.5	2.5x1	11	3.7	0.55	6.3x2.5
10-1-50T	1.5	3.1x2	12	3.7	0.58	8x5
		3.1x2	22	7.2	1	8x5
10-3-20T	3	1.2"dia DF	40	7	3.2	30mm DF
10-3-32T	3.5	3.1x2	30	7	0.72	8x5
		3x2	31	7	0.74	7.6x5.1
		4x2.5	40	7	0.95	10.2x6.3
10-3-26S	3.5	5x3	27	3.5	0.9	12.7x7.6
		4x2.5	22	3.5	0.7	10.2x6.3
10-3-26D	3.5	3x2	32	3.5	1.4	7.6x5.1
		4x2.5	37	3.5	1.9	10.2x6.3
13-2-16	4	3x2	72	6.8	2	7.6x5.1
13-3-14	5.2	3x2	56	7	1.43	7.6x5.1
		4x2.5	88	7	2.22	10.2x6.3
		5x3	43	3.5	1.3	12.7x7.6
		6x3	50	3.5	1.67	15.2x7.6
13-3-12	5.2	5x3	52	3.5	1.77	12.7x7.6
		6x3	61	3.5	2.29	15.2x7.6
13-3-20	5.2	5x3	67	7	1.3	12.7x7.6
		6x3	78	7	1.5	15.2x7.6
10/6/2020	5.5	5x3	60	7	1.3	12.7x7.6
10/6/2016	5.7	5x3	80	7	1.8	12.7x7.6
13-4-15	6.2	4x2.5	53	7	1.1	10.2x6.3
		5x3	86	7	1.64	12.7x7.6
		6x3	105	7	2.16	15.2x7.6
		3x2	61	10	1.17	7.6x5.1
		4x2.5	96	10	1.8	10.2x6.3
		5x3	139	10	2.48	12.7x7.6
13-6-9	8	5x3	107	7	2.3	12.7x7.6
		6x3	144	7	3	15.2x7.6
		7x3.5	156	7	3.6	17.8x8.9
13-6-9CS	8	5x3	152	7	3.16	12.7x7.6
		6x3	190	7	4.32	15.2x7.6
13-6-11	8	5x3	85	7	1.5	12.7x7.6
		6x3	124	7	2.24	15.2x7.6
		7x3.5	142	7	2.74	17.8x8.9
		5x3	156	10	2.8	12.7x7.6
		6x3	210	10	3.5	15.2x7.6
195.03	12	6x3	205	10.5	4	15.2x7.6

maximum thrust of 40 g on a 2 cell battery. This is the same size motor used in the vehicle found in Chapter 3. The particular motor used is purchased from radicalrc.com with SKU Number: HEMICRO74V. The 6 mm and 8 mm coreless motors seen throughout Chapter 3 are Blade motors from their helicopters model numbers EFLH2210 and EFLH3003 respectively. These motors have been found to be superior to others that were on the market in 2011. These two motors can be seen in Figure 2.1(a) and 2.1(b) for the 6 mm and 8 mm respectively.

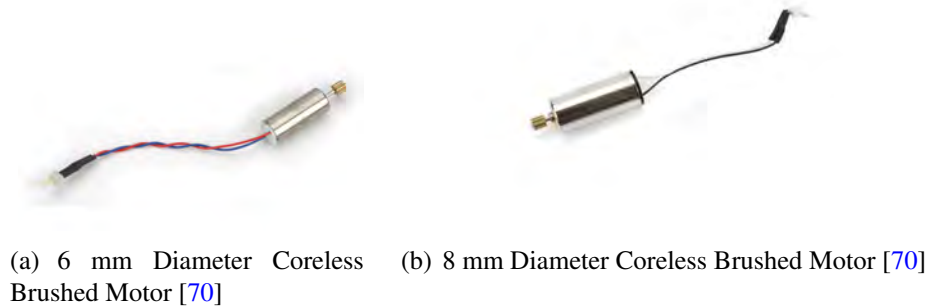
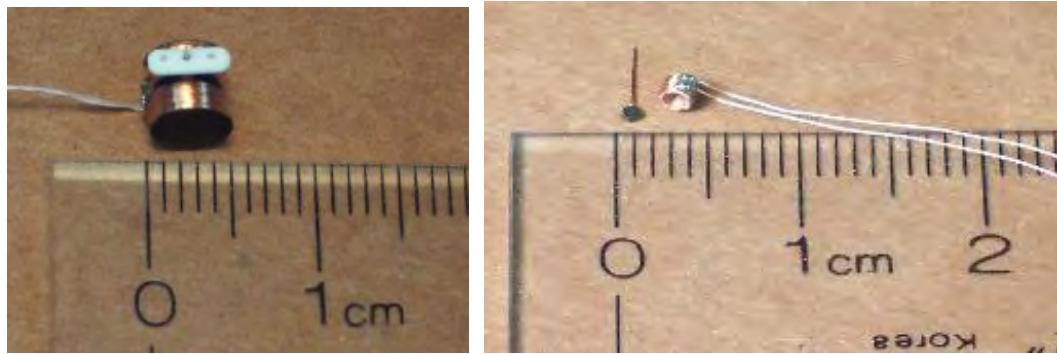


Figure 2.1: Electromagnetic Actuators

In addition to motors, actuation of control surfaces are typical for forward and flapping fliers. Electro-mechanical actuators commonly referred to as simply “actuators” and servos are used to drive the control surfaces. Actuators consist of a wire coil and magnet. Most are factory hinged, however, some come in separate pieces and require other hinge methods. These unhinged actuators are usually the smallest actuators available where there is little to no means of providing a hinge. The build uses other surfaces to create the hinge such as a vertical tail and rudder and can attach the coil to the vertical stabilizer and the magnet to the rudder. The hinge of the rudder is used to control the placement of the magnet in the coil. Upon energizing the coil, a moment will be applied to the rudder causing it to move about its hinge. Hinged actuators can support the control surface directly or use a connecting rod to move the surface on its own hinge. Micro Flier Radio has very small actuators, the smallest mass that is sold is a 25 mg and can be seen in Figure 2.2(b). An example of a hinged actuator can be seen in Figure 2.2(a) which weighs 400 mg.

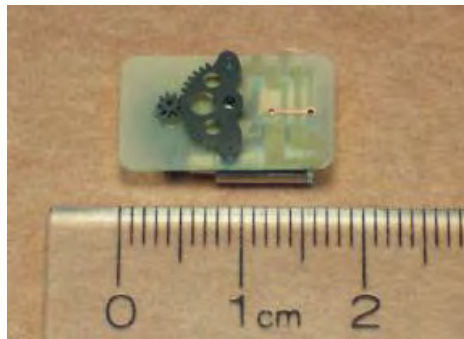


(a) 400 mg Mini Actuator [4]

(b) 25 mg Sub Micro Actuator [4]

Figure 2.2: Blade Coreless Motors

Servo actuators use motors to drive gear sets. Gear sets vary from gear trains connected to lever arms to worm gear sets. The gear ratios allow more torque to be produced by of the electro-mechanical device, in the case of the servo, the motor, however the cost is a heavier actuator. In addition to the motor, mounting devices, gears and feedback devices are necessary to control the actuation versus applying a voltage to the coil and magnet actuator. It is because of this that the actuators tend to be used for small vehicles, typically less than 10 g and servos are used above this weight covering most of the desired MAV realm to date. In addition to more torque, a servo needs very little power to maintain a position whereas a coil actuator can require relatively large power consumption for even a simple trim position. Longer duration, low maneuver flights would lend distinctly to servo control. Micro Flier Radio is again a supplier of the smallest servo actuator that I have found at a mass of 475 mg and can be seen in Figure 2.3(a). Spektrum makes a 1.5 g servo that is compatible with the AR6400 series receiver boards from Spektrum. The latter are the servos used to control wing control in Chapter 3 and can be found in Figure 2.3(b).



(a) 475 mg Sub Micro Servo From Micro Flier Radio [4]



(b) 1.5 g Spektrum Linear Servo [71]

Figure 2.3: Servo Actuators

2.3 Power Sources

Power sources are typically provided by the Lithium Polymer also known as Li-Po batteries. These batteries are capable of producing high power to weight ratios with high discharge rates typically rated from 25C-40C. The C rating for these batteries refers to the maximum and rated current draw acceptable for the battery. The C number refers to how fast the battery can safely be fully discharged. A C number of 15 means that the battery can be discharged in 1/15 of an hour or 4 minutes. A corresponding 100mAh battery with a 15C rating would then be able to provide 1500mA or 1.5A of max current for 4 minutes. The batteries have a rated output voltage of 3.7 volts per cell. These voltages can vary from 4.2V when fully charged to 3.0V when fully discharged [72]. The smallest single cell battery made by Full River is a 10 mAh battery which weighs 0.34 g and can be seen in Figure 2.4. Battery sizes go up from there to about any size desired. Typical prepackaged two

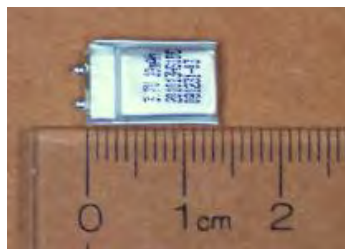


Figure 2.4: 10 mAh Full River Battery [4]

cell batteries begin at 120 mAh with a weight of 8.5 g. It is possible to run the smaller batteries in series to increase voltage. Using the smallest available battery, a designer should expect to have a flight weight of no less than 0.7 g. Typically the flapping and fixed wing vehicles use a battery weight near 30 percent of the vehicles total weight [16–20, 73, 74]. Super capacitors are one other type of power storage that can be used by lightweight fliers. Pornsin uses two 1 farad capacitors weighed in at 1.9 g but only provided approximately 1 minute of flight time [22].

2.4 Transmitters and Receivers

Many factors can go into choosing a transmitter and receiver. A designer must decide on the weight sensitivity of the vehicle and the options desired for the transmitter and receiver. If a total vehicle weight is desired to be less than ten grams then a transmitter receiver combination should be considered from either Micro Flier Radio or Plantraco. Both of these suppliers have receiver boards that are less than 1 g. Micro Flier Radio supplies a 4 channel receiver that weighs in at 115 mg. For larger models at or above the 10 gram flight regime, Spektrum 2.4 GHz receivers and transmitters provide robust, reliable communication. The receiver board used in Chapter 3 is an AR6400 series receiver that includes 2 of the 1.5 g Spektrum servos on the board and has a total weight of 4 g. The board has female plugs on it for expansion of more servos if needed or desired. Spektrum has several transmitters available that are “bind and fly” compatible with this particular board. Two such transmitters used are the DX7 and DX8 transmitters. While these transmitters supported much more functionality than can be used with the 4 g board such as telemetry not to mention the 7 and 8 channel control that these transmitters are capable of, they have quality joysticks that make flying more enjoyable for experienced RC pilots. The smallest receiver available from Spektrum is the AR610 6-Channel DSMX Aircraft Receiver (SPMAR610) which is a full range 2 g receiver. Depending on the desire, skill and knowledge level other receivers are available for customization from platforms such as Arduino and companies such as DigiKey. These receivers will not be ready to fly like the aforementioned products.

2.5 Gearing and Power Transmission

DC brushed or brushless motors run at speeds over 10,000 rpm with low torque, thus requiring the motor to be geared down substantially to accommodate the flapping frequency and torque necessary for flight. Typically the gear sets will require two gearing ratios to reach a large enough gear ratio for flight without requiring very large gears. Some gears can be purchased at various pitch diameter and teeth number. Gears can also be manufactured using high end 3D printers for plastic gears or CNC metal milling or EDM machines. Due to the need for robust custom gear design, all gears were custom made in house for the mechanisms discussed here. Depending upon the torque requirements, gears can be 3D printed out of plastic or machined out of metal. For years 3D printed gears provided great design flexibility and quick turnaround for model builds at the WSU laboratory. As motors became more powerful it was found that the plastic gears cannot hold up to the larger torques provided by more powerful motors without significantly increasing the tooth width. A wire EDM is capable of cutting gear profiles. While these gears were much more laborious to make and required much more time, the result was a more efficient, highly reliable gear train. Gears were made from 7075 aluminum and incorporated lightening holes to drop weight. A gear modulus of 0.3 was typical for ease of manufacture and size considerations. A smaller modulus was possible, however the wire used on the EDM must be smaller than 0.010 inches to cut the profiles. A 0.006 inch wire can be used to cut such gears but does have limitations. The gears on the left of the Figure 2.5 are cut with the 0.006 inch wire while the gears on the right are the 0.3 modulus gears cut using the 0.010 inch wire. The smallest gear successfully cut using the 0.006 inch wire is a .17 modulus gear.

2.6 Basic Building Materials

To this point much has been discussed about the COTS items that are necessary or useful for the building of MAVs. Several more basic building materials were used regularly in the CMAVS laboratory at WSU which provided a toolbox of design tools available for a



Figure 2.5: Metal Gear Train

researcher/designer. Typical stabilizer and control surface material was provided by balsa wood and or foam which has good stiffness and strength to weight ratios. Foam can be more forgiving in the event of crashes but may not be aesthetically pleasing as the balsa wood. Depending upon the amount of finesse desired for the vehicle, lightening holes in the stabilizers were cut and covered with Mylar. Mylar is a thin plastic sheet that is available in several thicknesses beginning at a thickness of $2 \mu\text{m}$ which has a mass of $2.2 \text{ grams/meter}^2$ (g/m^2). Frameworks have also been made from carbon fiber rod and super glue, then covered with Mylar. Super 77 Spray Adhesive is used to glue the Mylar to the wood, foam or carbon fiber. Typically, only minor masses can be saved using such techniques, however, the look of the vehicle can be dramatically changed and every small drop in mass helps.

Several super glues are available from hobby stores. Laboratory preference was to use the Super-Gold+ 10-25 second dry time and gap filling. This particular glue is some thicker than other available but always provided good results. This glue used with Insta-Set is a priceless tool to have when using the super glue. Addition of the Insta-Set to wet glue will virtually instantly cure the glue. It should be noted that the glue and curing agent must be used carefully around electronics as several receiver boards were ruined by these items. Furthermore, the curing agent is a thinner that will de-bond the Super 77 spray adhesive from the wood, foam or carbon fiber if it comes into contact. Un-Cure is also available from most hobby stores. This product will aid in softening and removing the super glue in

the event of a mistake building.

Carbon rod, tube and shapes can be purchased in sizes as small as 0.010 inch for rod and 0.028 inch OD, 0.011 inch ID for tubing. The Composites Store found online at cstsales.com has a wide variety of carbon fiber products from pre-cured shapes to pre-preg tapes to bare carbon tow. These rods and tubes can be used for parts such as push rods for control surfaces to stiffing rods for foam. Stainless steel needles can be found from several suppliers. Possible the easiest to navigate is McMaster-Carr whose assortment of dispensing needles ranges from 14 gauge to 30 gauge stainless steel needles. These have been used by the WSU laboratory for push rod ends, gear shafts and many other uses. In addition to the stainless needles, McMaster-Carr also has 5 sizes of Teflon needles that may suit a particular need.

Micro bearings can be purchased as small as 1 mm ID, 3 mm OD and 1 mm face width also described as 1x3x1. These bearings can be found at several hobby sites on the web, reliability goes up significantly when the bearing size is increased to the 1.5x4x1.2 bearings. This one size larger bearing is better suited to handle higher speeds and off-axis loading. The WSU laboratory has gone through hundreds of 1x3x1 bearings falling apart during testing and flight. Loctite 680 is a slip fit retaining compound that works very well at holding outer races of bearings to housings and even pinion gears on drive shafts. The retaining compound has been successfully used to hold a 1.5 mm hole to shaft with only a 2 mm face width. If removal is necessary and force cannot remove the compound, heat aids in release. Be careful of any motor magnets as they will lose their effectiveness if exposed to too much heat. In addition to micro bearings, hardware such as screws and nuts can be purchased. Typical sizes purchased by the WSU laboratory are M1, 0-80, 00-90, and 000-120 having diameters of 1.00 mm, 1.51 mm, 1.19 mm and 0.86 mm respectively.

2.7 Four-Bar Mechanisms

Flapping wing mechanisms require an oscillating actuation to flap the wings. Some research groups have done this via means of piezoelectric actuators [33, 34, 50, 64]. These actuators require high voltage and low current, the opposite of what is available from the

Li-Po power sources. Therefore the rotary motion of low voltage, high current motor is required to be converted to an oscillatory motion, to use the capabilities available from the battery power sources. This is commonly done via means of a crank-rocker four-bar mechanism. The principal components of a crank rocker mechanism are the coupler, rocker, ground link and crank. The crank is driven by the motor either directly or through a gear train. As discussed previously, flapping wing MAVs typically require a gear train to increase torque from the motor to accommodate the large loads given by the wings. The crank is then pinned to the coupler, and the coupler pinned to the rocker. The rocker and the crank are both pinned to the ground link. The resulting motion allows a continuous rotating motion of the crank to result in a oscillatory motion of the rocker. The positioning and sizing of the crank, coupler, and rocker can drastically change the output velocity profile of the rocker given a constant crank angular velocity. Figure 2.6 shows the four types of four bar linkages. For purposes of micro air vehicles the second picture from the left, or the crank-rocker, is the obvious choice due to is conversion of full rotational motion which occurs due to an electric motor to an oscillatory motion which can be used to drive the wings.

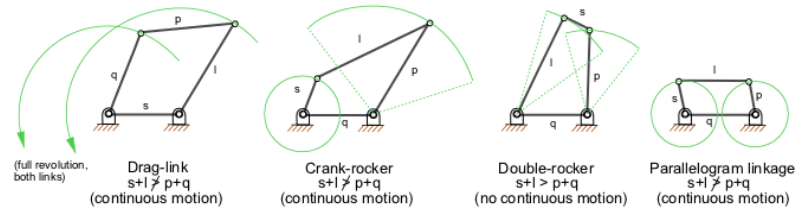


Figure 2.6: Types of Four Bar Linkages [75]

Notice that the axis of rotation of the rocker stroke is parallel to the axis of the crank or motor rotation. The requirements for a four bar mechanism to be a crank rocker is that crank and coupler length added must be smaller than that of the ground and rocker links added.

Due to the nature of the four bar mechanism, the velocity profiles are not equal from

the forward stroke to the backwards stroke. It is possible to make the duration times equal but this will not make the velocity profiles equal. Some mechanisms take advantage of the time ratio created by these velocity differences. The time ratio is a measure of the quick return of the mechanism and is defined in Equation 2.1.

$$Q = \frac{\text{Time of Slower Stroke}}{\text{Time of Quicker Stroke}} \geq 1 \quad (2.1)$$

The quick return can be used to flap fast down and slow up. Kinematics can be calculated using the geometry of the planar four bar linkage. The link lengths of the mechanism determine the kinematics that the mechanism provides. To determine the velocity profiles of the mechanism a MATLAB code was developed to calculate the position of each member in the four bar mechanism as the crank gear was indexed 360 degrees. The code can be found in Appendix B. Providing a crank angular velocity or velocity profile, the rocker arm angular velocity and acceleration can be calculated. Using a step-wise method there are two points where the equations must be solved more directly due to the crank aligning with the ground link. When calculating the rocker angle, one must be mindful of the location of the crank in relation to the ground link. The geometry changes when the crank is between 0 and 180 and 180 and 360. The velocity profiles will be used in Chapter 3 to calculate blade element theory lift and drag forces and related to vehicle forces and moments.

2.8 Computer Aided Design (CAD)

Computer Aided Design utilizes computer software to design two and/or three dimensional objects. Solidworks, Pro Engineer, and Autodesk Inventor are three of the more popular professional CAD software entities on the market. These programs allow the user to save multiple data types for the given parts and assemblies, so they can be used in other software for part manufacture. From the generated parts and assemblies the next step of creating the parts can be performed. If using a 3D printer, the parts can simply be added to the printer's software for orientation, sizing and support material processing. If machining will be performed, the parts can be uploaded to a CAM program to make tool paths and post

process G-code.

Gears can be a difficult item to CAD. Solidworks does have a built in gear software add-in which can make an assortment of gear modulus' with any desired amount of teeth. The convenience is astronomical when a program will correctly CAD the correct gear tooth involutes versus attempting to correctly draw them in the CAD software. Additionally, a software sold by Camnetics named GearTeq can be used to generate part and assembly files from the user input data in the software. The software can create spur, helical, rack and pinion, bevel, worm, and even planetary gear sets. This software was used to design the bevel gear set used to amplify the rocker motion. The full gears were then modified in Solidworks to provide the sectioned gears that are used on the FWMAV.

2.9 Summary

FWMAVs require many tools, materials and parts to generate a flapping much less flying vehicle. Combining the aforementioned into a working vehicle is becoming easier namely due to the hobby industries drive for better motors, servos, batteries and electronics. Utilizing the COTS items are crucial to allowing researchers the ability to investigate physics of flight vs. the vehicle itself. Without these, a substantially larger effort lay for developing the control boards or batteries or motors than desirable. The utilization of COTS items and other tools such as 3D printers, CNC mills and wire EDM have allowed for the development of a vehicle shown in Chapter 3.

DESIGN

3.1 Introduction

Many considerations must be weighed when determining a particular flapping style. First, what is the desired mission or characteristics of the MAV? Should the vehicle be hidden in plain sight? In how small of a space must the vehicle fly? Is there a maximum speed that must be reached or a minimum distance to traverse? Does the vehicle need to maintain a long duration on a charge? Or do you just want to show that you could make something fly! While all of these questions may never be answered and a craft fulfilling all the desired needs is basically impossible to produce with the given technology available, where does one start? Birdlike flappers, while successful, add relatively little to the world of flight compared with the distinct advantages offered by insect-like flapping. Typically, birdlike flappers are capable of flying slower than a fixed wing airplane but faster than a multi-rotor vehicle. One major consequence of multi-rotor vehicles is the audible presence compared to the flapping wings, though flapping wing vehicles are far from quiet. Horizontal flapping has the possibility to allow a vehicle to achieve the much desired snap acceleration, hover, vertical takeoff and landing, and hidden in plain sight qualities that are so desired out of MAVs. Choosing a flapping style is just the beginning of the research effort towards a flight worthy vehicle, but may provide the a good starting point to achieve aforementioned desirable traits. The following is an in-depth review of the methods used to design, manufacture and build flapping wing micro air vehicles.

The design of a flight worthy micro air vehicle is a delicate balance of experience, knowledge, custom design and manufacturing, testing, and patience. Personal experience in manufacturing, design and flight was first gained building and flying birdlike flapping

MAVs. These vehicles use the wings for thrust with a rudder and elevator for control. The vehicles perform quite well, several videos of such flights can be found on youtube.com by searching for “WSU MAV”. A more capable and natural vehicle was desired, the new design began with the approach of horizontally flapping wings. The design of the model began with the bio-inspiration from ladybugs, bumblebees and wasps to name a few. The attributes viewed in high speed video of such insects, matched with the attributes and invaluable lessons learned which enabled the birdlike flapper to fly. The first design developed a crude CAD model, which was modified to accommodate a basic four bar mechanism coupled to an amplified flapping mechanism. The CAD was modified for flight weight by lightening the gears, developing a lightweight aluminum frame and shrinking the footprint as much as the design will allow. Early iterations began with plastic 3D printed frames and gears to provide concept validation of drive mechanism and fundamental flapping concept. Lift and control tests were performed early in the design cycle to evaluate lift to weight comparisons for non battery powered models. Furthermore, high speed video capture was used to evaluate wing motion, sizing and stiffness using the novel driving mechanism. While control was absent, the bench model showed promise for a high lift to weight mechanism. Simple tails were attached during early testing and indicated that simple flap control surfaces similar to elevator-rudder designs would not suffice independently for the horizontal flapping mechanism. Early designs which could be printed in short order and assembled in an hour evolved into designs requiring weeks of manufacturing and assembly to produce one FWMAV. The most complicated design incorporated four channels of control directly into the flapping wings. Independent adjustment for angle of attack were provided via two servo motors. The next generation of mechanical control added a means of adjusting the flapping plane to make roll adjustments.

3.2 Inspiration

A major design tool used for the inspiration and design of micro air vehicles is to learn from nature. The two wing mechanism was bio-inspired specifically by the ladybug flapping style. The basic flight characteristics of the ladybug were investigated via high speed video,

of which samples of the can be seen in Figure 3.1.



Figure 3.1: Ladybug Flapping Cycle

It can be noted from Figure 3.1 that the lady bug has flapping amplitudes of 180 degrees and that the wings passively deform under aerodynamic and inertial loads. Many researchers have discovered the necessity of flexible wings [29,31,58–60,63]. An investigation into the wings was done drawing from insects and varying wing venation and stiffness to acquire a wing with desired flapping deformations, durability and lift [66]. The intention of using a freely deforming wing is to attempt to achieve the lift enhancing characteristics often found in nature being namely, delayed stall, rotation circulation, wake capture and clap and fling interaction [31, 52, 76]. When investigating the wing motion of insects, one can quickly see the fluid nature of their wings. Every stroke is extremely smooth through

stroke and transition. This quality is highly desired for FWMAVs for several reasons. A smooth stroke and transition is audibly quieter, less damaging to all parts of the mechanism from motors and frames, to electronics and wings, and provides a balance, efficiency and gracefulness that nature has self tuned for all of its flying insects and birds. Even the seemingly violent flapping of a hummingbird when inspected with high speed video is smooth through stroke and transition.

3.3 Evolution of a Horizontal Flapper

The CAD design aided in determining required crank and coupler lengths as well as overall vehicle design. The model has been developed from a 6 mm brushless motor with plastic frame and gears to a design requiring two 13 mm brushless motors with full aluminum frames and gears. The design was modified for basic flight capability, i.e. having a lift to weight ratio greater than 1, and having control for six degrees of freedom. The basic design consists of a 15:1 gear ratio from the motor to the crank gear. The crank gear drives a planar four bar mechanism to achieve the oscillatory motion. The oscillatory motion is then amplified to achieve a large flapping amplitude of 180 degrees, which is not realizable with only a four bar mechanism. In addition to the ability to reach larger amplitudes, the mechanical advantage of a four bar mechanism can be drastically reduced when large angles occur on the rocker. The amplification mechanism rotates the axis of oscillatory motion 90 degrees, allowing the gear train and motors to be underneath of the wing stroke plane.

Figure 3.2 shows two examples of the motor and wing stroke axis being parallel by means of the wing spar being directly connected to the rocker link. For the four wing flapper, developed by WSU MAV group and the author is pictured in Figure 3.2(a), it orients the motor toward the rear of the vehicle during forward flight. Furthermore, the wings do not flap a more than 60 degrees leaving plenty of room for the reduction gears and motor to fit below the wings when flying forward. The flapper in Figure 3.2(b) was developed by AFRL [77]. It also uses the rocker linkage to drive the wings. In this orientation the frame and linkages remain in the stroke plane. A planetary gear-set was used to reduce torque

seen by the motor. This gear-set is inline with the motor and requires no large gears to be in the stroke plane. Even with the significant reduction of these gears, the wing plane area has significant obstruction due to the frame and four bar linkage.

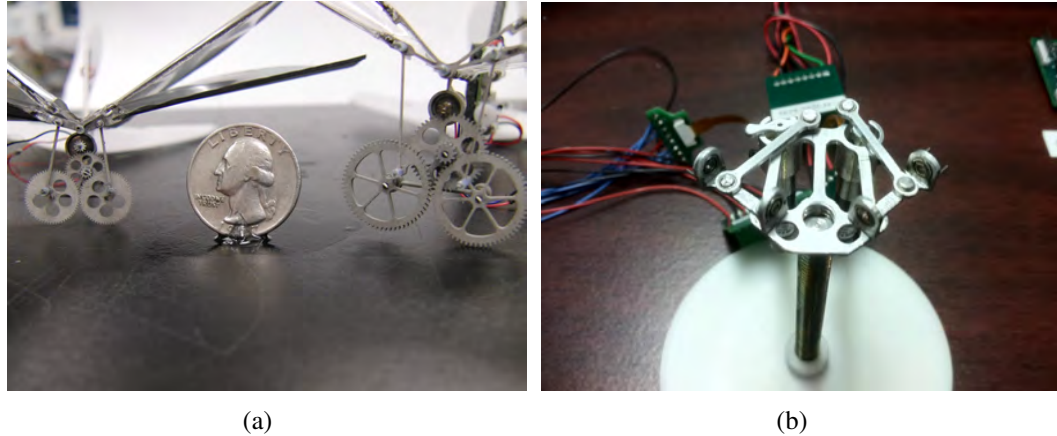


Figure 3.2: Rocker Linkage Drives the Wings Stroke Rotation [77]

3.3.1 Achieving Large Flapping Angles

The basics of the four-bar mechanism allow for a limited rocker angle amplitude. Previous flappers used the rocker arm as the wing spar. While this is desirable to reduce complication, large flapping angles were necessary to better imitate certain insects in nature. Although achieving a rocker angle of 120 degrees and even larger is possible with a planar four-bar linkage, the torque angles start becoming very poor at the reversal point, wasting precious energy and causing unnecessary wear and tear on the mechanism. The geometrical limit is less than 180 degrees for a conventional four bar mechanism. By adding a secondary gear-set to amplify the rocker motion, the link angles can be chosen to restrict rocker angles to more desirable ranges. Figure 3.3 shows a conceptual sketch of the design. Two major advantages are maintained when smaller angles are used for the four bar mechanism: the poor torque and harsher mechanism forces are reduced as well as the ability to create a more symmetric flapping cycle given a constant crank speed. While the quick return of a four-bar mechanism can be advantageous in many circumstances, in a horizontal flapping orientation it only hinders the balance and trim of a flapping wing vehicle. Flap-

ping faster fore than aft can cause translation and pitching problems that must be corrected by a means of control. Minimizing the quick return can allow the mechanism to begin in a more trim position allowing the control scheme greater authority and a more efficient mechanism.

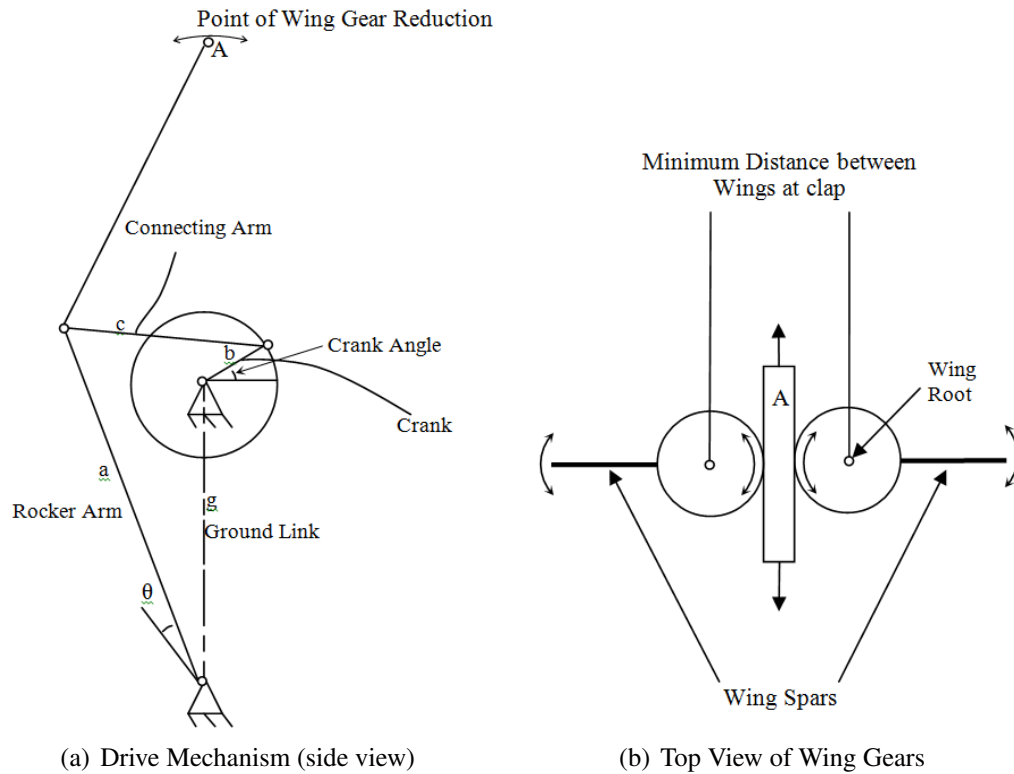


Figure 3.3: Conceptual Sketch of Mechanism

Utilizing GearTeq software allowed for quick manipulation of gear teeth number and pitch to achieve the desired geometry. The amplification gear design uses a bevel gear-set, with a ratio of 330 to 29. This gear ration was chosen to achieve the desired geometrical constraints while maintaining reasonable gear tooth thickness and size. The resulting rocker angle was then approximately 15.8 degrees of total amplitude generating the amplified wing amplitude of 180 degrees. Additionally, the bevel gear set rotated the flapping plane by 90 degrees allowing the gear train to be placed directly underneath of the wings axes of rotation. The bevel also helped increase the pressure on the gear teeth with larger wing load. As the wing loaded upward, the moment generated on the wing gear causes greater pressure between the gears ultimately reducing the risk of skipping and wearing

the gear teeth. Two of the 29 tooth gears were used to sandwich the 330 tooth gear which was made double sided, each side of the gear drives one wing. The rocker was designed to insert into the gear and drive it fore and aft of the flapper, in turn flapping the wings. Figure 3.4 shows a zoomed picture of the gears with wing spars and rocker arm inserted into the “wing gears” and the double sided sector bevel gear. An aluminum strap was precision machined on a wire EDM to achieve consistent gear spacing.

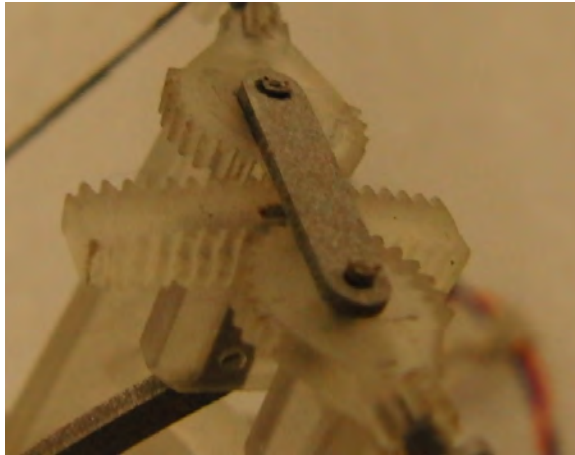


Figure 3.4: Double Sided Bevel Gear Sets

The basic geometry of the bevel gear set required the center of rotation of the 330 tooth gear to be 40.0 mm below the bottom surface of the 29 tooth gear. The 29 tooth gear had a diameter smaller than 5 mm so that a double sided gear could be mated between two 29 tooth gears and maintain the rotational axes at 10.0 mm apart. The 29 tooth beveled gears were then modified via the CAD program to accommodate the insertion of a wing spar and removed 14 of the gear teeth since the gear would not make full rotations. The 330 tooth gear was modified to accommodate the 29 tooth gears wing spacing by adjusting the gear thickness and mating two back to back. The gear was then cut down to only 16 teeth with an added extrusion and hole for mating. The rocker arm of the four bar mechanism was inserted into the extrusion hole. The rocker arm and sector bevel gear were designed to fit fully bottomed out to avoid assembly error resulting in poor tooth engagement being either too tight or too loose. Fine adjustments were made to the 330 tooth gears thickness to tune the gears contact pressure. Trial and error works incredibly well with the aid of a

high precision 3D printer, CAD software, and easily assembled vehicles. Iterations allowed for sufficient pressure to avoid gear teeth breaking but low enough to provide smooth, low friction interaction.

Later models decreased the number of teeth and increased the pitch so that gear teeth were large enough to be machined using a wire EDM. This became necessary when the drive motor became significantly more powerful which compromised plastic gears structural integrity.

3.3.2 Vehicle Kinematics

Flapping kinematics are dependent on the geometry of the four bar mechanism. The four bar mechanism found in the vehicle has a 25.08 cm rocker, 2.5 cm crank, 15.5 cm coupler, 24.0 cm ground link corresponding to links a, b, c and g respectively from Figure 3.3(a). Four bar mechanisms are commonly known for their quick return which can be calculated from Equation 2.1. The mechanism here flaps fore and aft thus a symmetric flapping stroke is desirable. It can be imagined that a bird that flaps up and down would prefer to flap downward faster than upward, thus the quick return could be designed into the flight concept. While the quick return can be minimized, and even eliminated, the four bar mechanism will still have asymmetry in the velocity and acceleration profiles. Correction for this must be done either with control authority or wings with asymmetry in stiffness from fore to aft flaps. The advantage to using the amplification method to make the four bar mechanism flap larger is to make the four bar kinematics easier to manipulate. A large amplitude four bar will also lend to worse mechanical advantage angles and are more prone to out of plane motion, thus a low amplitude mechanism was made and amplified. Figure 3.5 is shows the geometry for the crank, coupler and rocker linkages, colored in blue, red and black respectively, for every 10 degree step of the crank linkage. The green line represents the ground link.

Figure 3.6 is a graphical representation of the symmetry/asymmetry of the mechanism containing the crank angle vs. the normalized wing angle. Red lines indicate the zero wing angle and midpoint of the crank cycle. Ideally, for a time ratio of 1, the blue line would

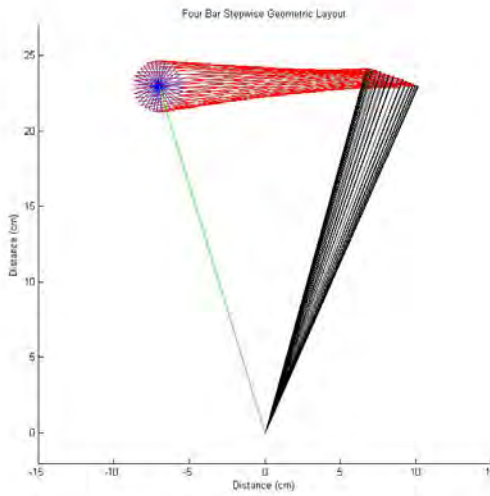


Figure 3.5: Four Bar Linkage Incremental Geometry

cross directly at the intersection of the two red lines.

Angular velocity and acceleration profiles for this mechanism can be seen in Figures 3.7(a) and 3.7(b), respectively. The propagation of a potential problem, can be seen in the velocity and acceleration profiles in larger amplitude mechanisms. Figure 3.8 shows two larger 52 degree and 88 degree flapping amplitudes of which are not half of the desired amplitude. Angular position of the rocker relative to the crank appears similar to the that of the low amplitude mechanism. Further investigation into the velocity and acceleration shows the problem more evidently. Figures 3.9(a) and 3.9(b) show the normalized acceleration profiles for larger amplitude four bar mechanisms. Figures 3.10(a) and 3.10(b) show the normalized velocity profiles for larger amplitude four bar mechanisms.

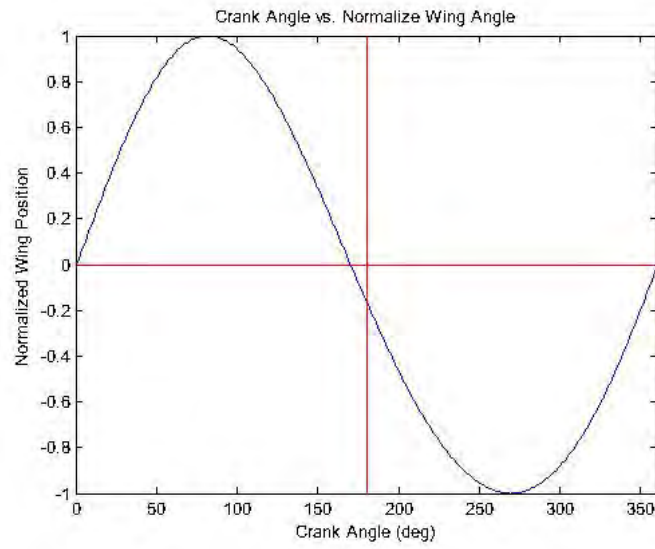
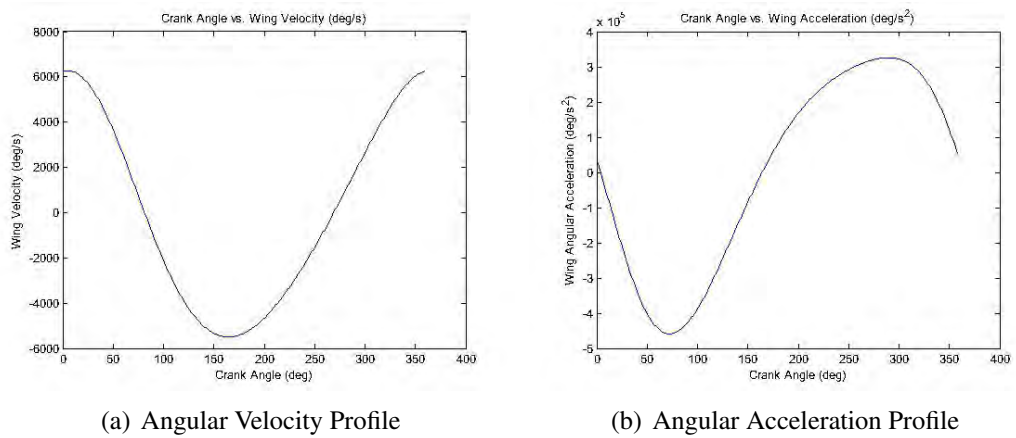


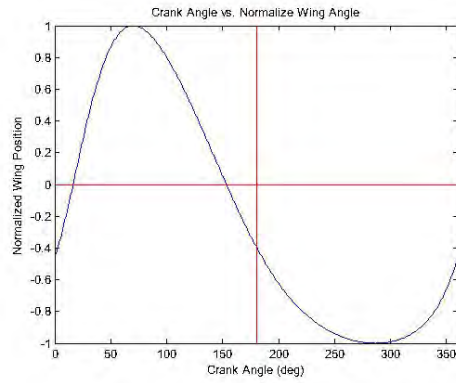
Figure 3.6: Mechanism Kinematics, Crank Angle vs. Normalized Wing Angle



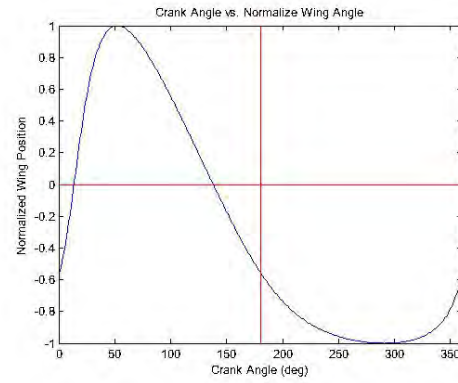
(a) Angular Velocity Profile

(b) Angular Acceleration Profile

Figure 3.7: Angular Velocity and Acceleration of Rocker Arm

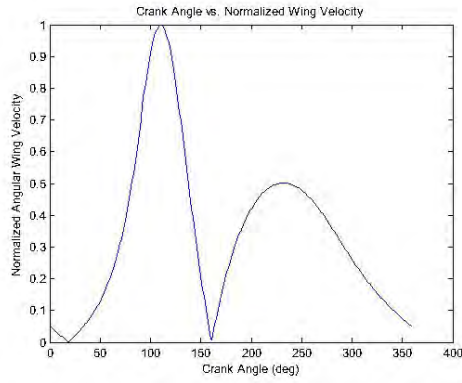


(a) 52 degree Amplitude

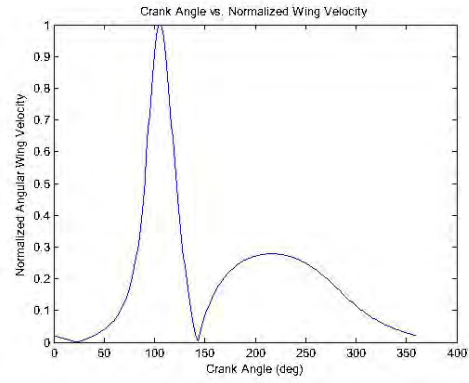


(b) 88 degree Amplitude

Figure 3.8: Normalized Angular Position of Larger Amplitude Mechanisms

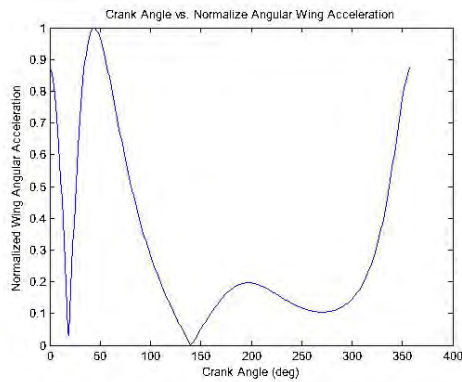


(a) 52 degree Amp Normalized Velocity

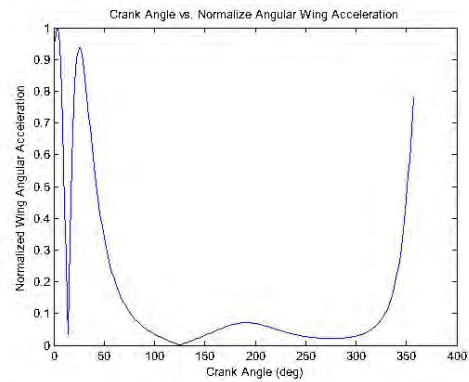


(b) 88 degree Amp Normalized Velocity

Figure 3.9: Normalized Absolute Value Angular Velocity of Larger Amplitude Mechanisms



(a) 52 degree Amp Normalized Acceleration



(b) 88 degree Amp Normalized Acceleration

Figure 3.10: Normalized Absolute Value Angular Acceleration of Larger Amplitude Mechanisms

In addition to the kinematics associated with the four bar mechanism, the wing flapping amplitude has a major effect on the efficiency of the mechanism. The position, velocity and acceleration plots for individual mechanisms utilizing different levels of amplification are shown in Figure 3.11. The mean acceleration of the 120 amplitude is 50% higher than the mean acceleration of the 180 amplitude and the 150 amplitude is 20% higher than the 180 amplitude. This illustrates the importance of large flapping angles and is not specific to one four bar mechanism. Several mechanisms were simulated and all showed cycle average accelerations decrease with larger flapping amplitudes. An increase in angular acceleration is a direct increase in motor effort from a purely inertial standpoint. It is naturally important to consider the quick return generated by a large amplitude four bar and consequently the maximum acceleration, however, without some means of amplifying a four bar mechanism, one should not expect any amount of efficiency from the mechanism due to very large accelerations inherent to four bar mechanisms as well as reduced flapping angles. A 90 degree flapping amplitude should expect half of the velocity squared and thus half the lift at the same inertial load compared with a 180 degree flapping amplitude. This relationship is independent of mechanism four bar design. While not quantified experimentally, this trend was found to be true for several four bar mechanism's calculated kinematics as well as in vehicle designs. The general concept follows that less reversals of the wing will lead to less load on the motor for a given cycle averaged velocity.

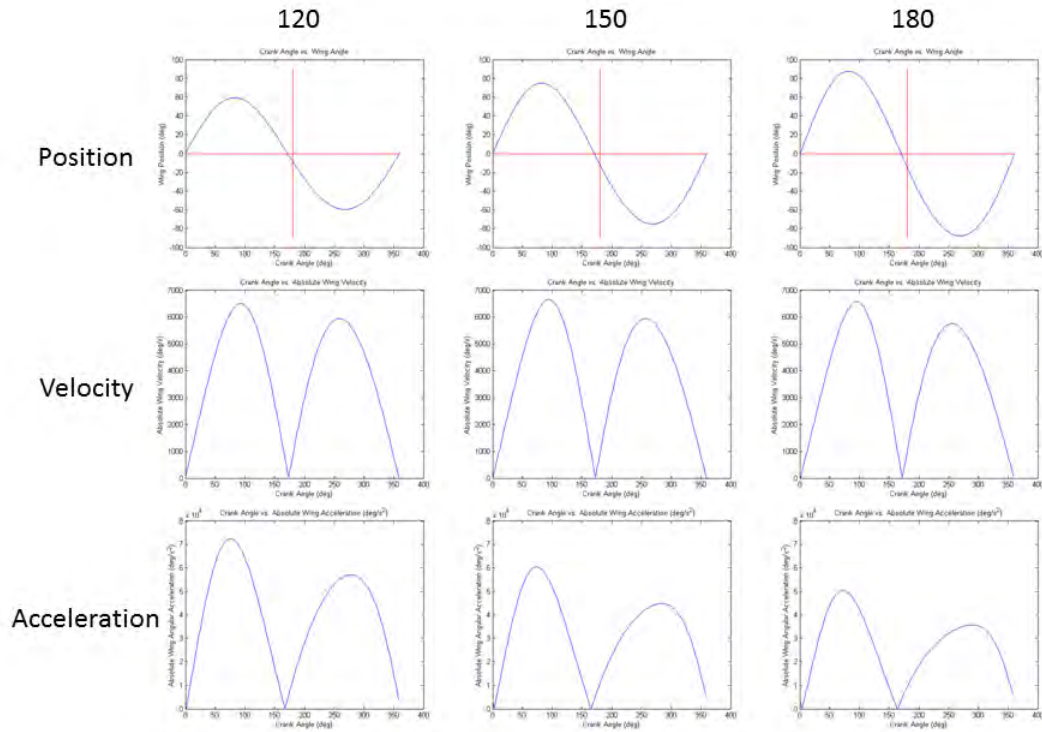
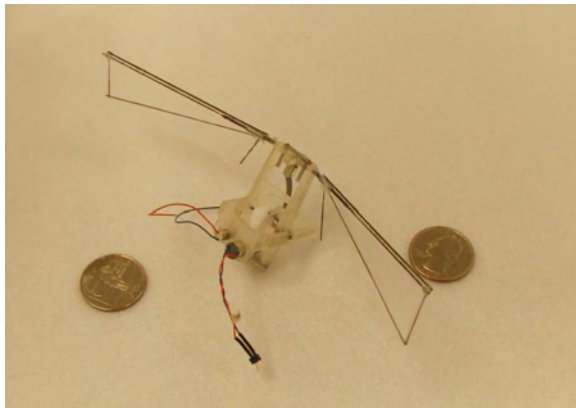


Figure 3.11: Mechanism Kinematics for Flapping Amplitudes and Frequencies

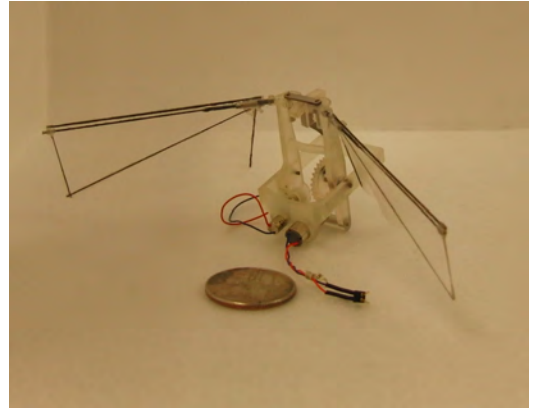
3.3.3 Pitch Controllable 180 Degree Amplitude Flapper

The first version of the horizontal flapper utilized a two piece frame which allowed the motor to rotate about the drive gear by means of a servo motor. The motor drove the crank gear by means of a worm gear, the idea being that worm gears provide large gear ratios with only one gear-set. Prototypes were built but were not successful due to the large friction generated by the worm gear set when made from the 3D printed plastic EX200 on the 3D Systems Projet 3000 HD. Part resolution was good, however, even with oil lubricant the gears were too difficult for the high speed, low torque coreless motor to turn.

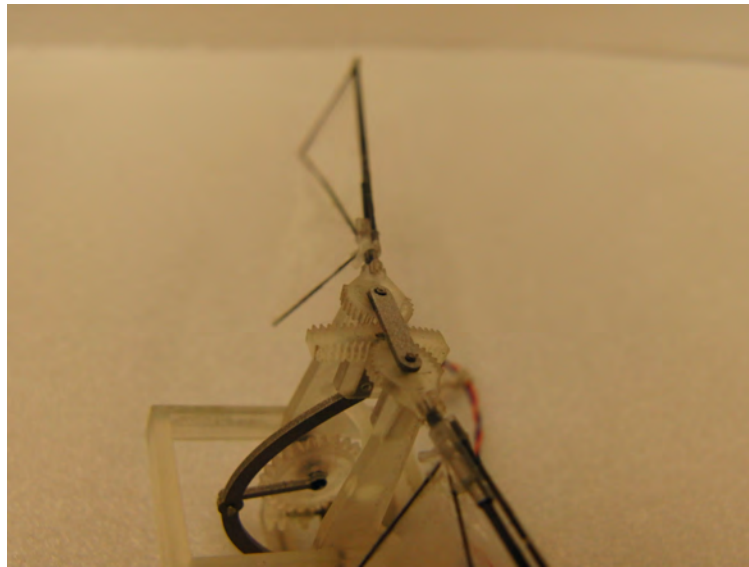
While the drive gears did not work, the wing amplification gear-set seemed to work well. The wing rotation points were designed to be only 10 mm apart, aiding in reducing the wingspan of the vehicle. The rocker, coupler and bevel gear-set can be seen in Figure



(a)



(b)



(c)

Figure 3.12: Version 1 of Horizontal Flapper

3.12(c).

3.3.4 Version 2 Lift Off

Although version 1 proved to have too much friction in the worm gear set, it did show promise for the wing amplification concept. During the redesign, the pitch control was dropped in favor of a spur gear drive train. The motor was turned 90 degrees so its axis was parallel and below the mid-stroke axis of the wings. The compound gear set was made out of plastic to provide sufficient torque to flap the wings. Preliminary gear sets ranged from 30:1 to 10:1. Desired frequency, wing size and stiffness, motor capacity, motor safety, battery discharge rate, and geometry considerations are some of the factors that contribute to the gear ratio chosen. Purchasing COTS gears will further limit the selection of gear ratios due to limited selection for both tooth number and gear modulus.

The design for this iteration of the model used 3D printed gears which aided in quick turnaround of models providing ease for trial and error gear combinations. Several gear ratios were used to drop current to a reasonable level that the intended small batteries could provide while generating sufficient torque and speed to lift the vehicle. Vehicle preliminary designs always began hanging from a tether and powered with a table top power supply via long small gauge wire. The power supply gives indication of current and voltage required to lift the weight of the vehicle. Too much current means a larger gear ratio is necessary. If a vehicle requires full cell voltage to lift the vehicle, a smaller gear ratio may be necessary to draw more current but generate higher frequencies. It is also possible that a more efficient and/or larger motor may be necessary to generate the required power to lift the vehicle. While a larger motor is heavier and requires a larger battery and typically requires heavier, more capable electronics, it is sometimes a necessary option which allows for more experimentation in the structural design of the vehicle. Furthermore, larger motors tend to provide a slight gain in efficiency. Gears were cantilevered off of the frame using two bearings to support the gear load. Vehicle weight was near 7 g and did not include the receiver or battery. Figure 3.13 shows snapshots from a high speed video of the tethered model lifting itself. Flapping frequency in the snapshots is approximately 20 Hz. The snapshots show approximately 0.2 seconds of real time flight. Lift results were impressive, however, more payload was necessary to accommodate control boards, batteries and control mechanisms

which required the use of a larger motor.

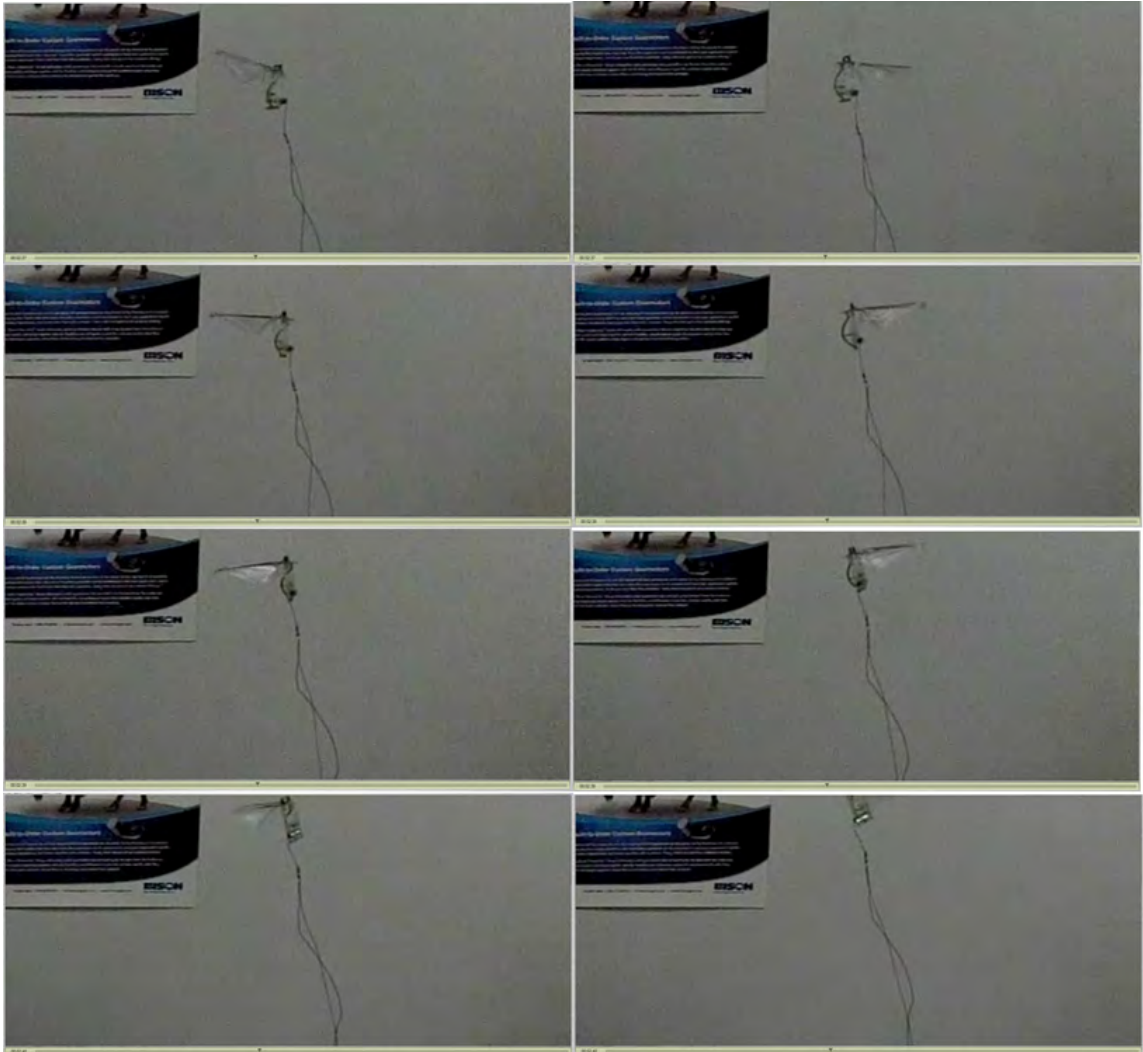


Figure 3.13: Snapshots of High Speed Video of Tethered Flight

3.3.5 Mechanical Design

The larger design presented here shows a recent version of the vehicle that utilizes a 3.5 gram brushless motor. The mechanism is built for testing wings and only has control over the motor effort. The model has a 17 mm diameter base that is used to mount to an ATI Nano-17 load cell. The overall vehicle is 57 mm tall, 27 mm by 32 mm wide. The bounding dimensions are shown in Figure 3.14. The purple cylinder is the out-runner housing for the

motor. The coils and shaft housing are co-linear and to the left of the purple housing in Figure 3.14(b).

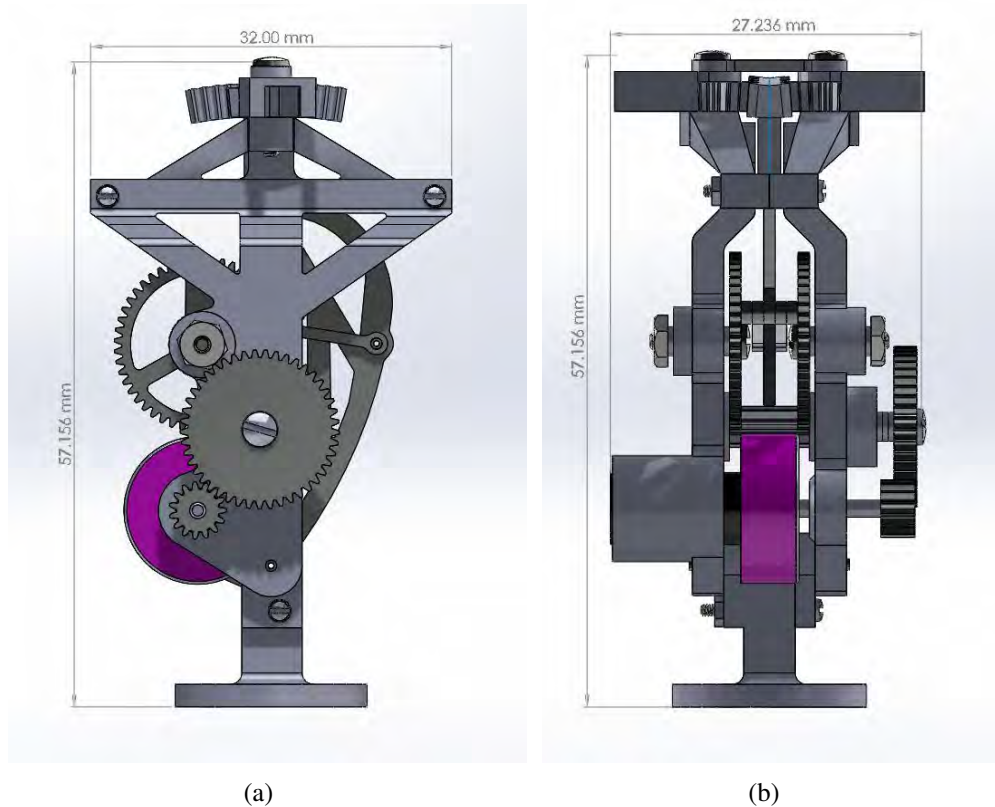


Figure 3.14: Horizontal Flapper Dimensions

A sectioned isometric view can be found in Figure 3.15. Figure 3.15(a) is a full isometric view of the vehicle. In this view the gear-set on the side of the vehicle is in plane view. Figure 3.15(b) is a sectioned view that removes the first drive gear-set and exposes the right side frame. This frame is made out of 3D printed plastic and is designed larger to provide a more robust frame for bench test reliability. Three bearing sets are exposed, the motor shaft bearing, compound gear-shaft bearing and left side crank gear-shaft bearing. Also notice that there are two gears located just above the purple motor. Two gears are used to provide a symmetric force on the rocker arm and prevent twisting which would flap one wing with a larger amplitude than the other. The double crank gear-set provide a significant increase in reliability reducing shaft and pin bending. Reliability increased in the bearings, pin joints and gear wear. Figure 3.15(c) is a section view that removes the right side frame

and right crank gear exposing the left crank gear, coupler link, rocker arm and the second gear-set. The dimensions of the four-bar mechanism will be discussed later in the section. The rocker is has a sector bevel gear mounted to the top of it. This gear mates with a sector bevel gear on each side of the vehicle. The wings are inserted into the smaller gear.

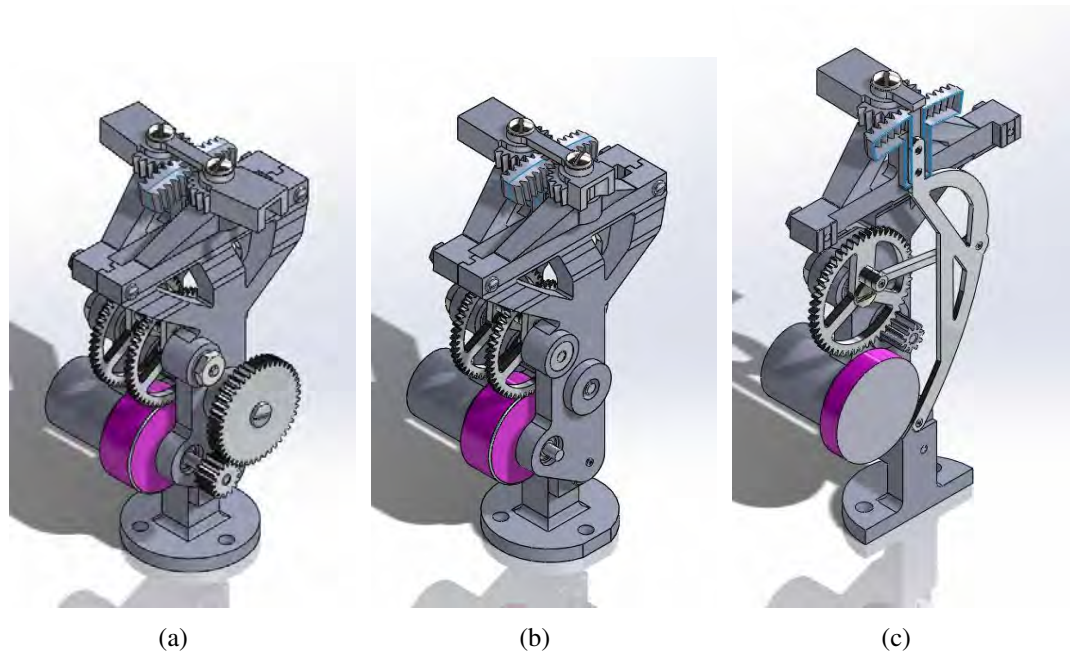


Figure 3.15: Isometric Sectioned View of Horizontal Flapper

Now that the overall size and general concepts for how the vehicle is designed have been discussed, the gear-train is shown in Figure 3.16. There are two reduction gear-sets used to achieve a final gear ratio of 15:1. The first gear-set has a 15 tooth pinion gear on the motor and a 45 tooth gear that is coupled to it. The resulting gear ratio is 3:1. The motor shaft is 1.5 mm in diameter and uses a 1.5x4x1.2 bearing between the pinion gear and the motor housing. The right side 45 tooth gear is directly coupled to the 10 tooth gear. Three 1x3x1 bearings are used to support this shaft. Two bearings are in the gear side of the frame and one supports the shaft on the motor side frame. The crank gear is a 50 tooth gear providing a gear ratio of 5:1 with the compound 10 tooth gear. Each crank gear uses two 1x3x1 bearings that are pressed into the frame. One bearing is pressed in from the outside and one bearing is pressed in on the inside of the frames for each crank gear. The final gear ratio is 15:1 for the motor to the wings after the two gear-sets. Assuming a free run speed

of 33,000 rpm, the theoretical maximum flapping frequency is 36.6 Hz. Changing the 45 and 15 tooth gears allow for relatively easy gear ratio changes. The space is open to allow for vast size changes and can be designed for easy gear removal without changing the four bar mechanism, frame, motor or wing amplification. The critical dimensions are the gear centers and minimum pinion size due to the 1.5 mm shaft diameter on the motor.

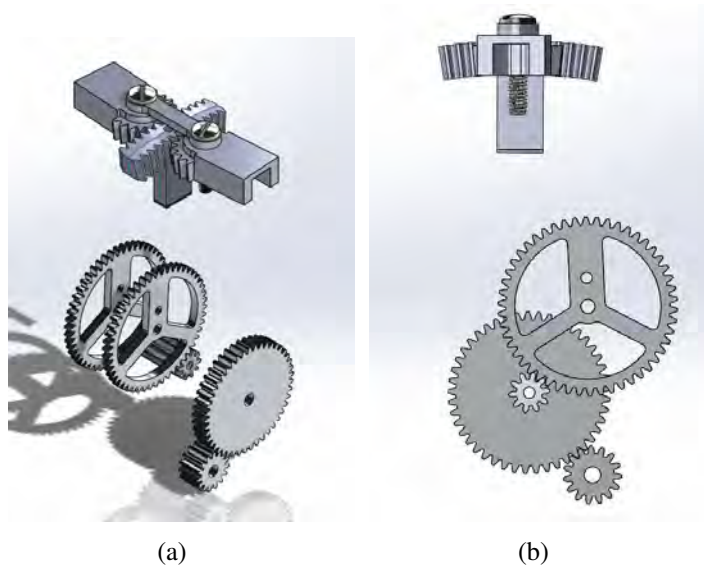


Figure 3.16: Flapper Gear Train

A planar view of the four bar mechanism can be found in Figure 3.17. All dimensions are in millimeters. The crank is 2.5 mm, coupler is 15.6 mm, rocker is 21.8 mm and the ground link is 20.523 mm. The resulting rocker angle sweep is 15.9 deg. This angle is directly coupled to the wings through the sector bevel gear-set that amplifies the rocker. The amplification is 224 to 20 resulting in an amplification of 11.2:1. The multiplied by the rocker angle is 178 deg. The amplification dropped slightly when the gears were redesigned to allow for their teeth to be large enough for wire EDM manufacture out of aluminum. The larger tooth modulus reduced the gear ratio slightly from 11.38 to 11.2.

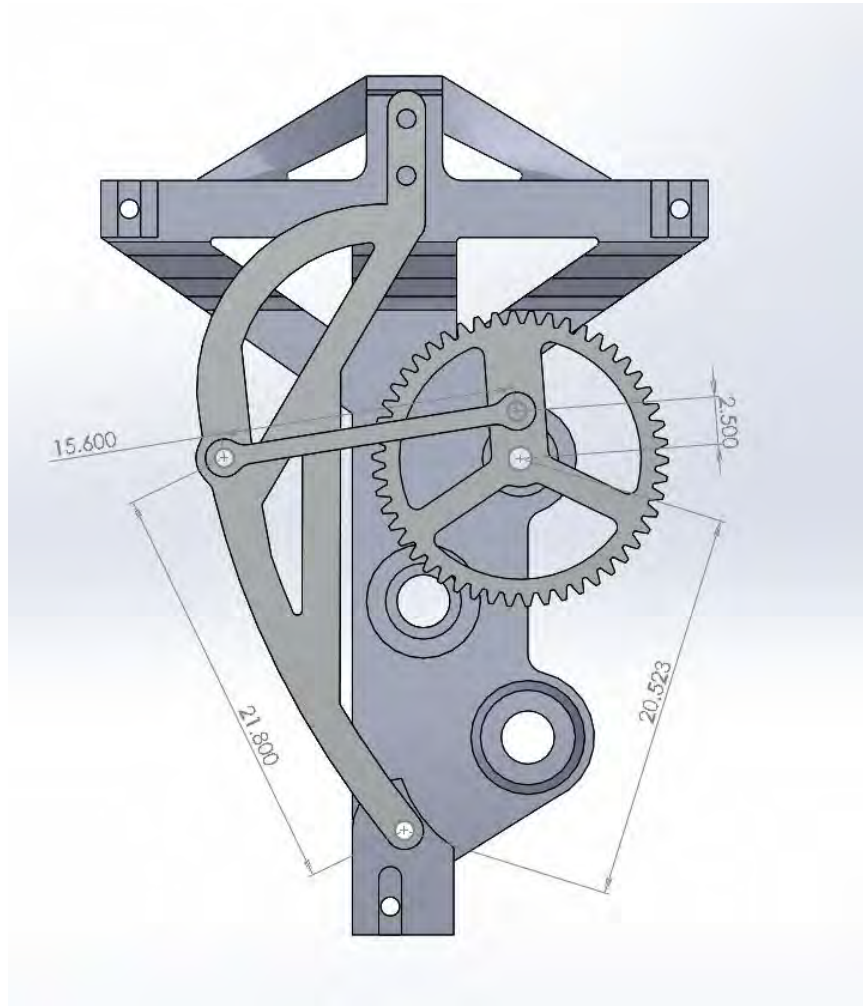


Figure 3.17: Flapper Gear Train

The bevel gear-set was designed such that the rotational axis of the large gear was 39.75 mm from to the bottom of the smaller gear. This distance was sufficient to raise the gear-set above the motor and gear-train and can be found in Figure 3.18. The smaller gear center to face was designed to be less than 5 so the two wing gears could have axis 10 mm apart and can be seen in Figure 3.19. The back to back large gear thickness was adjusted to provide low friction between the two gears and sufficient pressure to prevent the gears from skipping teeth and wearing prematurely.

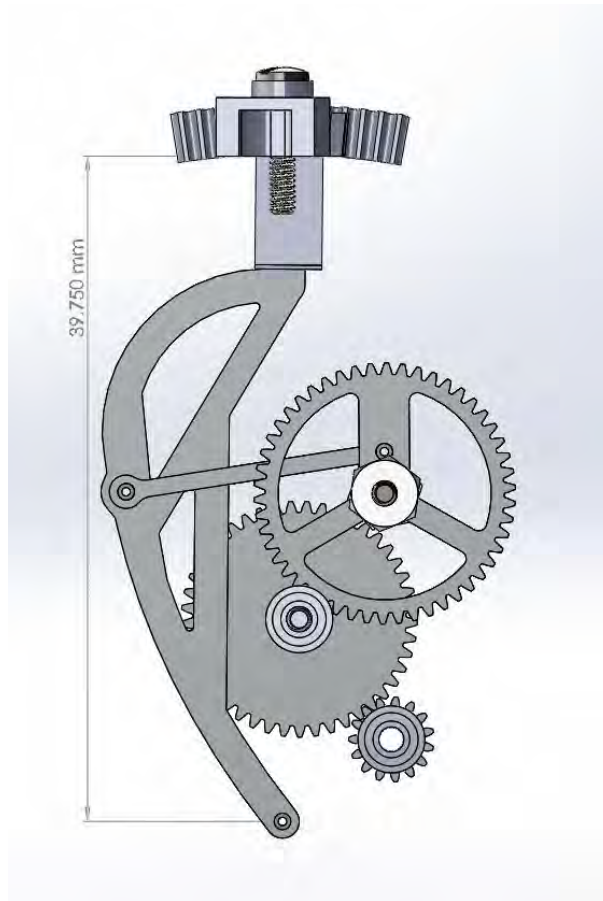


Figure 3.18: Bevel Gear Set Dimension, Side View

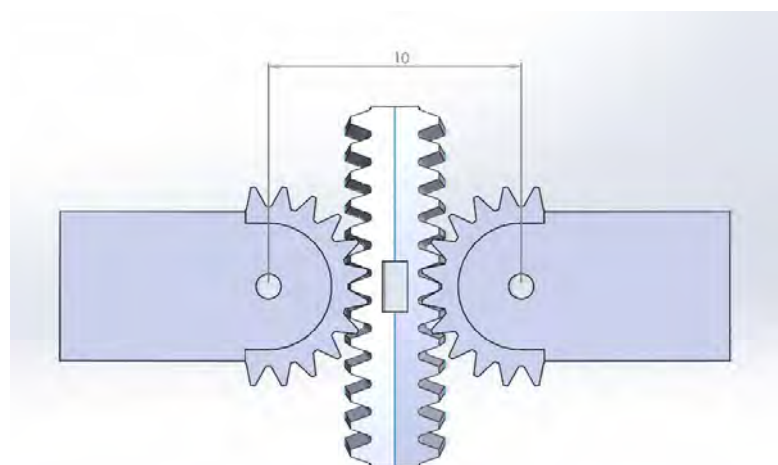


Figure 3.19: Bevel Gear Set Dimension, Top View

Figure 3.20(a) shows the full 224 tooth gear. Figure 3.20(b) is a zoomed in side view of the teeth. Notice that they are slightly angled due to the nature of the bevel gear-set. Due to the large gear ratio the bevel is small.

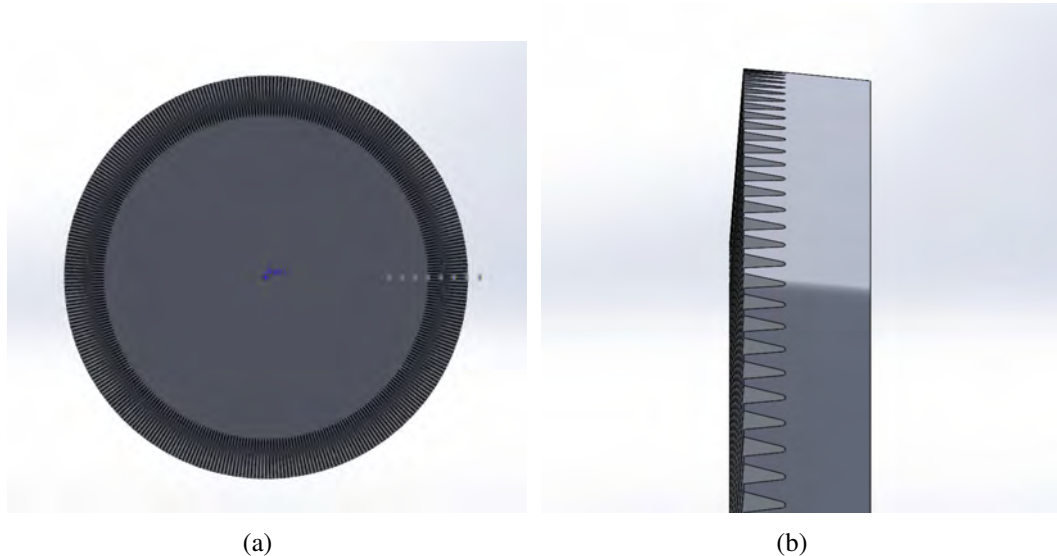


Figure 3.20: 224 Tooth Gear

The gear is trimmed via CAD modeling to reduce to only 19 teeth needed to flap the mechanism. An extrusion is made off the bottom to adjust the height of the gear relative to the rocker arm of the four bar mechanism. This allows for fine adjustment of the gear mates. The piece showing in Figure 3.21(a) is mirrored to produce the final part found in Figure 3.21(b). Thickness can be adjusted to increase or decrease tooth engagement between the two smaller gears in Figure 3.19. Figure 3.21(c) is a bottom view of the final part. The square hole is a 1 mm by 2 mm extrusion that the rocker arm inserts into.

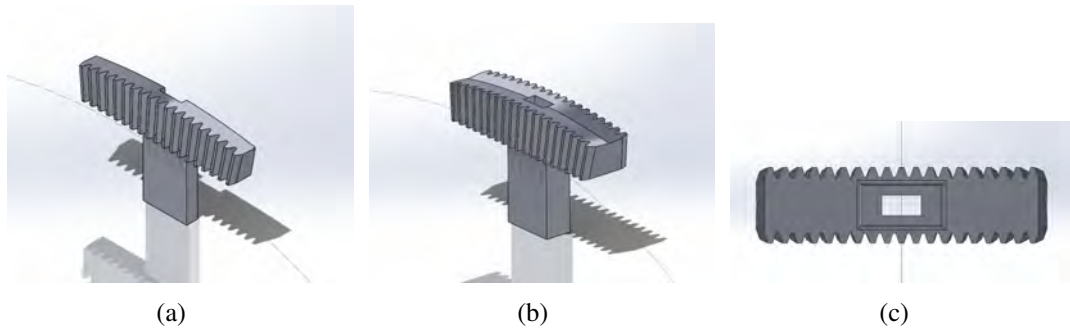


Figure 3.21: 224 Tooth Sector Gear

Figure 3.22(a) is the full 20 tooth gear that mates to the 224 tooth gear. Half of the gear teeth are removed in CAD and the wing interface is added.

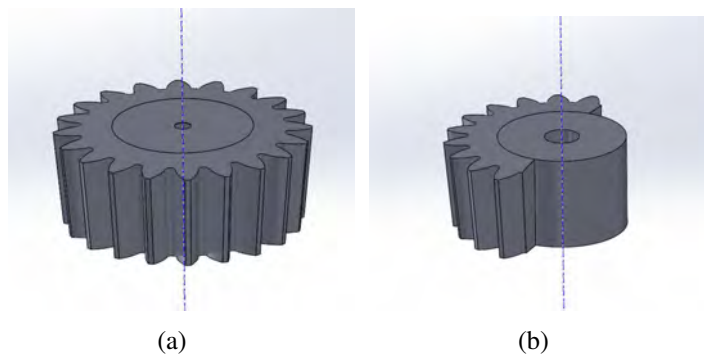


Figure 3.22: 20 Tooth Gear

An insert was made to accept round wing roots and then be pinned into the 20 tooth gear pocket. The gear was made taller to provide extra strength due to the large pocket made for a wing holder. The extra hole found in Figure 3.23(b) allowed for the pinning of the wing holder for easy wing changes. Inserts were 3D printed while the sectored 20 tooth gears were CNC machined from aluminum to provide robustness.

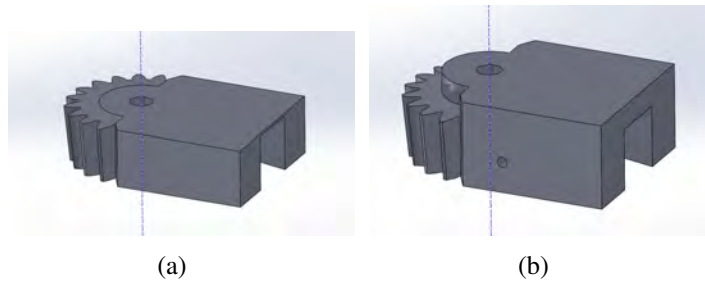


Figure 3.23: 20 tooth sector gear

3.3.6 Taking Control: Addition of Independent Angle of Attack Control

Moving to the next stage of adding angle of attack control adds several issues to overcome. First, something must actuate the wings, two choices are available for the given voltage that a Li-Po battery provides: electromagnetic actuator or servo actuator. Assuming loads on the wings would be large and servos can provide higher forces, they were chosen for actuation. Furthermore, it was assumed that this actuation would be necessary to trim the vehicle to help with any manufacturing inconsistencies. Since the servo only requires power to move and will remain stationary with very little power, it was a reinforced choice to use servos over actuators since actuators draw power at any position other than neutral. Due to the additional weight of the servos, controllers and mechanisms required to add this angle of attack control, it became evident that larger wings and/or higher flapping frequencies would be needed to account for the extra vehicle weight and thus a more powerful motor. The first step was to implement an 8 mm coreless DC motor. The motor has significantly more torque than its 6 mm coreless counterparts at a weight cost of 3 g of extra motor weight. Furthermore, the 8 mm motor required more current to push the higher power increasing battery size. The weight consequences were necessary to even consider creating enough lift for the newly added servos. As a side note, experience was gained with this particular motor in a large four wing flapper that was able to carry itself weighing near 25 g plus another 25 g in payload, compared with other 6 mm motors that were used in 12 g flappers capable of only carrying 6 7 g of payload. While flight characteristics of the two horizontal flappers were different due to size, one cannot overlook the difference in flapper mass going from barely 20 g to over 50 g by increasing a single motor size at a cost of 3

g in the motor alone. Experience has shown that power consumption over 8 watts lends to metal gears. Motors capable of these powers will tend to break thin (< 1 mm thickness) 3D printed plastic gears. Delrin or other injection molded or machined gears must be used to handle the extra power necessary to carry the load. It is also an option to print larger face widths on the gears, though metal gears can be produced with similar masses and much higher reliability if the capability exists.

The CMAVS lab at WSU uses a wire EDM to make its gears. The power upgrade to the 8 mm motor caused many 3D printed gears to strip the gear teeth. The changeover to aluminum gears greatly increased the life and reliability of the mechanism. Figure 3.24 shows the design which includes the larger motor and a two spar wing. The lower spar is used to control the angle of attack. The servos are not included in the models shown in Figures 3.24 and 3.25. These models used fishing line to move the pivot point of the lower spar fore and aft of the vehicle. This design was used on bench testing to test the concept.

While biomechanical control mechanisms are not completely understood, some key features can be seen from observation. First, birds have tails which act in multiple ways, one as a control surface using pressures generated by flow to create moments and two as center of gravity adjustment. Second, dragonflies use their tail to adjust their center of gravity along with phase adjustments in fore-wings and hind-wings. Third, it can be observed that bees have a second set of wings below a main set of wings which may be used for control. This model's control concept most closely mimics that of the bee and similar insects. The mechanism was devised such that a main drive spar controls wing frequency and powers the wings through the stroke. A second spar is added below the main spar which passively follows the main spar but can be offset to the fore or aft of the vehicle so as to increase or decrease the angle of attack of the wings. The second spar provides a similar function as that of the secondary set of wings on the bee. Figure 3.26 shows a schematic of how the mechanism works. The drive angle, ϕ , is assumed to be equal for both the control spar and the main spar through the entire stroke. The input control angle, β , is the angle made by the control mechanism. When there is a control angle, the angle of attack, α , increases or decreases depending on the direction of the stroke and the direction

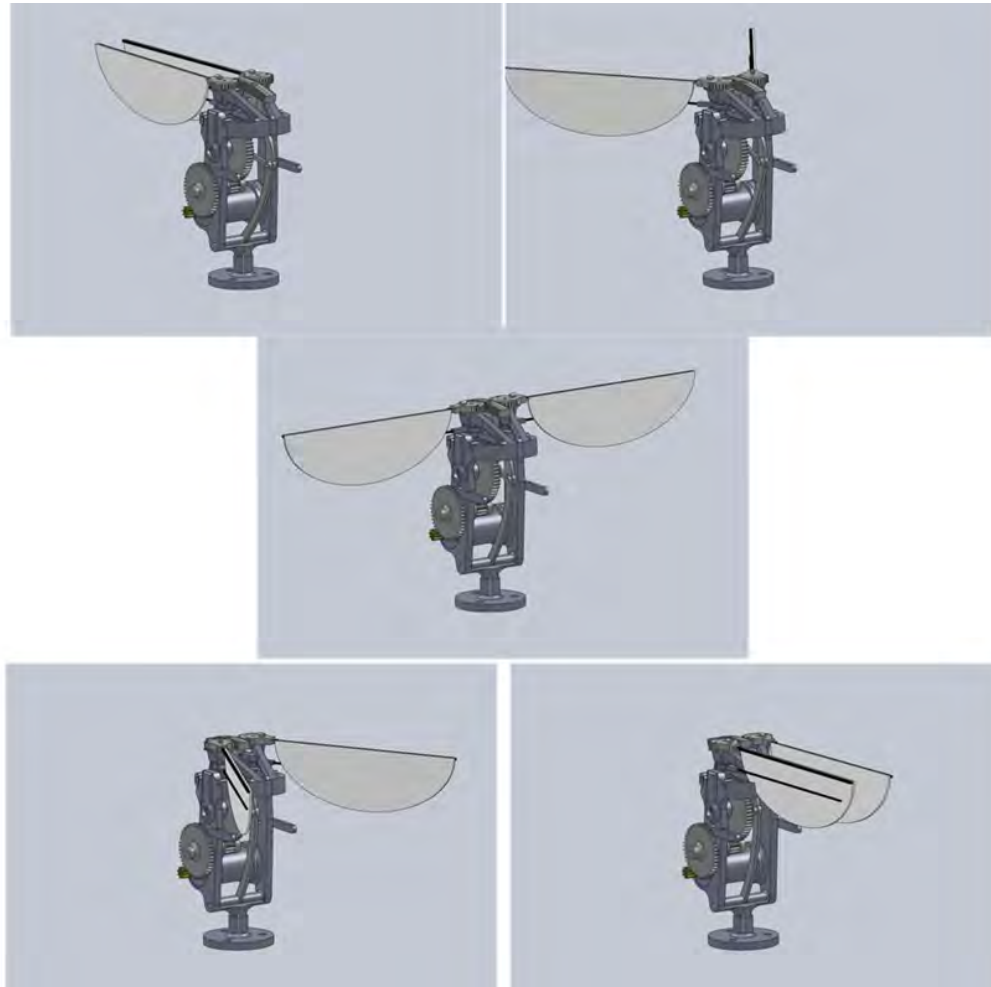


Figure 3.24: CAD Model Demonstrating 180 Degrees of Flapping

of the control angle. Since flexible wings are being used, it is assumed for Figure 3.28 that the wing deflection, α , is 45° with zero control input. Control inputs cause a bias from 45° equal to that made by the geometric angle added by the control spar. Figure 3.27 shows the control mechanism used on the FWMAV. The drive angle, ϕ , varies from -90 to $+90$, a is 3.20 mm, h is 5.57 mm. The control spar is allowed to slide in and out of the bottom spar mount to give the added degree of freedom needed to prevent binding.

Figure 3.27 shows the side view of the FWMAV and the wing angle change caused only by a control input. The control input is applied by moving a lever arm which pulls nylon monofilament tendons through the frame and actuates the control arm forward and backward for the shown wing angle changes. The angle shown is only due to the control

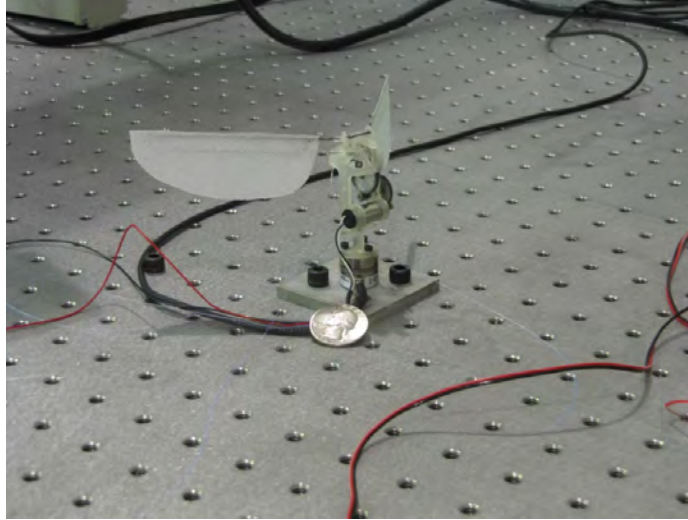


Figure 3.25: Angle of Attack controlled Flapper on a Nano-17 Load Cell

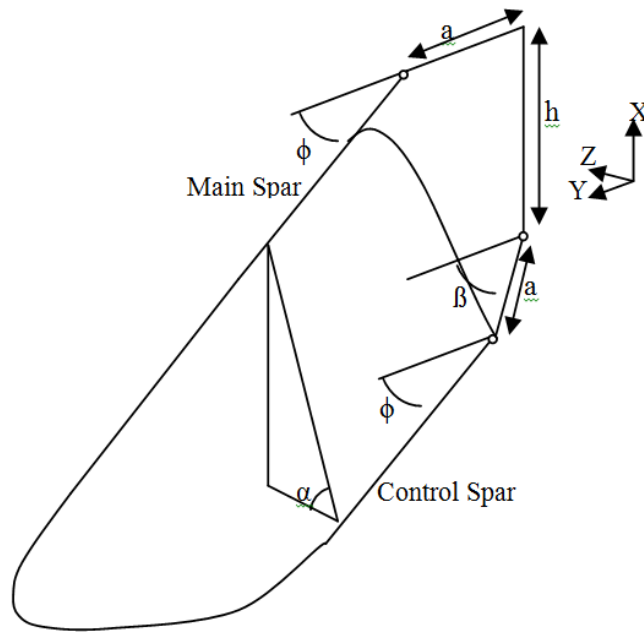


Figure 3.26: Angle of Attack Control Concept

mechanism, this angle is assumed to be added or subtracted to a 45° passively deformed wing.

As the wing moves through a 180° flapping stroke for any given control angle input,

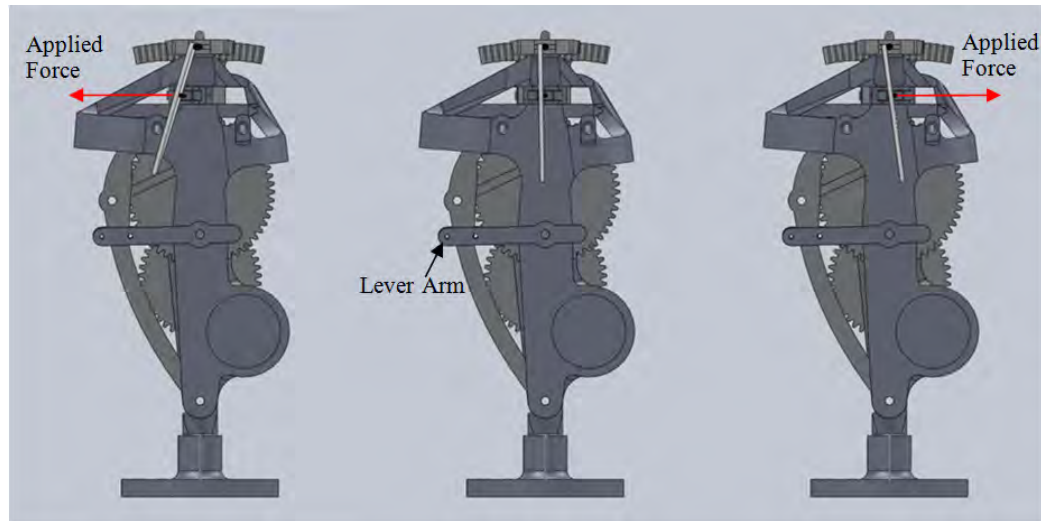


Figure 3.27: Angle of Attack Control CAD

the wing angle of attack will continuously change. The contour plot in Figure 3.28 shows the different wing angle of attacks centered around a base attack angle of 45° . For a forward control input angle of 30° the wing angle of attack varies between 33° and 56° . The color discontinuities represent the instantaneous 90° flip when the wings change direction during the flapping cycle. The red zones in the upper left and right corners represent the same wing position for a continuous cycle. Greater control input angles cause larger fluctuations in the angle of attack throughout the cycle. Notice that the crank angle ranges from 0° to 720° completing two cycles for the given plot.

Subsequent models rotated the control spar around the main spar to create a less binding action through rotation. The CAD and mechanism can be seen in Figures 3.29 and 3.30, respectively. A 2mm printed ball joint was pinned with a 0.5 mm stainless tube to provide sufficient freedom for the secondary spar to rotate. The carbon fiber spar was inserted into the stainless steel tube to and allowed to slide in and out to prevent binding. The printed plastic mount for the ball joint was held in place and moved by a 0.5 mm thick sector gear. The sector gear has an arm that is connected to a servo to provide movement of the sector gear and secondary control spar.

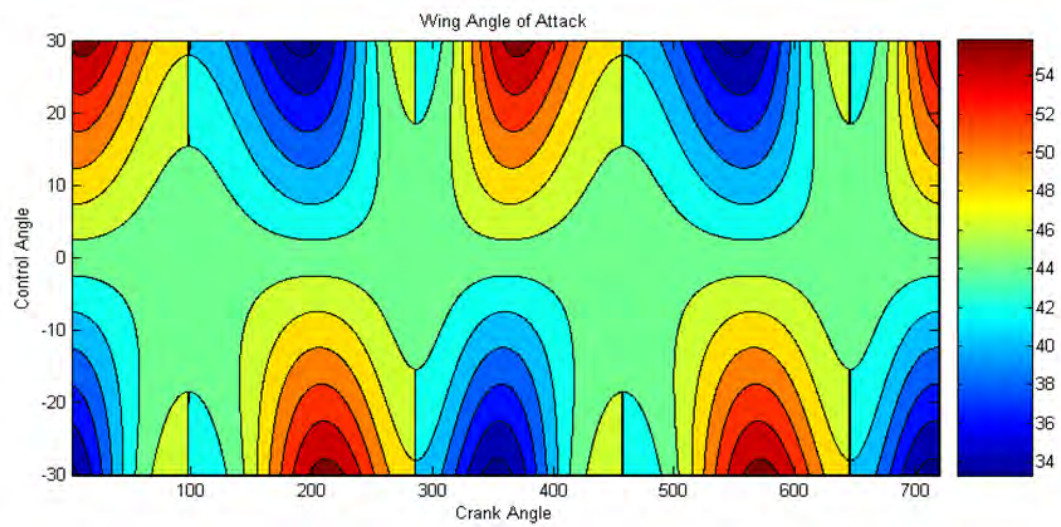


Figure 3.28: Angle of Attack Plotted on Wing Angle vs. Control Angle (Idealized)

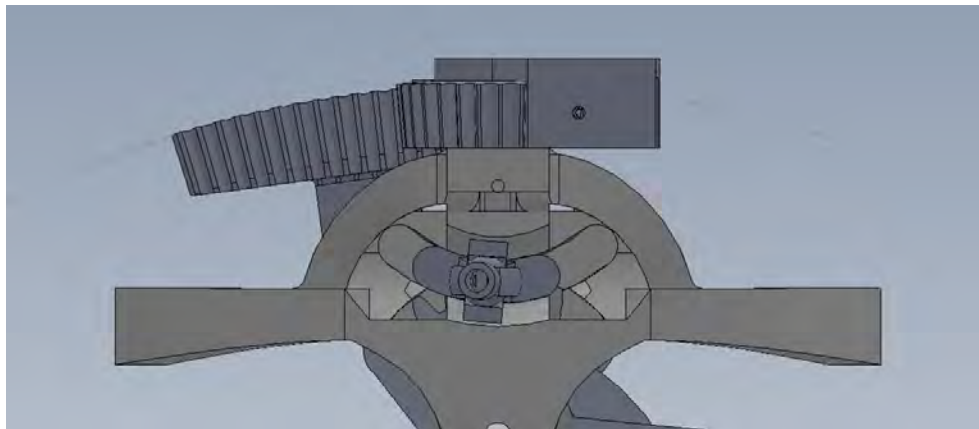


Figure 3.29: CAD of Modified Angle of Attack Control Mechanism

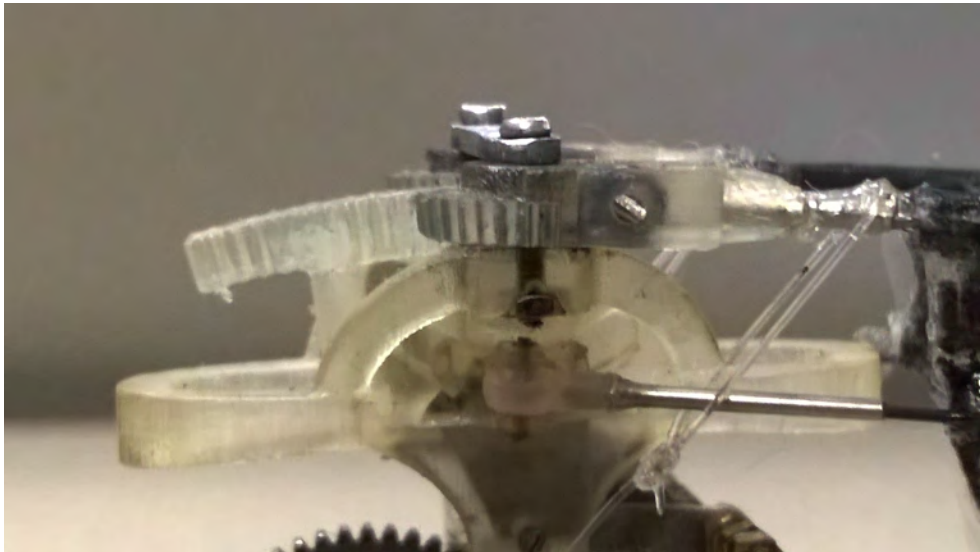


Figure 3.30: Modified Angle of Attack Control Mechanism

Blade Element Simulation

A blade element model was created to gain insight on the aerodynamic forces generated by the prescribed flapping motion. While the model is designed to have a wing-to-wing interaction at the end of each stroke, the simulation assumes an instantaneous wing pitch flip without the clap-and-fling or other wing reversal effects. If the wing kinematics and lift and drag coefficients are correct, the simulation lift profile should match an experimental case near mid-stroke.

This analysis uses a technique based on blade element theory. In the simulation, wings are assumed rigid and their angle of attack is estimated by the amount of deflection an actual flexible wing would exhibit. It is assumed that the wings deflect to an angle of attack of 45° due to the aerodynamic loads at the driving frequency necessary for hovering flight when no controls are input. It is furthermore assumed that any input by the control is a direct correlation with wing angle of attack deviated from the base 45° deflection. With these assumptions, blade element theory can calculate the lift and drag on each wing throughout a flap cycle knowing the area moment of inertia, angular velocity and angle of attack of each wing.

The angle of attack of the wing and blade element theory results in the lift and drag on the wing throughout each wing stroke. With the lift and drag on each wing throughout a full flapping cycle, trim conditions can be devised for a hover condition using cycle averaged forces and moments. The hover condition is defined as adequate lift to maintain a steady altitude, zero forward and lateral velocities, and zero angular velocity about any axis.

From the “Achieving Large Flapping Angles” section, Figure 3.3 is a schematic of the four bar mechanism which drives the wings. The crank, b , has a length of 3.23 mm, connecting arm, c , is 10.05 mm; rocker arm, a , is 25.08 mm; ground link, g , is 24.00 mm. The total rotation of the rocker arm of the described mechanism is 15.79° . The angular velocity of the crank is assumed to be constant through the stroke, thus, setting a flapping frequency can return the angular velocity of the rocker arm. The angular velocity of the rocker arm can be translated to the wings through an additional gear step as it travels throughout the entire cycle. The following method is also further outlined in Doman et

al [62].

Blade element theory uses a coefficient of lift and coefficient of drag to calculate the lift and drag on a wing. In addition to the lift and drag coefficients, the density of the fluid, ρ , area moment of inertia, I_A , and angular velocity, $\dot{\phi}$, are required to calculate lift and drag at any given point in time via Equation 3.1 and Equation 3.2 below.

$$L = \frac{\rho}{2} C_L(\alpha) I_A \dot{\phi}^2 \quad (3.1)$$

$$D = \frac{\rho}{2} C_D(\alpha) I_A \dot{\phi}^2 \quad (3.2)$$

The wing position, ϕ , is defined based upon a constant crank rotation from earlier kinematic calculations. The coefficients are calculated knowing the angle of attack, α , of the wings, which are based upon the control angle β and wing location ϕ for this mechanism. The coefficient of lift and coefficient of drag, determined by Sane and Dickinson, are calculated from Equations 3.3 and 3.4 below which are experimentally determined from mineral bath testing [78].

$$C_L = 0.225 + 1.58 \sin(2.13\alpha - 7.2) \quad (3.3)$$

$$C_D = 1.92 - 1.55 \cos(2.04\alpha - 9.82) \quad (3.4)$$

I_A is the second moment of area of the wing. The prototype model uses a half ellipse as wings. The simulated area moment of inertia was adjusted to mimic the actual wing shape. A half ellipse rotated about the edge has an area moment of inertia as follows in Equation 3.5.

$$I_A = \frac{5}{8} \pi * chord * \frac{span^3}{2} \quad (3.5)$$

Before going further into the simulation of the mechanism, the coordinate system used to describe the vehicle will be discussed. Figure 3.31 shows an isometric view with the coordinate system. The system assumes the vehicle flaps its wings fore and aft of the body. The system is centered at the center of gravity of the vehicle. The x-direction points up through the wings in the lift direction. The z-direction points forward of the vehicle.

The y-direction points down the starboard wing of the vehicle if the wings are spread to the sides of the vehicle. A positive move in the x-direction will cause an increase in altitude. A positive move in the z-direction will cause a move forward and a positive move in the y-direction will cause a sideways move to the right.

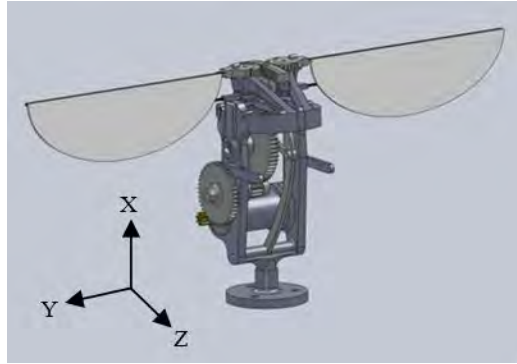
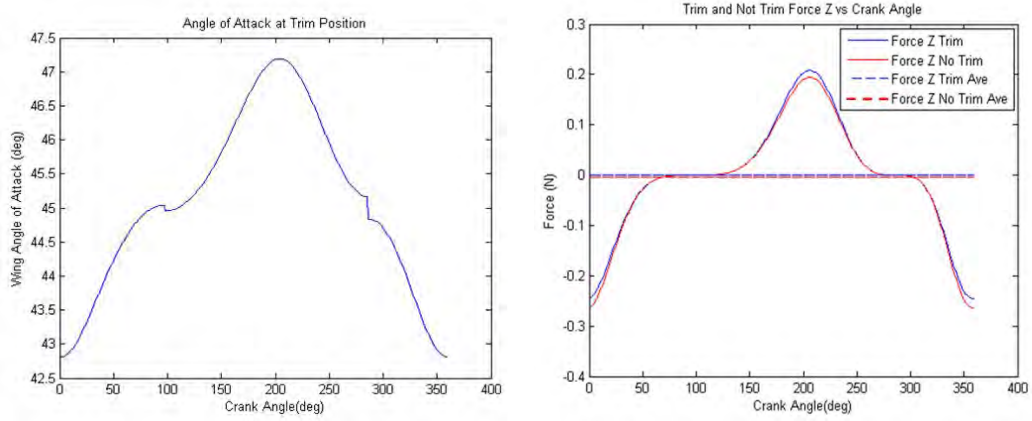


Figure 3.31: Vehicle Coordinate System

A sense of how to trim the vehicle was desired to see how well this method of control could work in simulation. The z-direction was trimmed first to rid the forces caused by the uneven flapping fore and aft caused by the four bar mechanism. The input control angle was -5.4° and caused an angle of attack deviation of $\pm 2^\circ$ throughout the stroke. The angle of attack throughout the stroke at the trim position can be seen in Figure 3.32(a). The change in z-force throughout the cycle can be seen in Figure 3.32(b).

Trim for the $\Delta \bar{M}_y$, or pitch of the vehicle is trimmed by adjusting the center of gravity. This adjustment is not controllable besides on the benchtop via adjusting control board and battery placement. Error in this placement will cause a drift in the z-direction to keep the FWMAV upright. The calculated z position for the center of gravity is -3.1 mm away from the wing roots. The vertical placement of the center of gravity is 24 mm below the wing roots. Lowering the center of gravity increases sensitivity in the pitch direction and decreases sensitivity in the roll direction. By lowering the center of gravity, the z-drift needed to control the vehicle's pitch will be relatively lowered. The trim and untrimmed pitching moment can be found in Figure 3.33.



(a) Angle of Attack at Simulated Trim Condition (b) Simulated Z-Force with and without Trim

Figure 3.32: Simulated Z-Direction Trim Results

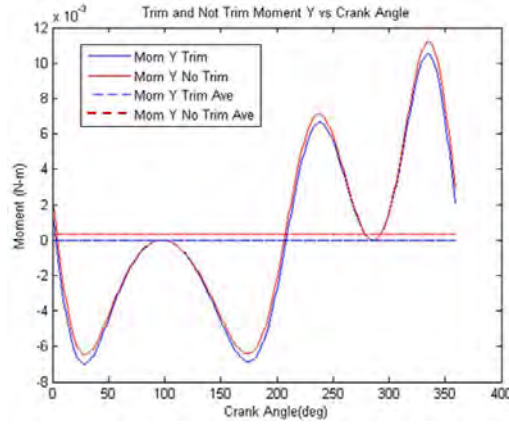


Figure 3.33: Simulated Trim and Non-Trim M_y Moment

A control effectiveness matrix can be found below in Equation 3.6.

$$\begin{bmatrix} \Delta \bar{X} \\ \Delta \bar{Y} \\ \Delta \bar{Z} \\ \Delta \bar{M}_x \\ \Delta \bar{M}_y \\ \Delta \bar{M}_z \end{bmatrix} = 10^{-3} * \begin{bmatrix} 0.1361 & 0.1361 & 32.84 \\ 0.1621 & -0.1621 & 0 \\ -1.5134 & -1.5134 & 0 \\ -0.1167 & 0.1167 & 0 \\ 0.0496 & 0.495 & 0 \\ -0.0022 & 0.0022 & 0 \end{bmatrix} \begin{bmatrix} \delta_{RW} \\ \delta_{LW} \\ \Delta \omega \end{bmatrix} \quad (3.6)$$

The matrix shows the sensitivity of changes in control angle of each wing and frequency changes from the trim point. Due to the assumptions of the simulation, note that changes in frequency or $\Delta \omega$ only change the lift or $\Delta \bar{X}$. Imperfections in wings and mechanism will certainly cause this to vary. Control input in the right wing or δ_{RW} will cause a

lateral movement or a move in the Y-direction. The most responsive or sensitive direction to AOA change is the $\Delta \bar{Z}$ or fore and aft direction. This occurs because a change in AOA causes an increase in z-force for one direction and decrease on the other causing a net positive change throughout the entire wing stroke. For example, an AOA more than 45° on a backward stroke will cause more drag and a forward movement. On the forward stroke, the AOA will be less than 45° causing less drag than at 45° so the vehicle will have a lessened restoring drag force. This can also be found in the moments, The M_x sensitivity is more than twice as large as any other. Although the pitch is linked to the Z force, note that the M_z sensitivity is lower than the pitch authority by 15 times. This means that the roll control of the vehicle is very little compared with all other degrees of freedom. Adding another means of control will aid in decoupling the 6 degree of freedom control.

3.3.7 Taking Control: Addition of Roll Control

From simulated results it was found that significant lack of control authority in the M_z , roll direction, was available using AOA control schemes. M_y , pitch control, is coupled with Z-direction movement but can be minimized by adjusting the center of gravity of the model. Furthermore, due to the limited amount of control in the roll direction, any inconsistency in the wings would most likely be difficult to impossible to correct without some sort of active control. It is also apparent during high frequency flapping that the wings bend upward causing the largest thrust vector to move away from the vehicle, essentially reducing the lift by changing its vector. Figure 3.34 illustrates the loss of vertical lift due to wing deflection in the vertical direction. The new lift will be reduced according to Equation 3.7 below.

$$Lift' = Lift * \cos(\gamma) \quad (3.7)$$

It is thought that if the wings could be held down so as to maintain a γ of $< 5^\circ$ under all wing loads that more effective lift could be produced at higher frequencies. While it is possible to stiffen the leading edge more for a means of the same result, small additions of weight to the wings can be detrimental to power required. Using the theory to tie the wings

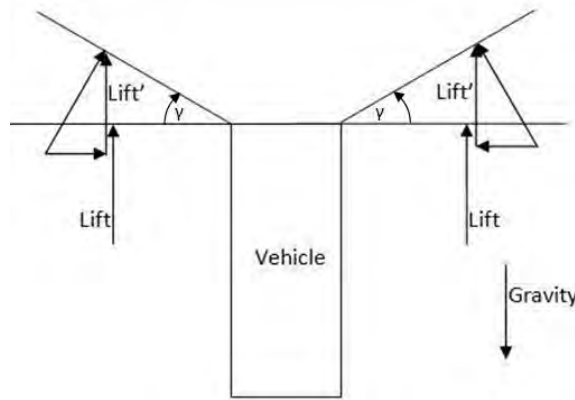


Figure 3.34: Wing Lift Reduction due to Wing Bending

down presented a means of adjusting the angle of the wing as it flaps. Forces needed to hold an individual wing down and manipulate it seemed to large for the small servos that are available to use on this weight vehicle, however, the servo did have enough force to bias the two wings if they are coupled together. The resulting mechanism is in Figure 3.35. Each piece of nylon monofilament is connected to a wing, routed through tubing in the

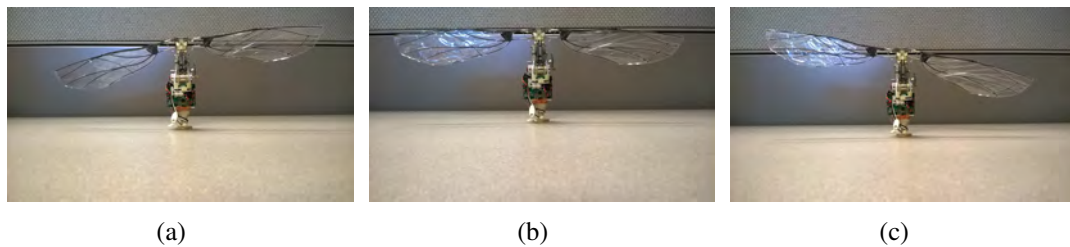


Figure 3.35: Roll Control Model

frame and connected to a the servo. Figure 3.36 shows a close up of the servo and nylon monofilament. Furthermore, adjustment for uneven mono-filament lengths could be made using the aluminum adjusters seen in Figure 3.37. These adjustments are made similar to that of a bicycle brake or shift cable.

Another modification made to the vehicle is the extra degree of rotation at the wing roots. This hinge allows the controls to move the wings. To avoid slow or stopped wings from drooping, a spring was added to keep the nylon monofilament in tension at all times.

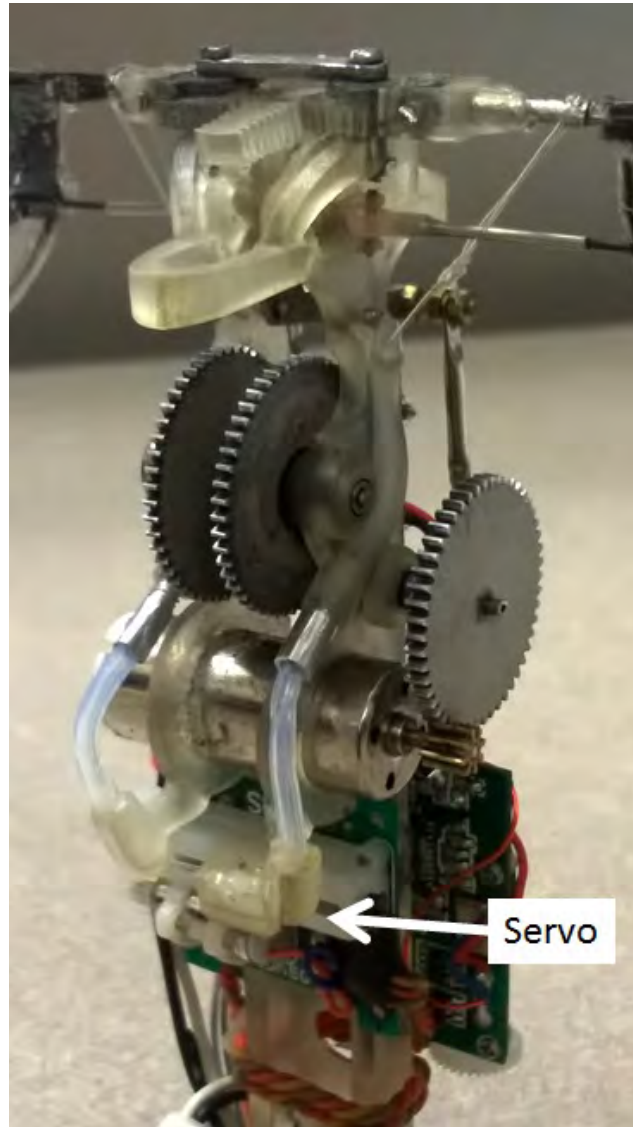


Figure 3.36: Roll Control Servo

The rotating the wings provides a moment about the center of gravity of the vehicle. The placement of the center of gravity relative to the center of pressure on the wings determines the sensitivity of the mechanism to roll and pitch. Moving the center of gravity further away from the center of pressure will cause a less sensitive, and provide less authority to the controls.

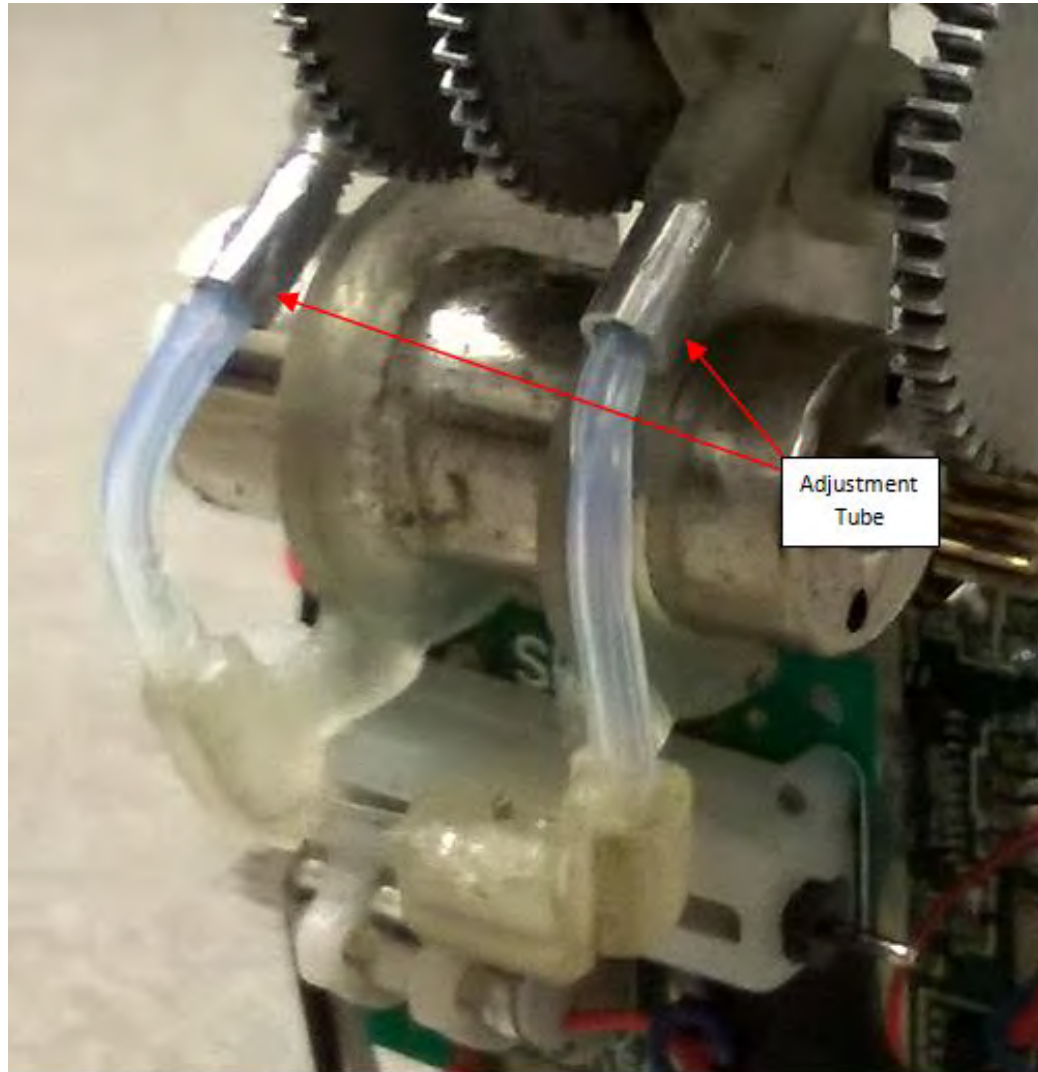


Figure 3.37: Roll Control Trim Adjustment

3.3.8 Collaboration with AFRL: Combining Novel Drive Mechanism with Split Cycle Control Scheme

AFRL/RQQA has a group of researchers working on MAVs. The major difference being that the group concentrated on controlling the MAV using only two motors. The two motors, one for each wing, are commutated and controlled by a control which receives position feedback from motor encoders. Each motor is capable of providing split-cycle control to their respective wings allowing the wings to be moved faster on the 1st half cycle vs. the 2nd half and vice versa. The methodology has even been advanced to quarter-cycle con-

trol in attempt to provide a more decoupled control algorithm. The promising lift results demonstrated with the 180° flapping angle prompted a design overhaul to implement the two motor design. The 8 mm diameter brushed motor was switched to two 13 mm diameter brushless motors. The brushless motors while lighter, provided more torque and efficiency. The brushless motors are capable of handling a 2 cell voltage input versus the single cell voltage input allowed by the 8 mm motor. The increase in voltage more than doubled the power output. Furthermore, an extra motor was added doubling the power to the wings. The removal of servo actuators lessened the weight of the vehicle and a more simple frame design allowed for manufacture of aluminum vs. 3D printed plastic. Due to the extra power, the sector bevel gear set was adjusted to handle the larger torques. First the gear teeth were made larger for better engagement in plastic. Shortly after followed aluminum bevel gears custom made on the wire EDM. Figure 3.38 shows one half of the FWMAV. The three holes in the left side of the frame are used to mate a replica on the other side. Flight weight models trim the excess screws and even lighten the bevel gears by drilling holes where excess material is not needed. Total vehicle weight including the battery and control board weighs 31 gf.

3.4 Summary

The goal of designing and manufacturing a flight weight model capable of flapping with an amplitude of 180 deg with relatively symmetric flapping has been achieved. Lift ratios are generally greater than one for many wing-sets, however a need for stable and repeatable wings are desired. Chapter 4 discusses the wing design inspiration from nature and the methodology used to generate the wing layout and build the wings.



Figure 3.38: Two Motor Design with Full Aluminum Chassis and Gears [79]

WING DEVELOPMENT

Flapping Wing Micro Air Vehicles are very sensitive to wing performance relative to mass, size, stiffness and frequency. While the mass, size and stiffness are obviously linked to one another, how these interact due to aerodynamic and inertial loads impact the vehicle and performance greatly. The design envelop to date for payload remains low offering little in the way of wing robustness. Wings truly have to be designed specifically for a maximum lift capacity and good efficiency. In the attempt to find a reasonable wing capable of handling the large deflections and high loading as well as good fatigue strength, several wing materials were investigated. Early wing versions were made of thin foam glued to carbon fiber rods. Ease of manufacture, low weight and good flexibility provided a good baseline for wing sizing and preliminary lift capabilities, however due to the low fatigue strength of the foam the wings would break down after a few tests changing performance. To date the best solution for wings are custom, hand layup wings made using carbon fiber tow, epoxy, silicone molds and cured carbon fiber rod.

4.1 Learning From Nature

Many biologists have worked to classify insect wings. For butterflies alone there are at least four systems, namely: Herrich-Schäffer, the “Indian” system, the Rothschild-Jordan system and the “English” or numerical system [53]. The Comstock-Needham system, created by John Comstock and George Needham in 1898, is based upon venation of all insects and has a fairly universal application [53]. Figure 4.1 shows a picture of the classification system. This system represents six types of veins in wings: the Costa, Subcosta, Radius,

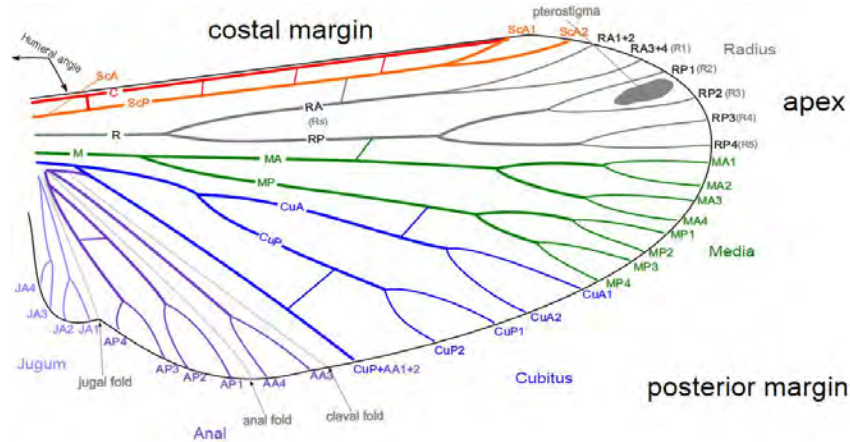


Figure 4.1: Comstock-Needham System [80]

Media, Cubitus, and Anal Vein. The Costa is the leading edge of the wing. The Subcosta is below the Costa that reaches the wing's span-wise edge. The Radius is the third longitudinal vein that typically contains one to five branches. The Media contains one to four branches and also reaches the trailing edge. The fifth longitudinal vein is the Cubitus. It typically has one to three branched veins that reach the wing margin. Finally, the Anal Veins are always un-branched and behind the Cubitus [81]. Due to the incremental sizes of carbon fiber (veins) that are available for manufacture, not every feature described in the system exists in the produced wings.

With the features of the system in mind, three specific insect wings were inspected for inspiration. While some of the commonalities described in this section can be found across a much broader scope of insects, three different insect wings were selected and carefully observed; the *Bombus Hymenoptera* (bumblebee), the *Tibicen pruinosus* (cicada), and the *Sphex argentatus* (wasp). At first glance these wings appear to be unrelated in shape, size, and vein structure, but a closer look into Figure 4.2 reveals a similar venial pattern is found in each wing. With each wing separated into four regions, similarities can be found. Region I reveals larger and stronger veins connected to a single point on the body of the insect. These larger veins will be called the wing root. In each case, the upper root vein propagates span-wise forming the wing leading edge while the second vein angles downward giving strength in the chord-wise direction. The cicada has 5 veins

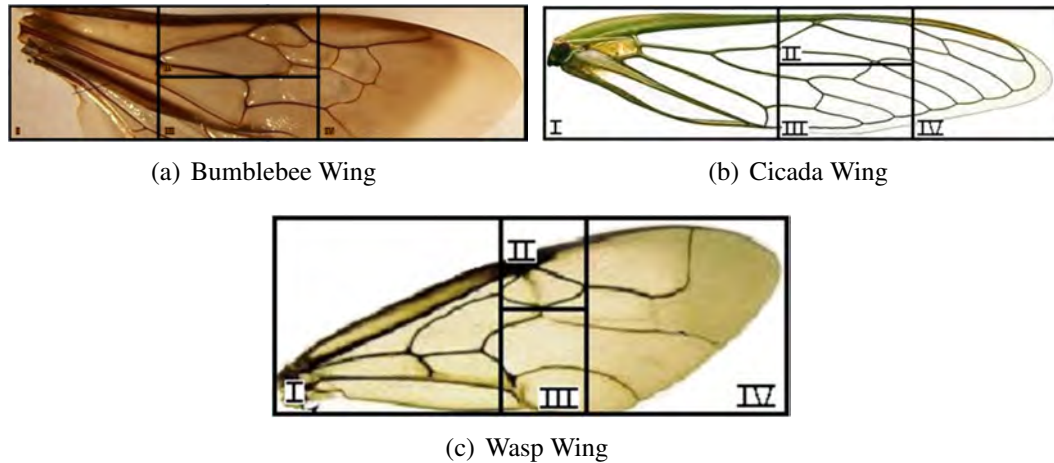


Figure 4.2: Insect Wing Division

that lead into the wing from the root, the wasp contains 4, and the bumblebee contains 3. Moving on to Region II, the most prevalent commonality found in all observed cases is the distinct connection point between the Subcosta and the Costa at mid wing-span. At the connection point, there is an abrupt transition between the thick wing root and thin wing tip. The Costa and Subcosta are apparent in Region I. The handling and manipulation of these wings reveals the wing root is dramatically stiffer than the tip. Region III is the beginning of the soft and uniformly skinned region of the wing which is likely generating the majority of the aerodynamic loading due to its large area and higher velocities as a result of being more outboard of the wing root. The trend in region IV was used for wing design given that the veins were unconnected, relatively soft compared to the root, and a larger surface area. Region IV has a tendency to have a lower AOA most likely due to generate a higher $\frac{Lift}{Drag}$. This design can be found in propeller blades as the angle of attack reduces toward the tip. Observing each flapping wing in high-speed video during flight provided evidence that the semi-parallel nature of the veins found in Region I allow each wing to twist near the wing root. This twist, in addition to more flexibility towards the wing tip, gives the wings the propeller type twist. Some conclusions are made about each region below:

1. Region I is the load bearing region. This region carries the load in the vertical and torsion degrees of freedom. This is the most rigid and dense region of the wing and typically contains straight non-branched veins.

2. Region II is a subset of region 1. It is here that the strongest part of the Costa tapers off to the tip of the wing. This region contains the structural hub of the wing called the Nodus. Much of the wing venation meets in this small region.
3. Region III contains the structural area of the wing which defines the primary and secondary lifting regions. The layout of the veins in this region allow for stiffing and softening of the torsional rigidity of the wing. Region III gives, 'initial conditions' for bending to region IV. For example, if region III is too soft, region IV will have very little angle of attack and does not add additional lift to the flapping cycle.
4. Region 4 is the most critical due to the moment arm it has on the root. This region requires stiffness sufficient to maintain an angle of attack but a mass low enough to minimize a mass moment arm. Furthermore a wing which is too resistant to twist (stiff) causes significant drag forces in the flapping direction which are adverse to flapping efficiency and causes large stresses on the flapping mechanism.

4.2 Coalesced Wing Design

The wing design shown in Figure 4.3 was prepared to test the effects of the structural layout of the veins based on observations of natural flying insects. Adjusting the angle of attack at a given The dimension d1 will remain fixed due to previous interpretations that this distance on insect wings is roughly half the distance of the length of the wing. The dimension d2 will be fixed at 6.61mm to reduce the number of variables for testing. The distances of spars-A and B from the wing root are believed to control the location and magnitude of wing twist. The purpose of testing these parameters is to show that as the dimensions d3 and d4 become smaller, the amount of twisting will increase. Spar-B is believed to control the twisting at the tip while spar-A dictates root twist.

It is believed moving veins A and B closer towards the wing root will cause more wing twist. A greater wing twist will create less drag forces and allow for a higher flapping frequency. A higher flapping frequency will then cause greater lift forces and a more efficient load on the driving motor. At some point, the flapping frequency will continue to increase,

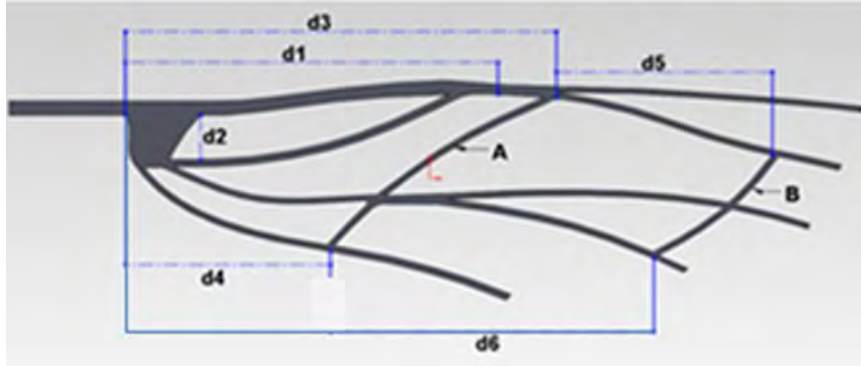


Figure 4.3: Coalesced Wing Design [66]

but lift will remain the same or reduce. At this point, the wing is saturated. It is desirable to create a wing with a predictable lift saturation point so wings can be sized according to the vehicle weight. Given the time consuming reality of creating each set of wings, it is not feasible to create enough sets to show the saturation point of the designed wing at this point in time. It will be shown, however, the movement of spars A and B do cause more wing twist, a higher flapping frequency, and more vehicle lift.

4.3 Wing Design and Manufacture

As it is known that FWMAV wings require large deflections and high loading relative to wing weight, a light-weight, high-strength material is necessary. Continuous carbon fiber is one place to find such attributes. The complex venial geometries found in natural wings are difficult and sometimes nearly impossible to mimic using pre-manufactured straight carbon fiber rods. Consequently, it was necessary to create each wing using individual groupings of carbon fiber tow. The materials used for the wings are carbon fiber tow, epoxy resin, epoxy resin hardener, and silicone molds. Each wing design is first defined in a CAD program outlining the discussed simplified venial structure. Through the use of a 3D prototyping machine, each design is made into a positive mold. This process involves creating the outline of the wing with venial thickness of roughly 0.8 mm. This thickness will suffice for up to 3k carbon fiber tow. Widths and depths can be adjusted to provide more strength in either the vertical or lateral directions respectively. As the thickness of the

tow increases, the thickness in the structure should also increase. The design is placed on a 1.5 mm thick base with lining edges of 2-3 mm. These parameters are subject to change based on the size and thickness wing that is desired, for this size wing it was a good mix of part stability and material conservation. Silicon is then poured into each mold to create a negative of the wing structure. It is important to provide as flat a surface on the backside of the silicone as possible as this can adjust the flatness of the wing. Carbon tow was then impregnated (painted) with resin and laid into the grooves of the silicone mold as seen in Figure 4.4(a). Cutting and trimming of the tow was done as it was laid into the mold. After several iterations of making the wings it became apparent that the order in which the tow is laid makes a difference in the wing. Essentially a weave can be made so as to make joints more robust. In some cases, the order of the tow placement can be the difference between a good and bad wing. Be sure to look for a long workable time on the epoxy as a single set of wings can take upwards of one hour to layup, especially if being done for the first time. Place the silicone mold and carbon fiber layup on a flat structural piece of aluminum or steel as seen in Figure 4.4(b) to maintain flatness during the vacuum and cure cycle. A release fabric is put down directly on top of the epoxy and tow followed by a cotton pad to soak up any excess epoxy as seen in Figure 4.4(c) Cure times for an vacuum bagged, baked set of wings was around three hours depending upon the epoxy and hardener chosen.



Figure 4.4: Wing Layup and Cure

4.4 Sizing and Stiffness Considerations

The size, stiffness and mass moment of the wing will determine its lifting capacity. While all three of these parameters are linked, they are not entirely dependent. Changes in the wing can be as sensitive as trimming off a few millimeters for better performance. Depending upon the robustness of a mechanism, it may be advantageous to begin with a “weak” and or small wing. It is better to err on the small and light side to maintain the mechanism than install a heavy stiff wing-set which breaks the mechanism before learning anything about the mechanism or wing design. Saturating a light but strong set of wings can show where the weakest points in the wing are and where they may need strengthened. Furthermore, high speed imagery can investigate how the wing transitions, how well the AOA changes along the span of the wing and if the wing is having any poor interactions

with the mechanism. Many wings were built that would lose angular velocity near the mid-stroke. This was an indication of too slow of flapping or too large/stiff of a wing. A good wing/mechanism couple will look just as fluid as the high speed videos of insects. One set of wings tested appeared to be becoming saturated, the wing had a span of 9.7 cm and an area of 18 cm² and was able to lift 25.6 g at 22 Hz. Another set of wings, with the same spacial layout but wider having a span of 10.5 cm and an area of 21.2 cm² was capable of lifting 35.2 g at 20.7 Hz. Both wings were made using the same materials, with the same people manufacturing and testing, with the same testing methods and the latter achieved a 34% increase in lift at maximum power of the mechanism. Another example, two sets of wings having a span of 10.5 cm and an area of 22.0 cm² lifted 38.4 g on a lever balance at 19.0 Hz and 20.8 Hz. Other wings of comparable size, with the same drive mechanism were only capable of lifting 25 g before the motor was not able to flap them faster. Refer to Chapter 5 for more comprehensive findings. The intention of these findings is to provide a starting point for a wing design in the 20 to 30 g vehicle weight regime.

4.5 Summary

This chapter discusses a wing venation layout inspired by nature. Three insects wings, namely a wasp, bumblebee and cicada, were compared for similarities. The most notable similarity is the truss-like structure that spans from the root to the mid-span of the leading edge. Using the similarities found in the insect wings, a venation layout was drawn in CAD to provide a repeatable layout that could be quantitatively adjusted. The CAD layout was 3D printed to provide a repeatable mold design for the carbon fiber layout. Fiber layout must be recorded as subtle changes can make large differences in wing performance. Wing manufacture methodology is discussed along with preliminary lift results demonstrating the high sensitivity to the venation layout and fiber placement. Chapter 5 will provide greater detail on lift testing and PIV flow measurements that further investigate the lift mechanisms that are advantageous to flapping wing flight.

EXPERIMENTAL TESTING

5.1 Introduction

Experimental testing is the best means of evaluating a design. From flight testing to bench testing to component testing, many times as a researcher the most necessary lessons are learned from these activities. Many tests have been run over the years, from testing functionality to flight attempts. After few attempts for flight and subsequent failures leading to complete mechanism destruction, the necessity of bench testing became apparent.

Several means of achieving data are applicable to MAVs. One of the easiest means to acquire qualitative and quantitative data is via high speed video capture. This allows the researcher to change the blur of wings or even mechanisms to speeds of more than 60 times slower than real time. Some high speed cameras will require ample lighting due to the reduction in exposure time. One of the most useful pieces of quantitative information that can be gained from high speed video is the flapping frequency of the vehicle. Other useful qualitative items that can be viewed are stability of the mechanical parts and wing deformations. Additionally load cells and PIV testing can provide valuable data for analysis validation, documentation and evaluation of a design or component. A more simple design, a lever balance, has been used to measure lift for many tests. While the exact lift cannot be digitally recorded, lift thresholds are achievable at an incremental level. This method is cheap, easy to use and requires no data processing or concerns of data accuracy. The lever balance also provides a large mass to dampen the wing oscillations of the FWMAV.

5.2 Load Cell Testing

ATI Industrial Automation sells a load cell that is 17 mm in diameter. This load cell is capable of reading 6 degree of freedom forces and moments. The resolution of the forces is as low as 1/160 N (0.68 gf) and has a maximum input force in any direction of 12 N (1223 gf). Torque in any axis is limited to 120 N-mm and has a resolution of 1/32 N-mm. The sensor uses three M2 tapped holes for mounting on both sides. Typically the mounting holes were designed into the frame of the vehicle for ease of testing. This hole pattern was standardized for use in our lab for testing on both the lever balance and PIV setup as well. Units can be purchased with or without a data acquisition system (DAQ) depending upon the lab capabilities. If a larger load is required, a nano-25 is capable of 125 N in the x and y directions and 500 N in the z-direction (normal to the top surface.) Resolutions will drop to 1/48 N in the x and y directions and 1/16 N in the z-direction.

5.2.1 Experimental Setup

The normal direction or z-direction of the load cell is what is considered the x direction of the vehicle in the setup seen in Figure 3.25. A base plate was made to fix the load cell to an optical table. The plate consists of four holes on one inch square centers with the 2 mm load cell mounting pattern drilled and countersunk for flat mounting to the table. Experimental results will be reflected using the vehicle coordinate system. Load cell testing was performed with an ATI Nano-17 6-axis load cell and a lever balance. The maximum sampling frequency for the included DAQ is 7000 Hz which in turn provides 700 samples per flapping cycle at 10 Hz and 350 samplers per flapping cycle at 20 Hz. Filtering is done in the DAQ prior to data saving. These parameters are available to adjust in the DAQ software.

Level Balance Verification

Load cell data taken with a Labview data acquisition system proved to be very noisy. Although the mean of the data seemed reasonable, some verification was desired to validate the results. Validation was performed using a lever balance to measure lift. While the other

five degrees of freedom could not be quantified, it was still desired to determine how accurate the load cell results were in the lift direction. The lever balance was attached to an optical table to provide a rigid base. The balance used ball bearings to create a low friction rotation about the base. To begin testing the vehicle and all necessary testing equipment, whether batteries or power supply wires, were connected to the balance. After installation the lever was balanced using an adjustable counterweight to remove all effective weight of the vehicle. Items were then hung directly underneath of the vehicle from a string. The items were either calibrated masses or measured using a calibrated scale to resolve better than 0.1 g. The vehicle was then powered and flapped to lift the masses. While lifting the mass, high speed imagery was captured to calculate the frequency. Regardless of the frequency, this is a reasonable means of determining the lift capability of a mechanism and wing set. Although control will lessen the lift capability of the vehicle, achieving a lift to weight ratio greater than one is a good starting point for a design.

High Speed Imagery

High speed cameras come in many levels of quality and cost. A hand held digital camera capable of recording video at 600 frames per second (fps) will provide sufficient frame rates to capture flapping frequencies of 30 Hz. This style camera is relatively inexpensive and easy to use. Other systems can cost over one hundred thousand dollars for three camera systems. A Photron FASTCAM MC2 system was used to capture many of the high speed imagery used in this research. The system is capable of recording 2,000 fps and can store 4 GB of data, which allows 4 cameras 4 seconds of data at 2,000 fps with a 512x512 pixel resolution. Pictures are gray-scale and provide wonderful playback of 10-30 Hz flapping wings.

Power Measurement

Power consumption is a very important part of the vehicle testing. Initially, these concerns are for determining the ability of a flight weight power source having the capability of supplying sufficient power to fly the vehicle. Subsequent to defeating the task of flight is duration. Finding an efficient power and drive system is critical for a flight duration of

any length. Choosing a larger battery may not mean a longer flight time. The larger mass can cause the motor or wings to run less efficient, draining current so much faster than the previous flight weights that the flight time can be reduced while compromising motor, mechanism and wing integrity.

Initially, lift tests were done using power supplies. Several tests were done using set voltages and allowing current draw to be unlimited to the motor. Power supply displays can give an indication of current draw. This can be useful for deciding on battery size and capabilities for DC brushed motors. Brushless motors are distinctly more difficult as they require a speed controller for commutating the coils of the motor. One method of determining flight worthy lift is to utilize the flight weight power supply (battery) and controller when performing lift tests. Furthermore, if using a power supply to power the speed controller, the voltage can be adjusted to throttle power to the motor up or down. Battery voltages vary up to one volt per cell as they discharge, changing the supply voltage can demonstrate the battery level required to lift the vehicle.

5.2.2 Experimental Results

The first load cell tests performed were on the foam winged AOA adjustable flapping vehicle. Figure 5.1(a) shows the filtered data from the ATI DAQ. This data was then further filtered using the method devised by Jeng et al [82]. Figure 5.1(b) shows a comparison of the lift force between the simulation and experiment running at the 12.55 Hz. The two peaks within each cycle represent the wing near the mid-stroke where aerodynamic lift is highest. In this plot, to facilitate a comparison, the simulated lift has been purposely re-scaled to the maximum value of experimental lift force. The simulation makes use of the correlation of Sane and Dickinson, Equations 3.3 and 3.4, for the lift and drag coefficients but the current experiments were conducted for a different set of wings than those used in the Sane and Dickinson experiments. Hence, it is assumed that only the magnitude of the predicted force would be affected. Moreover, in the experiments, the wing-to-wing interaction and wing reversal effects occur at two ends of the stroke motion. By matching the maximum lift force, it is assumed that the trend near in the middle of the stroke motion

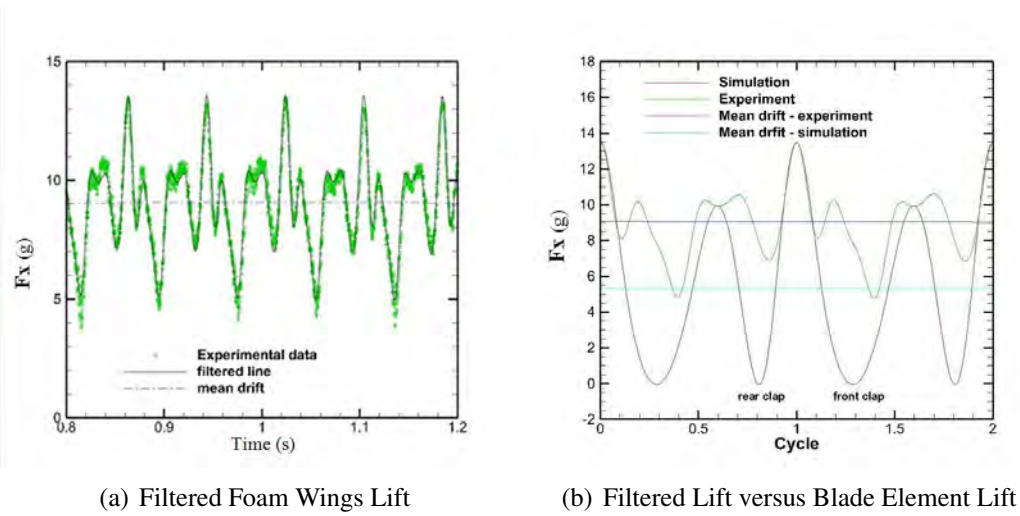


Figure 5.1: AOA Adjustment Vehicle Load Cell Results

(where the maximum peaks occur) is unaffected by the wing interactions and reversal effects occurring at both ends of the stroke. As seen from Figure 5.1(b), the simulation gives zero lift at the two ends of the strokes because the angular velocity is zero while the actual measurement exhibits a positive lift due to the wing interaction and wing reversal effects. Since this effect was neglected in simulation, the approximate increase in cycle average lift can be determined by determining the difference between the simulated and actual average lift results. Each peak occurs when the wing is at its maximum velocity, midway through a stroke. The supination causes a higher peak lift shown at both ends of Figure 5.1(b), while the pronation produces a slightly smaller peak lift. This difference is caused by the uneven angular peak velocity between forward and backward sweeps. The wing interaction and reversal effects generate a 67% increase in mean lift force.

Control results based upon the simulation are presented next. The controls were set fore or aft to their fullest extents of $\pm 15^\circ$ for testing at the controlled angles. The first series of control tests were conducted at 2 volts. The prototype operates at about 9 Hz when 2 V is applied to the motor. Maximum control deflections were used in each case to show the maximum effect. For both control arms in the negative z-direction, each wing will experience less drag on the forward stroke and more drag on the reverse stroke. This results in a forward vehicle force. Similarly, for both control arms actuated in the forward z-direction, each wing will experience more drag in the forward stroke and less in the reverse

stroke. This would result in a negative z-direction translation of the vehicle. Next each control arm is centered for no control input. Simulation results suggest that the vehicle should tend toward a forward translation with no control input. Finally, the moments about the x-axis for each symmetrical control setting are near zero. From Tables 5.1 and 5.2 the lift (x-direction) and fore/aft (z-direction) are behaving as desired. With a control input, the lift drops as expected. For the fore/aft motion, the two volt case shows good trim and authority in the fore/aft with negative and positive control input respectively. The three volt case becomes out of trim at 0.28 g, however the differential is still in the correct direction and of similar magnitude to the two volt case.

Table 5.1: 2 Volt Symmetric Control

	Both Negative	Both Center	Both Positive
Frequency	9.10	9.11	9.36
Fx (gf)	3.8	4.2	3.3
Fy (gf)	-0.41	-0.02	-0.22
Fz (gf)	0.27	-0.01	-0.13
Mx (N-m)	-0.00012	-0.00004	-0.00003
My (N-m)	0.00046	0.00027	0.00003
Mz (N-m)	0.00006	0.00000	0.00013

Table 5.2: 3 Volt Symmetric Control

	Both Negative	Both Center	Both Positive
Frequency	12.66	13.77	13.16
Fx (gf)	9.0	10.5	9.1
Fy (gf)	-0.69	-0.45	-0.29
Fz (gf)	0.50	0.28	0.08
Mx (N-m)	-0.00010	0.00043	-0.00004
My (N-m)	0.00073	0.00010	0.00031
Mz (N-m)	0.00049	0.00084	0.00064

The assumption made for simulation testing was each wing deforms to 45° instantaneously for each wing stroke. Then the control adjustments make slight variations to this base angle. In the two volt experiment, however, the wings are deforming less than 45° from vertical for each stroke. This should only have an effect on the magnitude of lift

produced by each wing by placing emphasis on the drag forces. Drag forces are increased because the angle of attack is increased. Figure 5.2 shows the actual wing deflection with a 3 volt motor input which are near 45° .

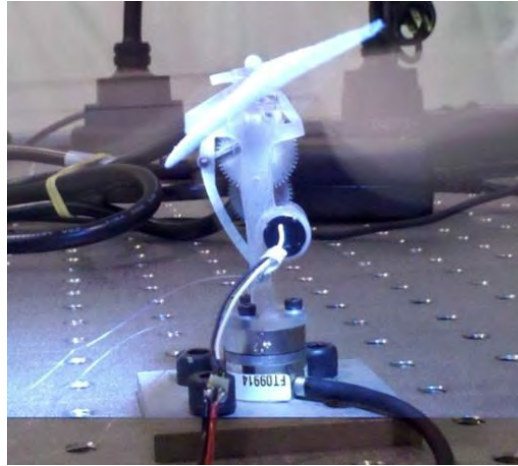


Figure 5.2: Strobe Light Foam Wing at 3V

To generate the experimental control matrix, five tests were run for each voltage supplied. Table 5.3 shows the bare results for the experiment for left wing full control fore and aft, both wings centered and right wing full control fore and aft. Forces are in gf and moments are in N-m. The units chosen are gf so as to be easily compared to the vehicle mass. Moments are in N-m to maintain continuity with the simulation results. Forces are converted to N/deg for the control effectiveness matrix to maintain units as well as moments to Nm/deg. The deg stands for the degrees of control input to the mechanism for the respective wing side, left or right. The control effectiveness matrices are not intended to be identical because experimental results utilize full control extents while simulation are based off of the trim point. However, due to the relatively linear nature of the control plots from the simulation, the direction and magnitudes should be similar.

Due to the use of foam wings and the need for several tests, breakdown of the wings has skewed the results. As seen in the symmetric control cases, the lift is largest at the center position. During this phase of testing the lift was greater at every point but one other

Table 5.3: 2V Load Cell Results: Individually Controlled Wing					
2 Volt	Left Wing			Right Wing	
Control Position	-15	15	0	-15	15
Fx	4.2253	4.5357	3.7242	4.5534	4.4648
Fy	-0.39876	-0.67566	-0.42187	-0.27968	-0.19078
Fz	0.043873	-0.11182	0.32219	0.17567	0.13566
Mx	-0.00003	-0.00013	0.00002	-0.00012	0.00001
My	-0.00020	-0.00010	-0.00039	-0.00034	-0.00016
Mz	-0.00001	-0.00022	-0.00006	-0.00004	0.00005

Table 5.4: 3V Load Cell Results					
3 Volt	Left Wing			Right Wing	
Control Position	-15	15	0	-15	15
Fx	5.8705	11.5710	10.8610	11.7710	12.0510
Fy	0.0716	-0.8290	-0.2882	-0.1595	-0.4371
Fz	0.0425	0.2236	0.5325	0.5536	0.1773
Mx	-0.0001	0.0000	-0.0001	-0.0003	-0.0002
My	-0.0005	-0.0004	-0.0008	-0.0009	-0.0005
Mz	-0.0001	-0.0004	-0.0001	-0.0001	-0.0001

than the center position, indicating that the wings are not as stiff and thus are not producing as much lift.

$$\begin{bmatrix} \Delta \bar{X} \\ \Delta \bar{Y} \\ \Delta \bar{Z} \\ \Delta \bar{M}_x \\ \Delta \bar{M}_y \\ \Delta \bar{M}_z \end{bmatrix} = 10^{-3} * \begin{bmatrix} -0.029 & 0.101 & 17.50 \\ 0.029 & -0.091 & 0.328 \\ -0.13 & -0.051 & 0.516 \\ 0.004 & -0.003 & -0.019 \\ 0.006 & 0.003 & -0.091 \\ 0.003 & -0.007 & -0.019 \end{bmatrix} \begin{bmatrix} \delta_{RW} \\ \delta_{LW} \\ \Delta \omega \end{bmatrix} \quad (5.1)$$

$$\begin{bmatrix} \Delta \bar{X} \\ \Delta \bar{Y} \\ \Delta \bar{Z} \\ \Delta \bar{M}_x \\ \Delta \bar{M}_y \\ \Delta \bar{M}_z \end{bmatrix} = 10^{-3} * \begin{bmatrix} 0.092 & 1.863 & 17.50 \\ -0.091 & -0.294 & 0.328 \\ -0.123 & 0.059 & 0.516 \\ 0.005 & 0.006 & -0.019 \\ 0.016 & 0.000 & -0.091 \\ 0.001 & -0.009 & -0.019 \end{bmatrix} \begin{bmatrix} \delta_{RW} \\ \delta_{LW} \\ \Delta \omega \end{bmatrix} \quad (5.2)$$

$$\begin{bmatrix} \Delta \bar{X} \\ \Delta \bar{Y} \\ \Delta \bar{Z} \\ \Delta \bar{M}_x \\ \Delta \bar{M}_y \\ \Delta \bar{M}_z \end{bmatrix} = 10^{-3} * \begin{bmatrix} 0.1361 & 0.1361 & 32.84 \\ 0.1621 & -0.1621 & 0 \\ -1.5134 & -1.5134 & 0 \\ -0.1167 & 0.1167 & 0 \\ 0.0496 & 0.495 & 0 \\ -0.0022 & 0.0022 & 0 \end{bmatrix} \begin{bmatrix} \delta_{RW} \\ \delta_{LW} \\ \Delta \omega \end{bmatrix} \quad (5.3)$$

Load cell results show marginal results at best. The variability in the foam wings and variability from one side to another make it difficult to find any reasonable trends. Not to mention that the average moments are barely over the resolution level for the load cell. Other forms of control testing are tethered control. Successful tests were done restricting five degrees of freedom and letting the vehicle move forward and backwards on a string, or rotate about the lift axis. Successful tether tests were performed with different sets of wings and showed promise utilizing the AOA control. However the wings still proved to be the largest benefit or fault of the vehicle as a whole. Further control methods were postponed and remain outside of the scope of this paper. Stability is another major concern for any flying vehicle, especially horizontal flapping MAVs and remains also outside the scope of this paper. The following results discuss the efforts put into wing design and performance. Maximum lift achieved at 3V with foam wings was 12 gf. Wings described in the following section will achieve lifts of over 38 gf.

Wing Comparisons

After gaining some confidence and experience making carbon fiber wings, several sets of wings were made and tested utilizing the lever balance to evaluate lift. All wings were tested using a single motor to flap both wings. This method alleviates the need to maintain wing synchronization and commutate the motors using the AFRL control scheme. A COTS speed controller and a bench top power supply were used for commutating and powering the motor. The power supply was set to 8.1 V for all testing except the 38 gram lifts which were both run at 8.4 V, the maximum charge for a two cell battery. All testing was recorded using high speed cameras for frequency calculations. AOA data is also calculated using the imagery. Figure 5.3 shows the test results of 17 different wings with frequency vs. lift. A matrix of 4 wing layouts were chosen and adjusted by how much tow was used in each

trace. The A and B wings are smaller than the C, D, E, F, G and H wings. Wing Designs 1 and 3 did not generally perform well and had early failures as 6 of 8 number 1 designs failed and 5 of 8 number 3 designs failed. Designs 2 and 4 each had 6 of 8 wings not fail and generally had good performance over the desired lift range. The highest lift for each wing is at the largest incremental lift before power saturation for the motor. The addition of 3.2 grams was too much for the motor to overcome. Only 2F and 2E were able to lift 38.4 grams of mass at 8.4V.

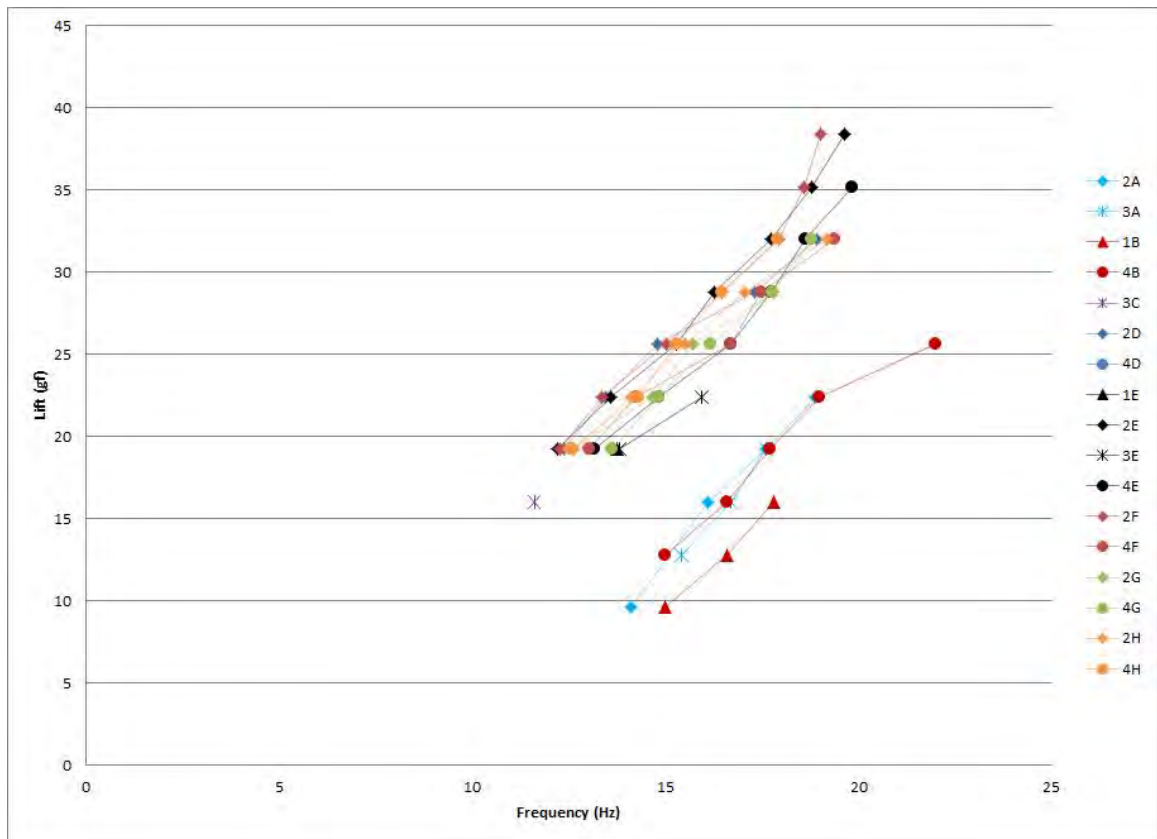


Figure 5.3: Wing Lift Testing Results [83]

Frequency calculations are accurate to within plus/minus 1 frame or 0.0005 s at the 2000 frame per second rate. Masses used are certain to within 0.1 g. The sensitivity of the lever balance is better than 0.2 g. The frequency of the flapper was adjusted via throttle control to achieve level balance and maintain equal lift to weight of the applied

mass. While uncertainty is inherent to any system, it is believed that the added inertia of the lever maintains a reasonable measurement of lift. Nano-17 load cell measurements proved to be very noisy having standard deviations more than twice as large as the average value. Surprisingly the average of the measurements were reasonably consistent with lever balance results indicating noisy but accurate mean measurements.

The high speed video data was processed utilizing the top view camera. The processing was done by a program developed by Sigthorsson of AFRL and uses MATLAB to trace and process the images [84]. The program uses the top view projection of the wing and a template wing to determine the angle of attack of the wing. The bending of the leading edge is compensated for in plane bending and ignores any out of plane bending. Curvature of the wing is also ignored. Only one wing on any given model was processed due to the field of view available. The program calculates the AOA based on the wing chord at multiple locations along the span of the wing. Linear approximations are used with trigonometry to estimate the AOA along the span of the wing.

Understanding the following AOA figures should begin with understanding the axes. The y axis is the location along the span of the wing from root at the bottom to tip at the top of the figures. Any given vertical line on the graph is a single point in time. The plot should be viewed as if the “wing” is the vertical line traversing horizontally in time. Each plot consists of one cycle and begins and ends at the same point in the mechanism for all wings and lifts. AOA near the root of the wing should be ignored due to there being no surface area, only the leading edge spar is located in these areas which generates useless measurements for the AOA. This refers specifically to the lower portion of the graphs from 0 on the y axis to approx 15. These were included to maintain a reference to root of the wing that was consistent across all wings. The color of the plot indicates the AOA of the wing at a given span location and point in time of the stroke. A darker color indicates a lower AOA, or more deflection. A lighter color indicates a higher AOA, or less deflection. Notice the stroke transitions are a light color as the wing goes vertical from one stroke to the next.

Wing designs 2D, 4D, 2E, 4E, 2F, 4F, 2G, 4G, 2H and 4H were processed for all lift values tested. Wing designs 2D, 2E, 2F, and 4H will be presented below. All other Figures

can be found in Appendix [A](#).

In addition to the magnitude of the measurements a noteworthy result can be highlighted which is the wing AOA oscillation that occurs when a wing has a loss of AOA in the middle of a wing stroke. It is typical that one direction may exhibit this dwell while the other will be smooth throughout the entire stroke due to the quick return of the four bar mechanism. In general the wing achieves a larger angle of attack at the beginning of the wing stroke that cannot be maintained through the entirety of the stroke due to the lack of aerodynamic and inertial forces to overcome the torsional stiffness of the wing. This dwell or oscillation is overcome when flapping faster. Specifically in Wing 2D, Figure [5.4](#) the oscillation can be found in lift measurements 19 thru 28. This can be found specifically in the plot as the AOA moves from a large AOA to a small AOA and back to a large AOA in a half cycle. The wings maintain a smoother AOA transition throughout both strokes when lifting the 32 gram mass.

Wing 2E and 2F produce the most lift of all the wings tested. Both have large tip deflections at the lowest tested load level and have AOA lower than 20 deg as far back as the wing mid span. For wing 2E found in Figure [5.5](#), the large deflections taper to approximately 30 degree AOA from the mid span to the wing root. As the load increases the time spent in the higher deflections increases with minimal change in wing deflection. The lower AOA or darker regions are spreading throughout the relative stroke times. The dwell is present in the wing until it reaches a lift of 32 grams. The leading edge bends significantly and seems to “whip” through the stroke when high speed video is investigated.

Figure [5.6](#) shows the data for wing 2F. The AOA spreads throughout the stroke similar to wing 2E, however, in addition to the longer duration, the lower AOA is driven deeper towards the root of the wing as lift increases. Both wings exhibit large leading edge deflections. As the wing flaps faster, the relative AOA retards. The leading edge spar tends to bend and advance on the majority of the wing. While not groundbreaking this could be used to determine relative leading edge spar stiffness. Larger leading edge stiffness will not retard the AOA as much as a lower leading edge stiffness.

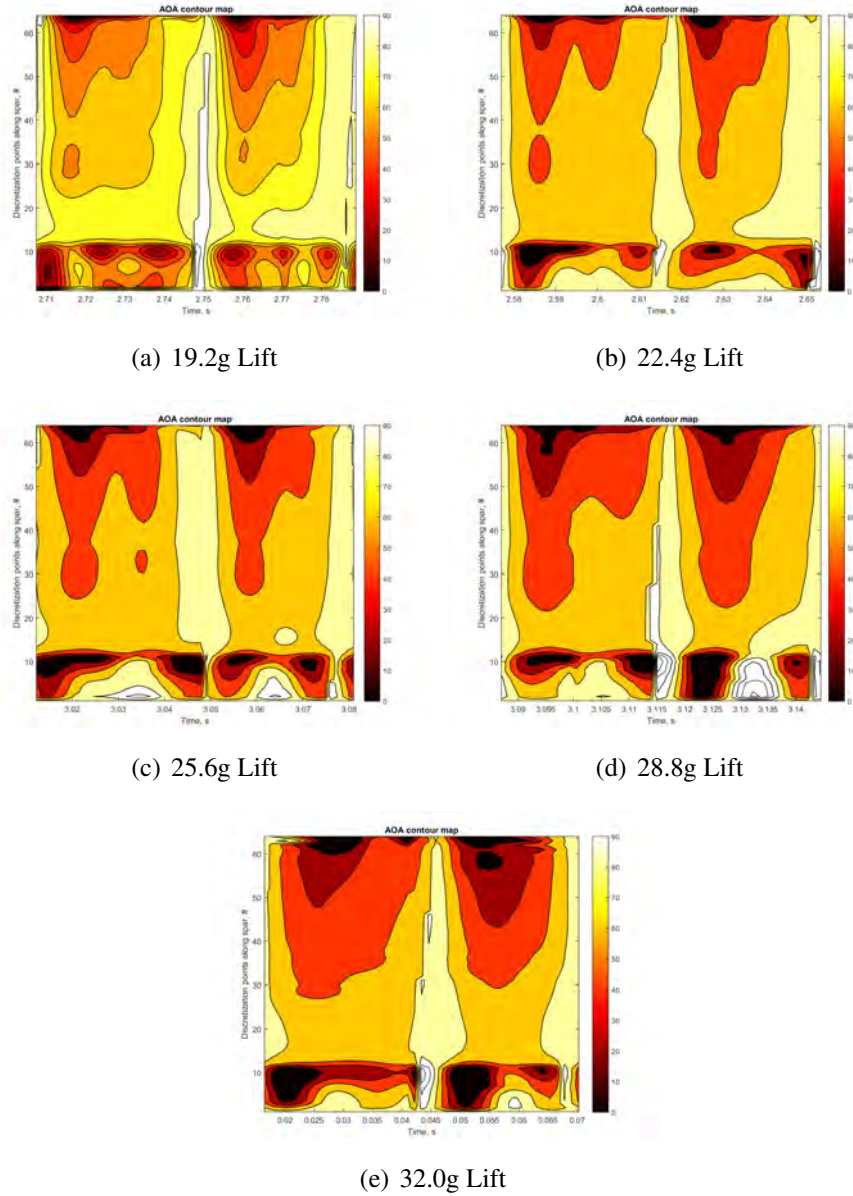


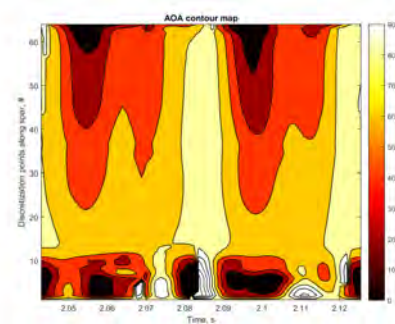
Figure 5.4: Wing 2D AOA Mapping

Wing 2H AOA profiles can be found in Figure 5.7. The leading edge, similar to other G and H wings, proves too stiff to lift more than 32 g. Wing oscillation exists through all lift levels. The wing leading edge does not exhibit any whipping effect, however deflections are similar in magnitude to other wings at the same lift levels. The frequency is similar to that of 2F as it is 19.2 Hz compared with 19.0 Hz respectively.

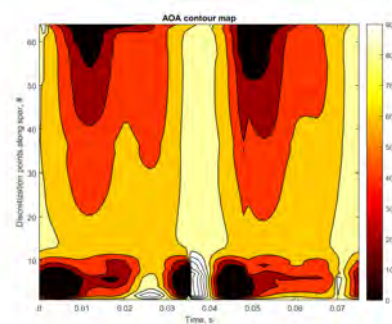
Note that the AOA of wing 2H is similar to that of wing 2E and 2F and flaps at 19.2 Hz

vs wing 2F at 19.0 Hz. Wing 2F flaps slower than wing 2H yet is lifting almost 20% more. The results show that 45 degrees is not the desired AOA for flapping wings. Drag, while useful for control, is difficult on a flapping mechanism and provides little benefit to the lift vector. Achieving AOA larger than 45 degrees should be expected for highly efficient flapping wings at a desired lift level.

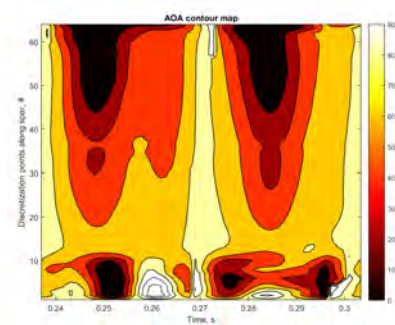
Also of note is the slight retardation of the AOA relative to the spar angle can be noticed as the frequency increases, this is due to the in-plane bending of the leading edge. The wing tip lags the root as the frequency is increased thus the root leads the wing at a more significant amount and looks like a retardation of the AOA relative to the wing stroke. The retardation is simply relative to the stroke duration as the x-axis includes one full cycle. Notice specifically that the darker regions of AOA move toward the right side of the plots as the wings flap faster.



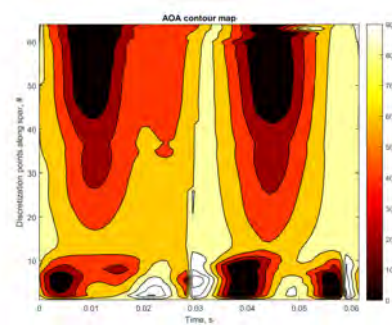
(a) 19.2g Lift



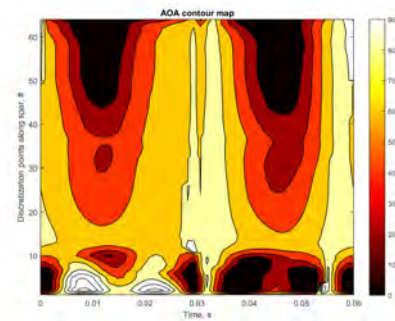
(b) 22.4g Lift



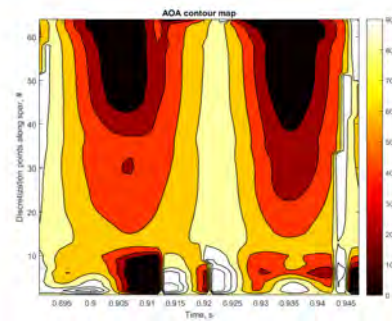
(c) 25.6g Lift



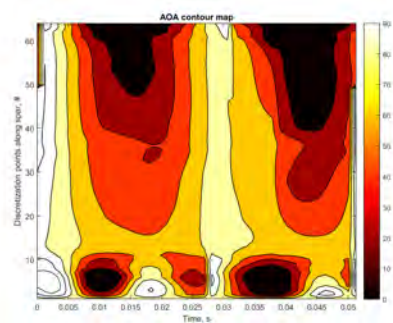
(d) 28.8g Lift



(e) 32.0g Lift

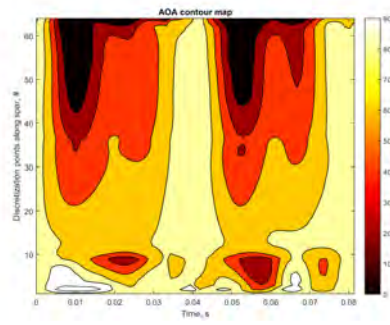


(f) 35.2g Lift

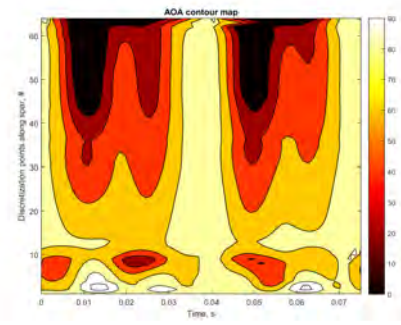


(g) 38.4g Lift

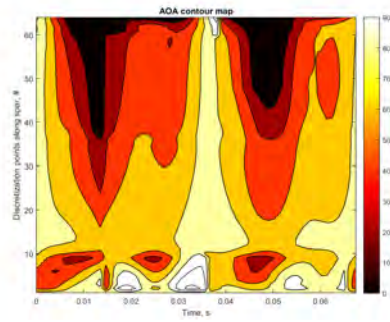
Figure 5.5: Wing 2E AOA Mapping



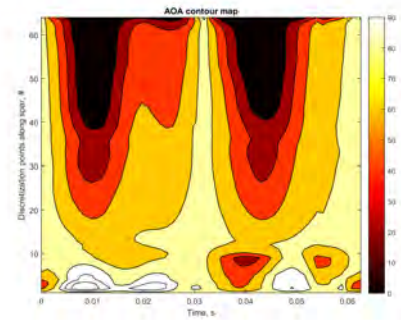
(a) 19.2g Lift



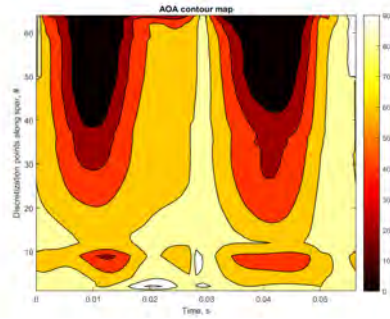
(b) 22.4g Lift



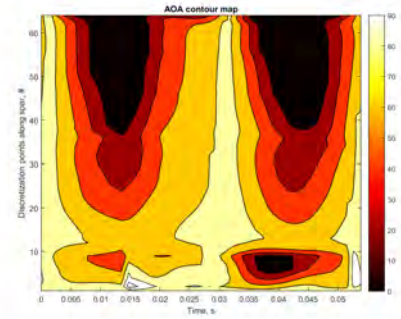
(c) 25.6g Lift



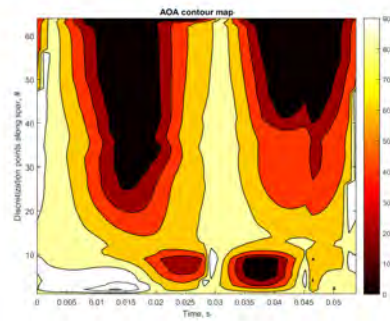
(d) 28.8g Lift



(e) 32.0g Lift

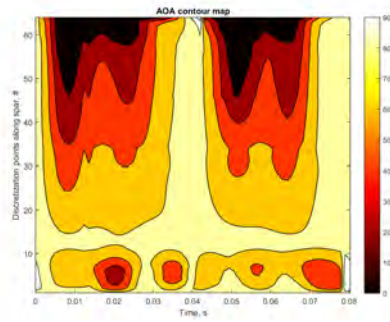


(f) 35.2g Lift

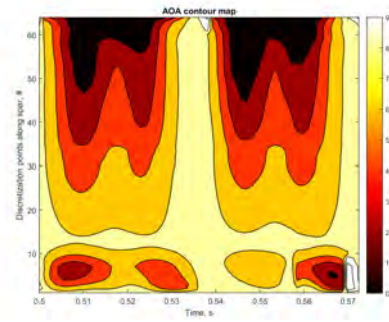


(g) 38.4g Lift

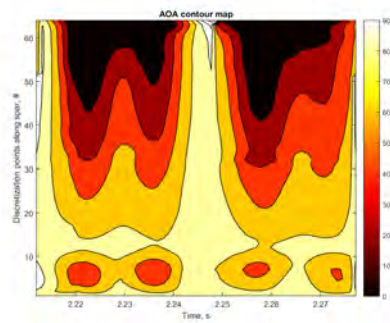
Figure 5.6: Wing 2F AOA Mapping



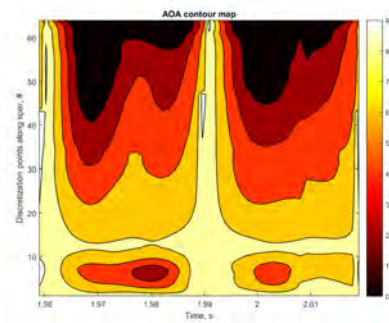
(a) 19.2g Lift



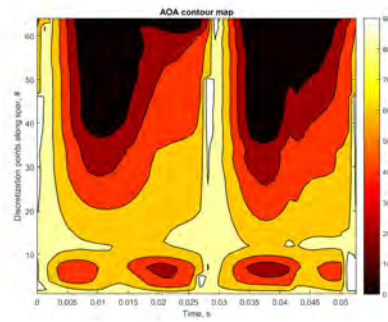
(b) 22.4g Lift



(c) 25.6g Lift



(d) 28.8g Lift



(e) 32.0g Lift

Figure 5.7: Wing 2H AOA Mapping

5.2.3 Experimental Conclusions

Wings 2E and 2F demonstrate the largest lifts of all the experiments. The 2H wing that has similar AOA and frequency to the other wings provides 20% less lift. AOA, frequency and wing moment of area are used to calculate lift according to Sane and Dickenson. Even though these are very similar for three sets of wings, 2 have show lifts 20% greater than another. This indicates that some complex effect must be providing the wings with more lift. Hypothesis to why this occurs are a “whipping” effect of the leading edge through the stroke or some other complex aerodynamic action; it is clear that all effects are far from fully understood. The highly dynamic and coupled nature of these systems further demonstrate the need to test and evaluate under flight load and weight conditions. Solving these problems requires more than matching Reynolds numbers, the inertial effects of the wing effect the flapping and require a non dimensional equivalent or in situ testing. The development of a non dimensional equivalent is outside the scope of this dissertation. Phase-lock PIV is used to visualize the flow generated by this complex, highly coupled system. While exact wings used here are not tested, the reversal effects are investigated to attempt to understand the impact of amplitude on flow patterns at the stroke reversal for three amplitudes, namely 120, 150 and 180 degree flapping amplitudes.

5.3 Phase-Lock Particle Image Velocimetry (PIV)

Determining the flow fields that are generated by flying vehicles is key to understanding the fluid mechanics of the system. Steady flow applications such as airplane wings can provide flow field visualization in wind and water tunnels with relative ease. Seeding the air with smoke or water with dye are easy ways to see how vortexes are developed and shed. For highly unsteady applications such as flapping wing MAV's, a more ingenuitive means of seeing flow fields is required. Several researchers have used oil and water baths to learn about the flow fields of flapping wings. The significantly higher viscosity of water and oil relative to air allows the flapping cycle to be slowed significantly and scaled larger. This becomes much easier to visualize the flow fields at equivalent low Reynolds numbers. The complication comes with accurately scaling the wing stiffness of the insects that are being studied. Typically, rigid "wings" are controlled using large motor apparatus's prescribing amplitude, angle of attack, and rotation time as well as timing [31, 39, 52, 53]. While not completely representative of the insects they are studying, certainly lessons can be learned from such experiments. Deluca has performed such in situ experiments but focused primarily on the supination and pronation of the flapping cycle. [50] Furthermore, only one wing was used for the experiments and thus any wing interaction effects would be lost.

In an attempt to include the inertial effects which are influential to the wing shape and consequently to the flow fields, a phase-lock PIV system was used to capture flow fields generated by the mechanism and wings at both wing reversal and mid-stroke. The PIV system uses smoke to seed the air. A laser is then used to illuminate the smoke particles. A high speed camera then takes two snapshots very close in time. The time step between photos is precisely controlled and the distance traveled by the particles in that time is calculated between the two photos. The distance and time are then divided to provide a velocity map of all the particles that are captured and illuminated in the picture. Due to the highly dynamic nature of flapping wing vehicles, PIV can provide "messy" results during a single image capture. To alleviate some of this variation, a method was developed to take many measurements at the same point in the flapping cycle. This type of PIV is called phase-lock PIV [85].

The two wing flapper utilizes a 180 degree flapping amplitude to maximize wing interaction and minimize wing reversals. To test the effects of wing interaction, an experiment was done to investigate the flow at the wing reversal for interactions. Phase-lock PIV was implemented to investigate the flow patterns during these interactions. Furthermore, two other flapping amplitudes, namely 150 degree and 120 degree were tested to compare with the larger 180 degree flapping angles. Every wing reversal requires significant motor effort to change the wings direction. For this testing the average wing velocities were made equal in attempt to provide as even of a test from one flapping amplitude to another from a blade element theory standpoint.

5.3.1 Experimental Setup

The phase-lock PIV system consists of a double pulse Nd:YAG laser, tachometer, two digital delay generators, high resolution CCD camera, computer, optical lenses, mirror and the vehicle. A layout of the system can be found in Figure 5.8. The Nd:YAG laser and camera are connected to one of the delay generators to synchronize the laser and the camera. The tachometer is connected to a second delay generator which triggers the first delay generator. The second delay generator times the delay after the tachometer pulses, providing adjustment of the vehicle phase to the laser. Laser sheet thickness is approximately 2 mm and the time between pulses is 100 μ s. A strip of reflective tape is put on the crank gear. This gear only makes one revolution per cycle and thus every pulse from the tachometer provides a specific time in the flapping cycle. The air was seeded with a water-based fog generator which provided $\approx 1\mu$ m diameter droplets. Initial pictures are taken to evaluate smoke thickness and camera focus. Achieving good results is more an art than science. One must be aware of reflections from wings and metals as reflections can provide bad results or even break the camera if impinging upon the optical sensor. Historically, 200 cycles per test were desired to provide the best averaged results, however for these tests, good results were achieved with 50 snapshots. Due to laser restrictions on duty cycle, a capture cannot be taken every cycle of the wings. If the laser cycles too fast, it does not have enough time to recover causing a weaker beam which provides poor results.

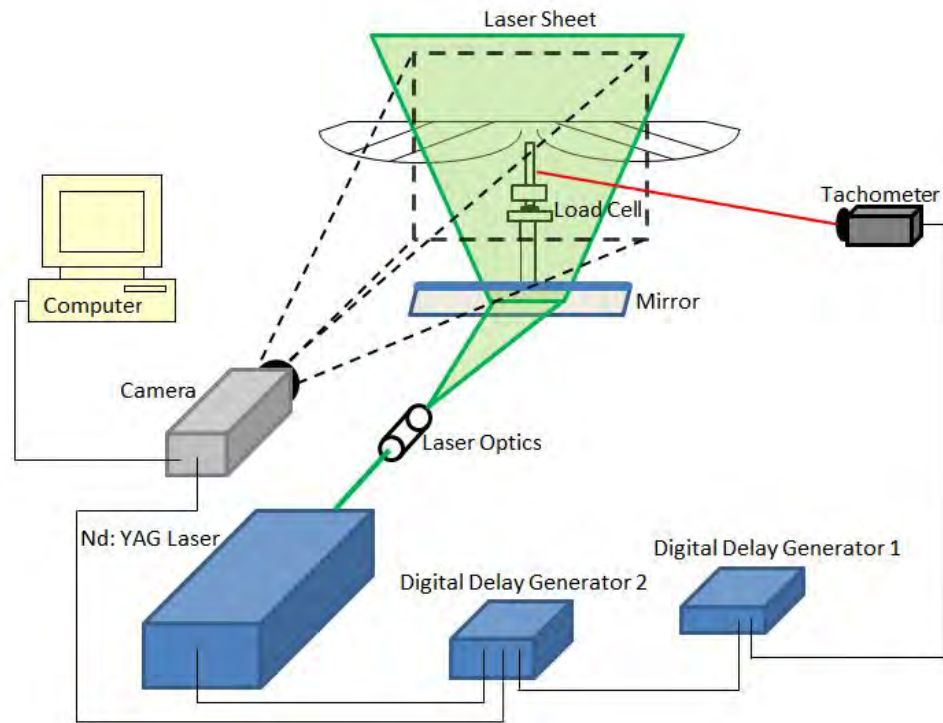


Figure 5.8: Phase-Lock PIV Schematic

While 200 snapshots may take 3-4 minutes to acquire, 50 cycles only takes 1 minute to acquire. To maintain wing and mechanism integrity, 50 snapshots were chosen. While 5 minutes is not a long flight duration, 30 different locations requires a minimum of 2 hours of flapping. Not to include any data that needs retaken versus the 30 minutes of flap time required using the 50 snapshot data. Even if a mechanism is able to withstand several hours of flapping, wing degradation is a serious concern when trying to determine flow fields.

The same wings and vehicle were used for every test. Modification to the coupler location on the crank gear was varied to provide different amplitudes. A brushless motor was used to drive the mechanism via a bench top power supply, COTS speed controller, and Spektrum transmitter and receiver. Frequency was adjusted using the throttle control and tuned in using the tachometer.

5.3.2 Experimental Results

Six flapping positions per flapping amplitude were chosen for investigation at the wing reversal and three at the mid-stroke. All wing positions are determined by adding or subtracting the time from the delay generator. The cycle time, divided by twenty-four was used to increment fifteen degrees. Kinematics of the mechanism are ignored, only the average crank velocity is used to estimate wing position. This is apparent upon investigation of the pictures found in Figures 5.10 and 5.11. At the end of the flapping stroke there is a slight leading edge dwell. The dwell occurs between “0 degrees in” found in Figure 5.10 and “0 degrees out” found in Figure 5.11. This dwell is caused by looseness in the mechanism and the pause of the leading edge as the wing flips. Additionally the wing reversal causes a higher load on the motor which will generally cause the motor to slow and in extreme cases stall. Due to the relatively low deflection, very little can be learned from the flip that is seen in the higher loaded wings. The increase in frequency from the 180 to the 120 amplitude does however provide larger wing deflections at reversal even though cycle averaged velocity remains constant as evident in Figures 5.10 and 5.11. The position, velocity and acceleration plots for the individual mechanisms are shown in Figure 5.9. The mean acceleration of the 120 amplitude is 50% higher than the mean acceleration of the 180 amplitude and the 150 amplitude is 20% higher than the 180 amplitude thus providing reason for the larger AOA for the higher cycle averaged angular accelerations and further demonstrating the need to perform in situ testing as the increase in inertial wing loading shows significant differences in wing deformation.

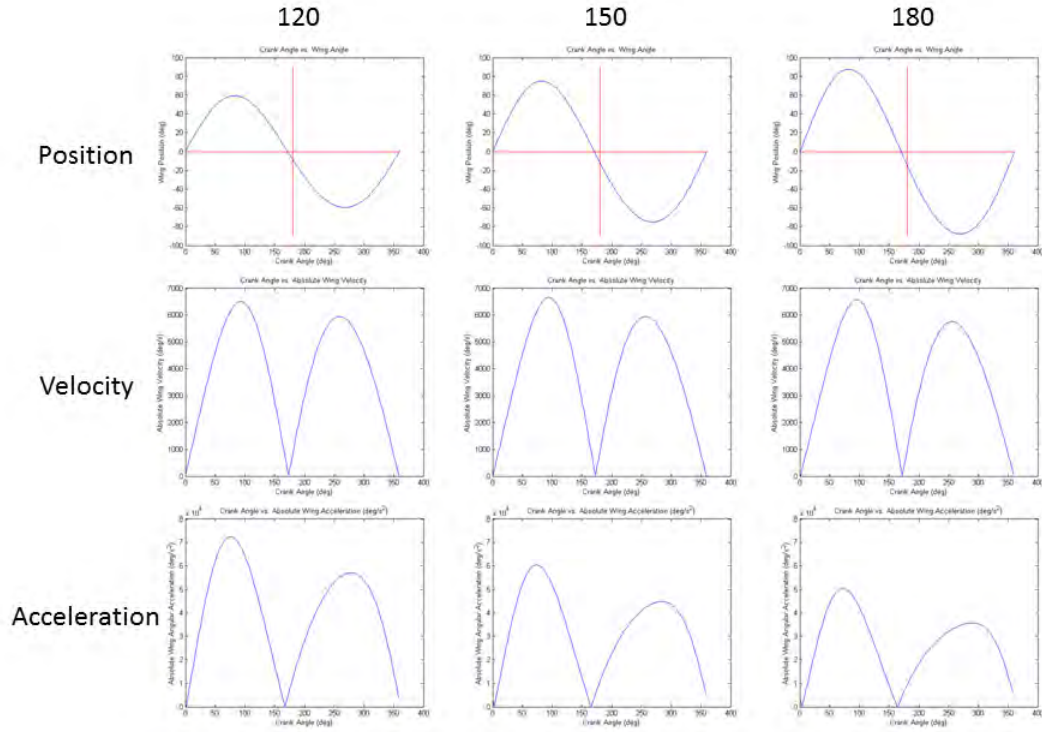


Figure 5.9: Mechanism Kinematics for Flapping Amplitudes and Frequencies

Stroke Reversal Measurements

All flow fields are positioned for 75% span of the fully clapped wing. The results only show the 2-D flow field at one wing span location. Wing deformation on entry to the wing reversal is mostly undeformed. Higher load/frequency flapping lends to large deformations at the reversal, however, flow fields remain sufficient for measurement under the low wing deflections. X and Y direction scales are measured in millimeters spanning approximately 368 mm in the x direction and 275 mm in the vertical direction.

The program used to calculate the flow fields outputs a grid of vectors in the x and y directions. These vectors are then averaged over a given data set and vorticity is calculated. The following figures ranging from Figure 5.12 to Figure 5.33 show the corresponding

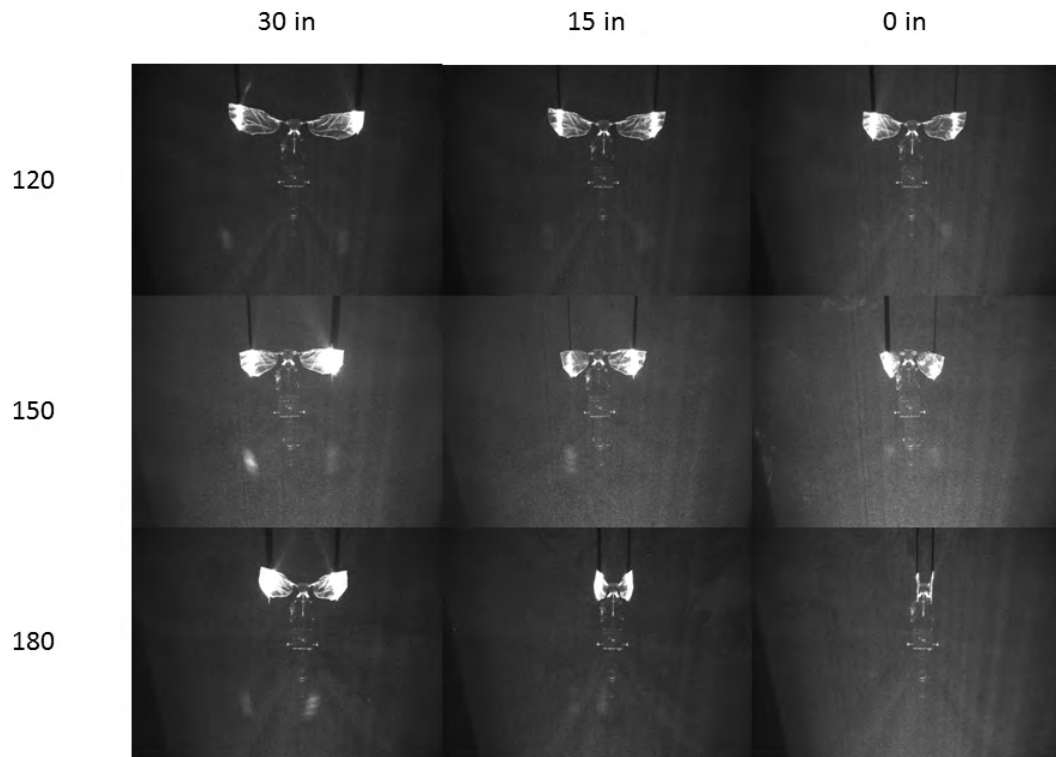


Figure 5.10: PIV Wing Locations

velocity vectors overlaid on the vorticity magnitude. Vorticity is the curl of the velocity field. Data within several pixels of the wings should not be expected to be accurate as well as the general area between the wings where the mechanism resides as it can cause reflections. Reflections from the laser cause the illuminated smoke to wash out in the photos and thus the calculations are inaccurate. Filtering has been done to remove significant problems resulting from the reflections.

A red magnitude represents a rotation in the clockwise direction. White on the plots indicate low or no vorticity. Blue on the plots indicate a counter-clockwise rotation. The blue arrows are the velocity vectors overlaid on the vorticity. These vectors indicate direction and magnitude by the direction they are pointing and the size of the arrow. More quantitative contour plots for the velocity are located in Figures 5.35 thru 5.37 and Fig-

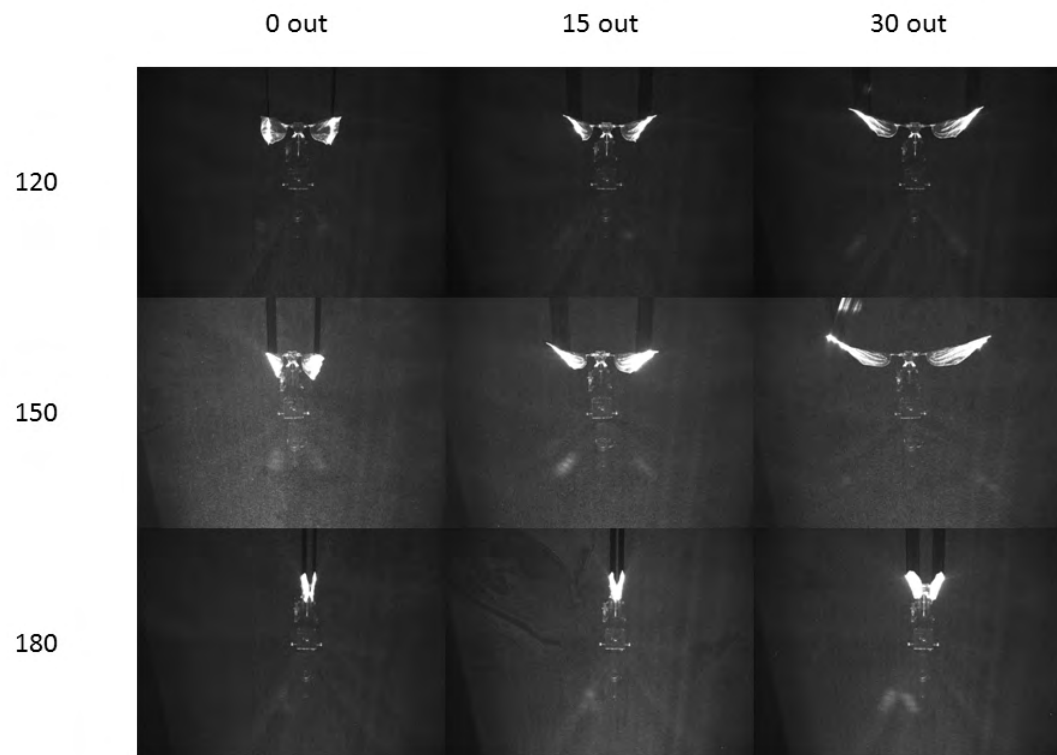


Figure 5.11: PIV Wing Locations

ures [A.6](#) through [A.8](#) for the wing reversals. Flow patterns will be discussed between the various time steps as the flow develops as well as comparisons between the three flapping amplitudes. Flow directions, and vortexes will be of particular note as they are the phenomena that generate pressure gradients on the wings which generate lift.

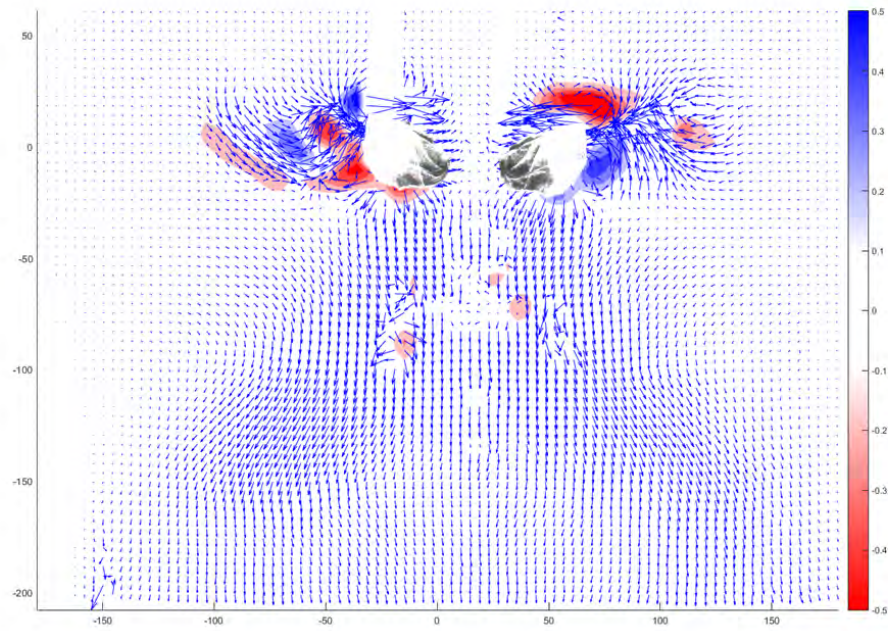


Figure 5.12: PIV 30° in 180 Amplitude Vorticity

Figure 5.12 is the first capture of the 180 degree amplitude mechanism. The wings are moving toward one another and relatively symmetric flow is measured between the two sides. Between the wings in the general area of the mechanism is significantly lower velocities indicating that these measurements are not likely correct. Presumably the flow field below the mechanism is from the previous cycle. The flow generated by the wings as they are coming together can be found near the outsides of the wings. This wake from the wings will be of particular note for the remaining measurements.

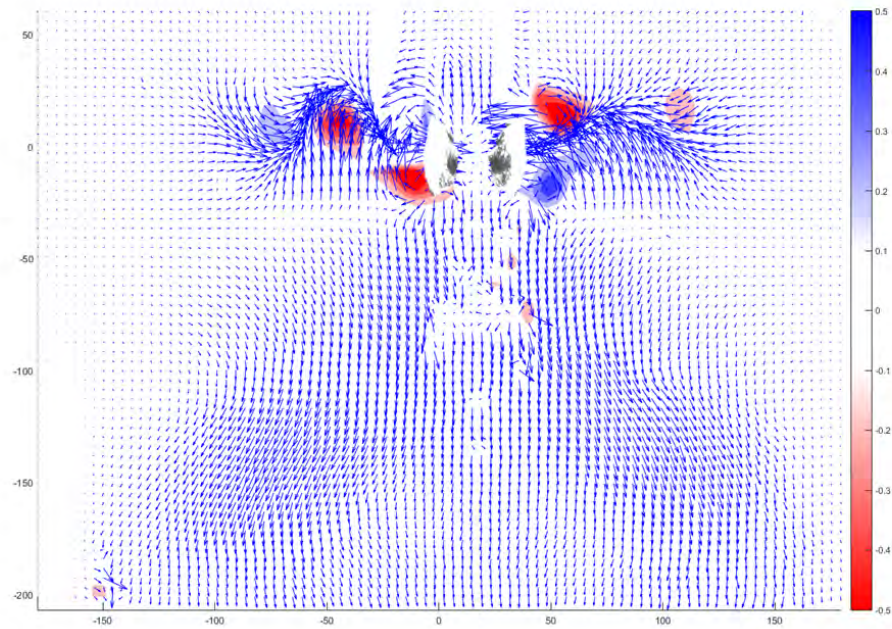


Figure 5.13: PIV 15° in 180 Amplitude Vorticity

As the wings come to the “15° in” wing position in Figure 5.13, a large flow is measured on the wing stroke plane. These flows appear to be diverging up and down from where the wing had just passed through. Very little flow is present above the wing as it enters the reversal. The flow however looks as if a velocity from above is beginning to generate a vortex. The more likely explanation is the flow from the vehicle side of the laser sheet is beginning to enter into the measurement area. 3-D flow measurements could confirm this theory. Regardless, large flow fields and vortices are generated following the wings at the 75% span plane.

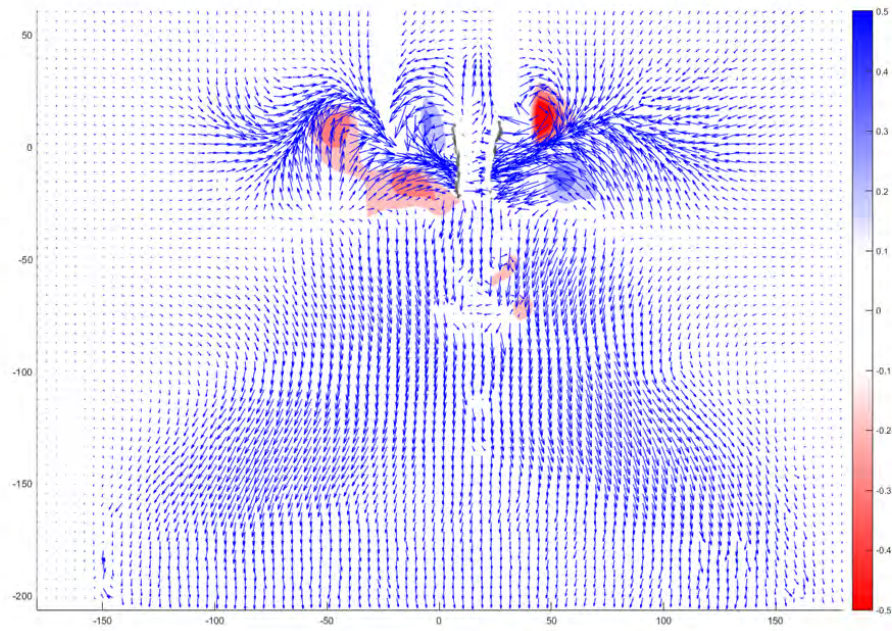


Figure 5.14: PIV 0° in 180 Amplitude Vorticity

Figure 5.14 occurs when the leading edge has reached its furthest extent, in the case of the 180 degree flapping amplitude, the wing is perpendicular to the camera providing the least intrusion in the view of the flow. The developing vortex from the previous time step begins coming into full view. The flow is impinging directly on the wing at this point giving a pseudo velocity on the wing as it is stopped. This is known as the wake capture phenomenon that was discussed in section 1.3.4.

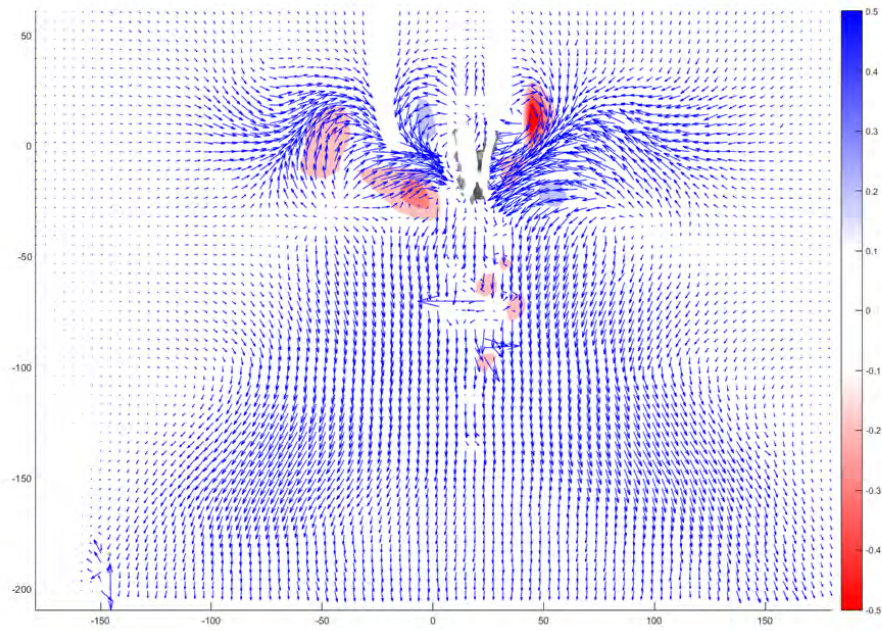


Figure 5.15: PIV 0° out 180 Amplitude Vorticity

The flow in Figure 5.15 has preloaded the wing and the mechanism has tightened up any slop, the wing is just about to begin moving. At this time the vortex in the measurement plane has dropped some in magnitude while maintaining its position. Flow on the right side of the wing is rolling into the wing at a lower position. While accuracy near the mechanism and wings is hard to confirm, a vortex appears above both wings from Figure 5.13 through Figure 5.16. Due to its appearance in four averaged data sets it is fair to believe this is an occurring phenomena. As the wings are clapped together at this relatively low frequency, the flow wraps around the top edge of the wing and some is ejected out the bottom.

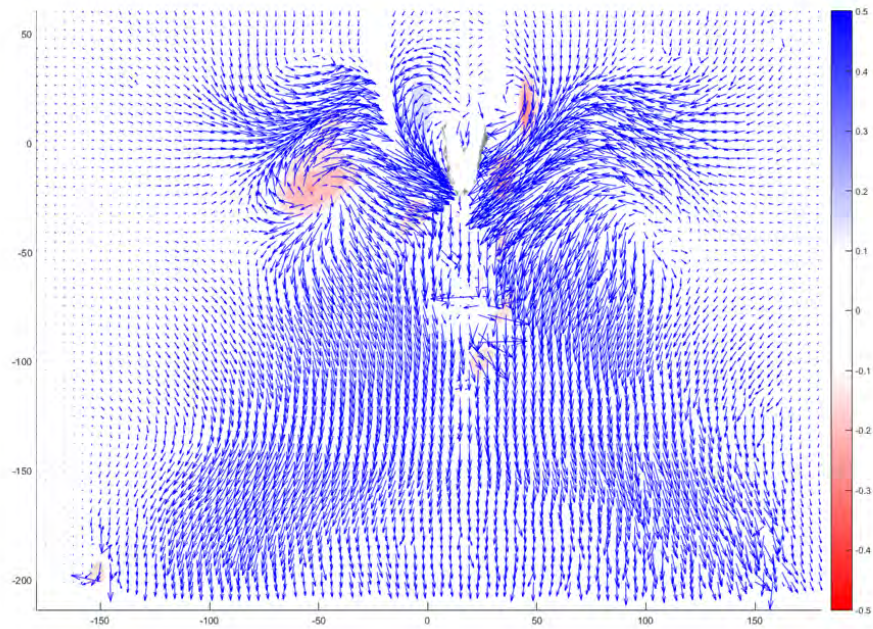


Figure 5.16: PIV 15° out 180 Amplitude Vorticity

Figure 5.16, “15 out”, shows the initial combination of both flow fields. The vortices on each side of the wing are impinging on the wings and combining into a significant downflow that will remain in the measurement plane until the next cycle begins. The trailing vortex comes into full view, with the center of the vortex near the center of the wing.

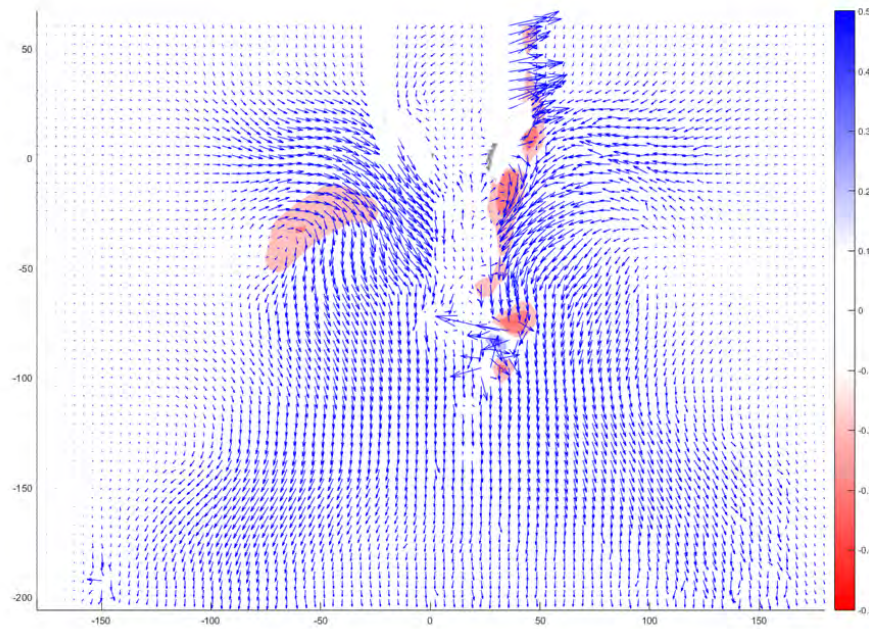


Figure 5.17: PIV 30° out 180 Amplitude Vorticity

The vorticity from “15 out” is now being fully captured by the wings in Figure 5.17. The vortex is being pushed below the wings and general flow is following a uniform flow below the wings. The apparent strong flow above the right wing should be ignored as the measurement is likely not real due to the shading of the laser by the wings. The shading can easily be seen in Figure 5.11 where above the wings is darker than the rest of the image. This is the first frame where the wing tips are not near touching.

Due to the longer duration of the end of stroke dwell seen by the 180 degree amplitude flapping mechanism, the wings did not open to 30 degrees during the prescribed time duration. In an attempt to gain more insight two more wing locations were captured in Figures 5.18 and 5.19. These locations are by calculation 35° and 45° out.

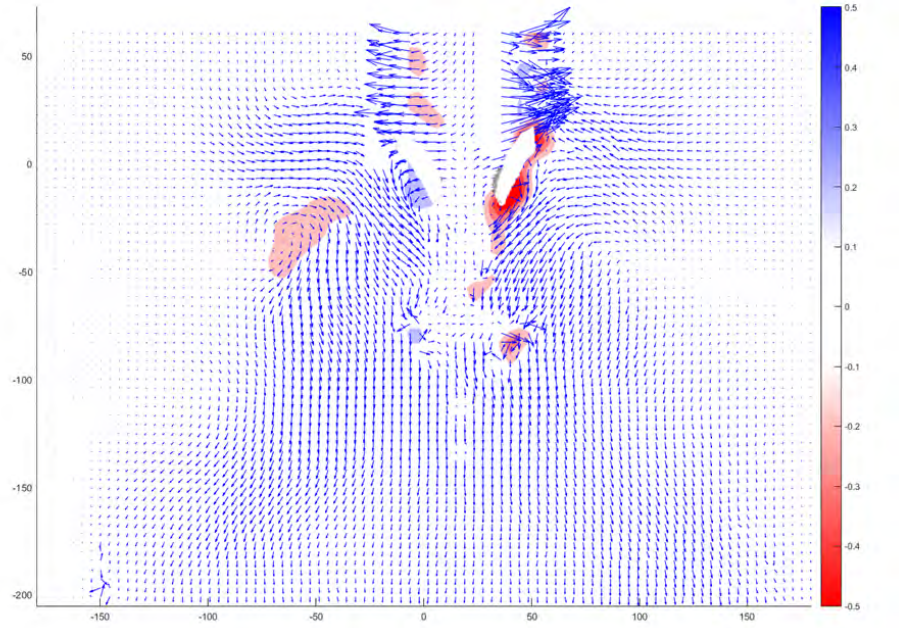


Figure 5.18: PIV 35° out 180 Amplitude Vorticity

The left vortex is still visible in Figure 5.18 though it is dissipating. Wake capture is still occurring, notice the flow field as it moves towards both wings as they are beginning to travel on the next stroke. Flows directly above the wings should be ignored due to laser shading and reflections.

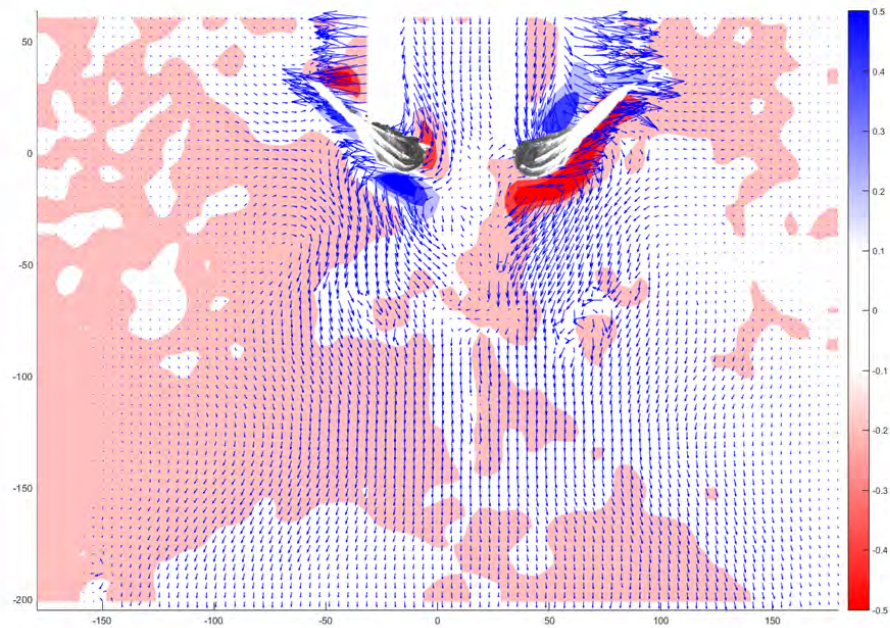


Figure 5.19: PIV 45° out 180 Amplitude Vorticity

Although the wings are not physically at the 45° out position in Figure 5.19, the wings have made significant travel relative to the previous time steps. The vortex is still present although the plot does not distinguish it well. Flow toward the wing is significantly smaller indicating that the majority of the wake has been dissipated in this plane. The wings are now spread enough that the flow above the mechanism is able to be measured and shows a down flow.

Figure 5.20 shows all six plots on a single page to visualize the progression of flow. The large arrows represent general flow patterns.

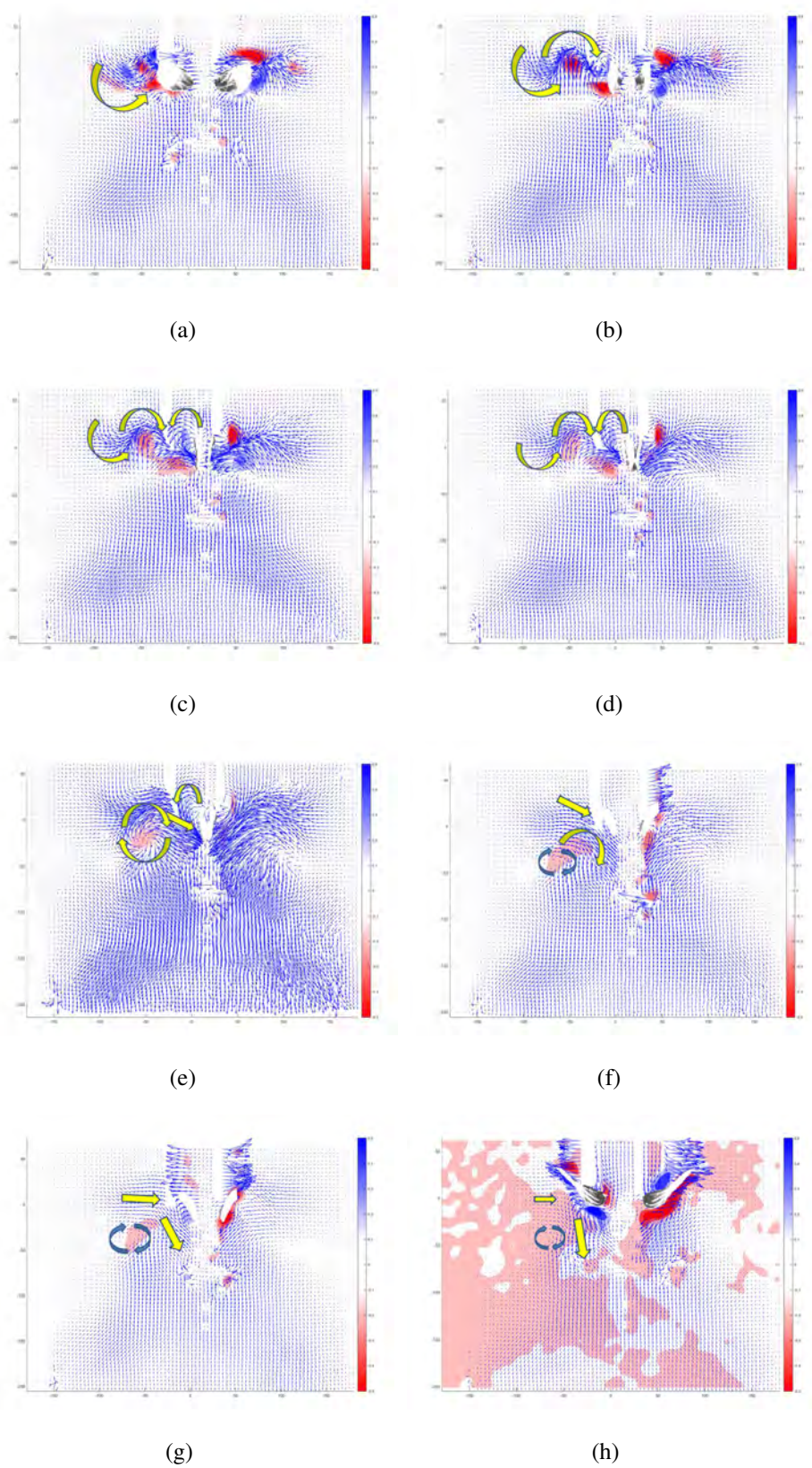


Figure 5.20: PIV 180 Amplitude Quiver Plot

The average lift generated by the 150 degree amplitude mechanism was similar to the 180 degree mechanism, however both produced lower lift than the 120 degree mechanism. The following Figures 5.21 through 5.26 plot the vorticity with the velocity vectors overlaid.

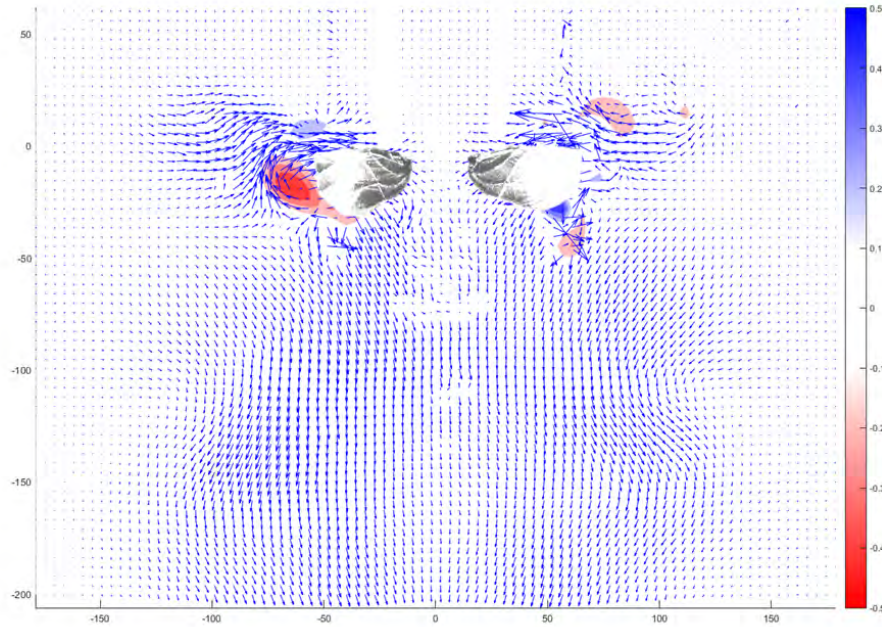


Figure 5.21: PIV 30° in 150 Amplitude Vorticity

Figure 5.26 is the first data point taken on the approach of the wings toward the reversal. Similar to the last set of data, a velocity field in the down direction is apparent before the wings have enough time to effect on the velocity below the vehicle indicating flow continuing from the previous stroke. A wake is generated by the left wing however the right wing has a significantly less flow following the wing.

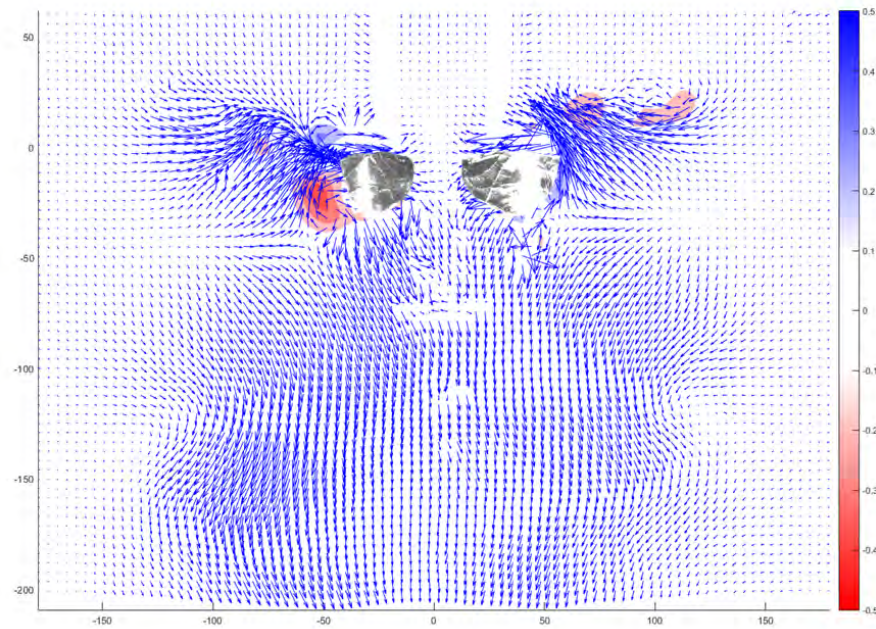


Figure 5.22: PIV 15° in 150 Amplitude Vorticity

Figure 5.22, “15 in”, has more flow enter the measurement plane from the right wing. More up-flow is occurring beginning at the lower tip of the wing on both sides. The left wing shows indication of the flow curling down towards the leading edge, however the right wing flow continues up above the leading edge. This would result in loss in lift and an inefficient flow field. It is preferable to catch as much of that flow with the wing and avoid any losses and possibly negative effects of this flow over the leading edge.

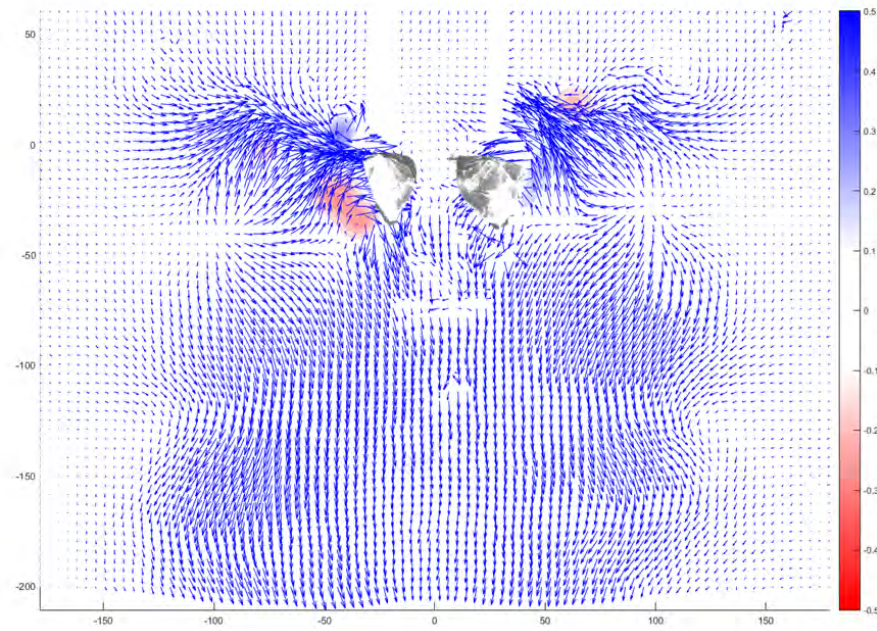


Figure 5.23: PIV 0° in 150 Amplitude Vorticity

The flow pattern of Figure 5.22 continues into Figure 5.23. Flow into the left wing is curling into the leading edge and the right wing continues up past the leading edge. A general flow field in the down direction is maintained. The flow field here is wider than the 180 degree amplitude but will be shown later to be less in magnitude in the y velocity plots.

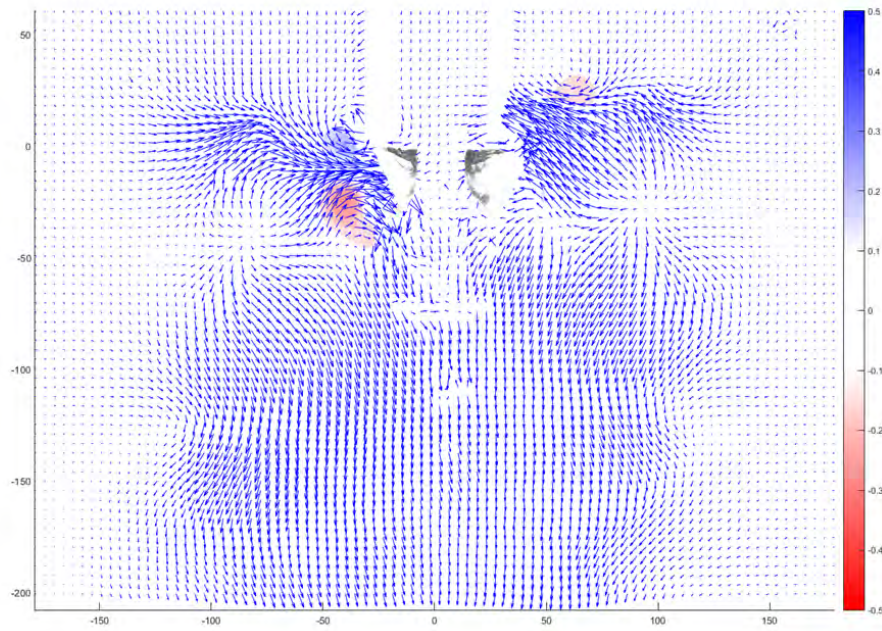


Figure 5.24: PIV 0° out 150 Amplitude Vorticity

Figure 5.24 continues to show wake capture by the left wing and overall good flow patterns while the right wing continues to have flow passing above the leading edge. The trailing edge vortex from the previous stroke is maintained as the wing reverses and catches the wake. The direction of the vortex indicates a trailing edge vortex shed from the previous stroke. The vortex is not as strong as the 180 degree vortex, but maintains the trend.

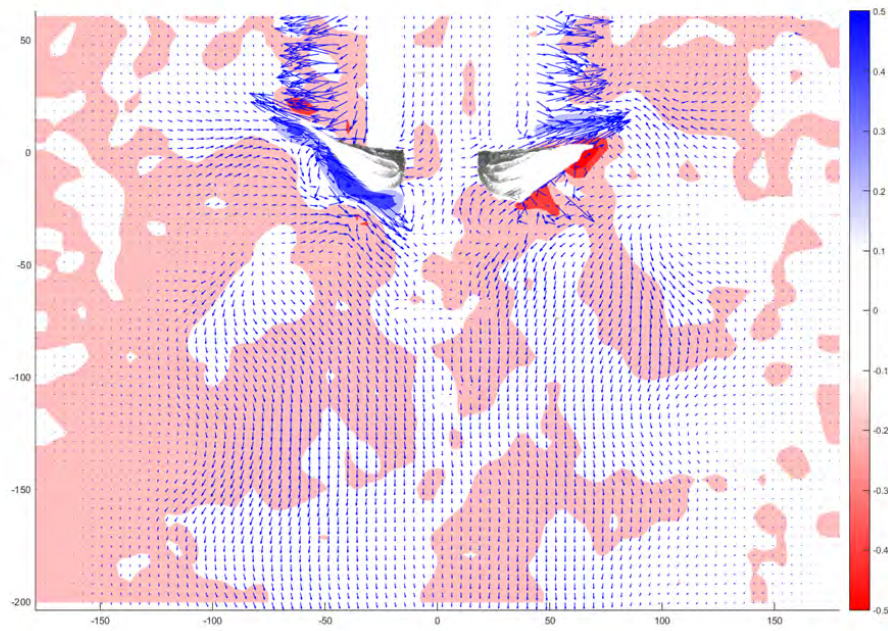


Figure 5.25: PIV 15° out 150 Amplitude Vorticity

Figure 5.25, “15 out”, shows flows approaching the left wing still from the previous wake. The right wing wake is still moving over the leading edge and does not appear to be providing any apparent pseudo velocity to the right wing. The large vectors above the wing should be ignored due to laser sheet shading and reflections by the wings.

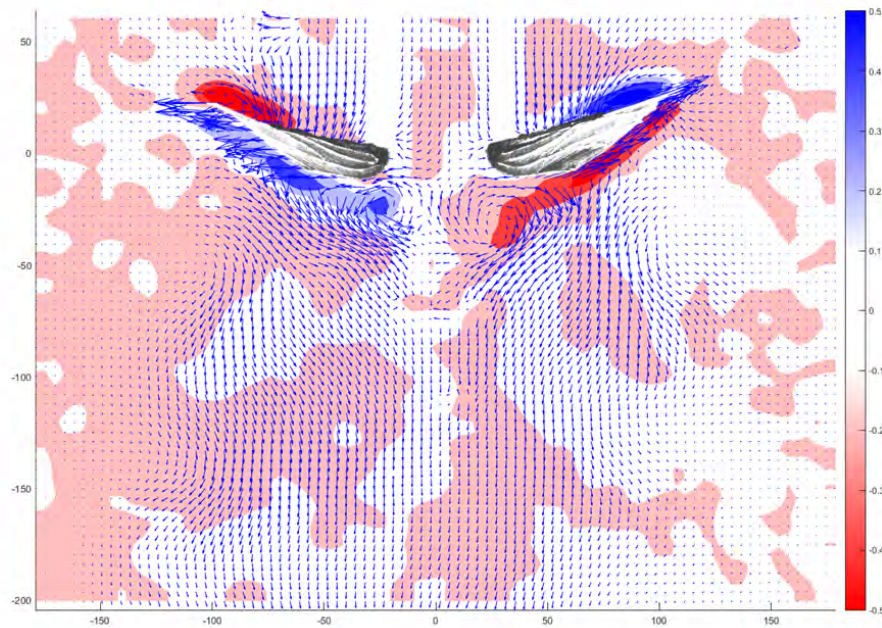
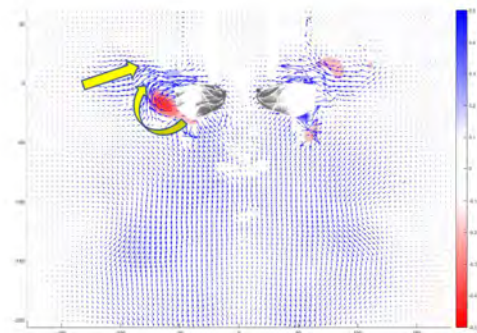


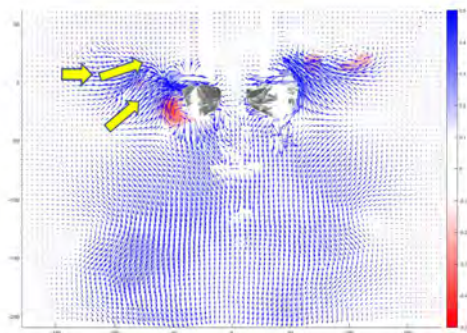
Figure 5.26: PIV 30° out 150 Amplitude Vorticity

Figure 5.26, “30 out”, wings are well spread, the trailing edge vortices are developing on both wings. Both wings are well deformed and generating good down-flow. Flow in the general directions are similar for right and left wings and wake capture is present although small.

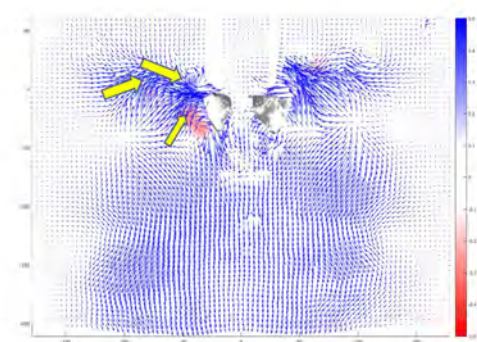
Figure 5.27 shows all six plots on a single page to visualize the progression of flow. The large arrows represent general flow patterns.



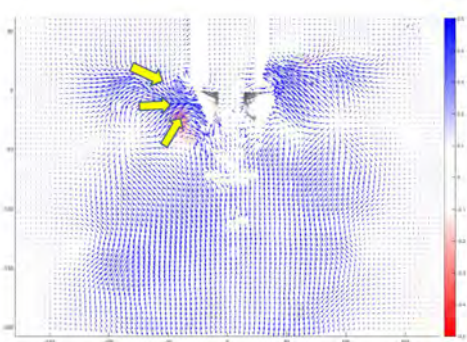
(a)



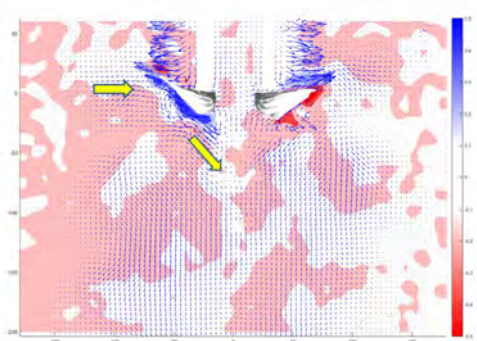
(b)



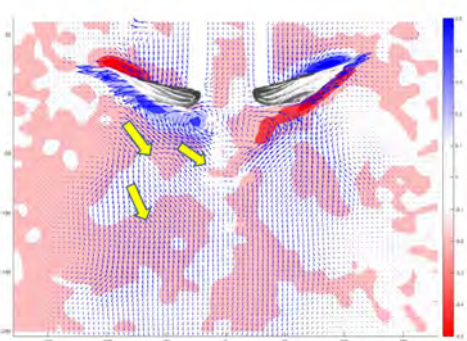
(c)



(d)



(e)



(f)

Figure 5.27: PIV 150 Amplitude Quiver Plot

The smallest amplitude wing produced the highest lift. Although the cycle averaged velocity is equal to the others, the wings achieve larger, better angles of attack leading to better lift. The angular acceleration on the wings is largest for the lesser amplitude mechanism causing the wings to have larger inertial effects. Larger magnitude flow fields are generated by the 120 degree mechanism, however the flow fields appear to have very little interaction with one another and have less coverage of the 2D area than the 180 degree amplitude mechanism. Figure 5.28 is the first measurement of the wing reversal. At this

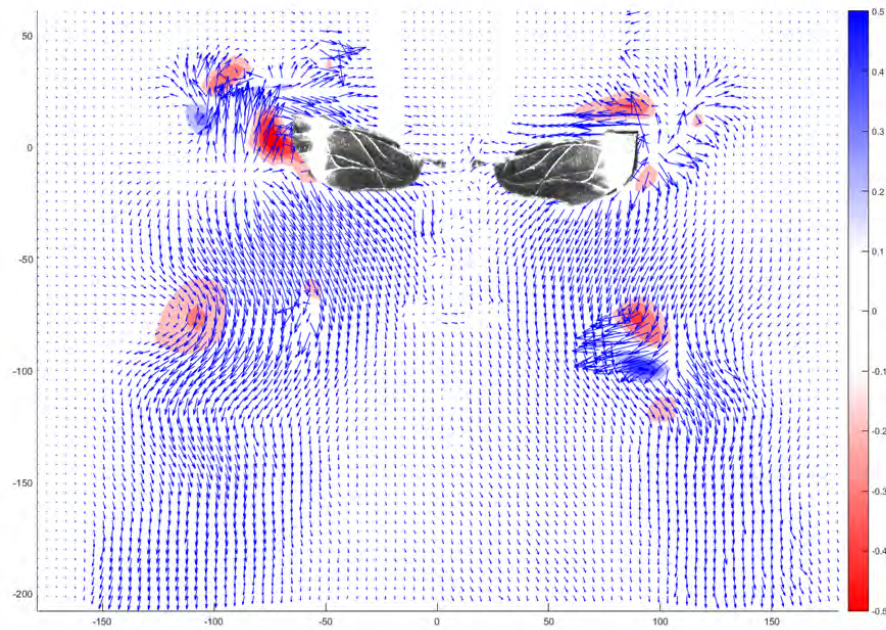


Figure 5.28: PIV 30° in 120 Amplitude Vorticity

time-step there are two vortices below the wings. Flow is strong in the down direction indicating remaining flow field from the previous flapping cycle as seen in the previous measurements for 180 and 150 degree mechanisms.

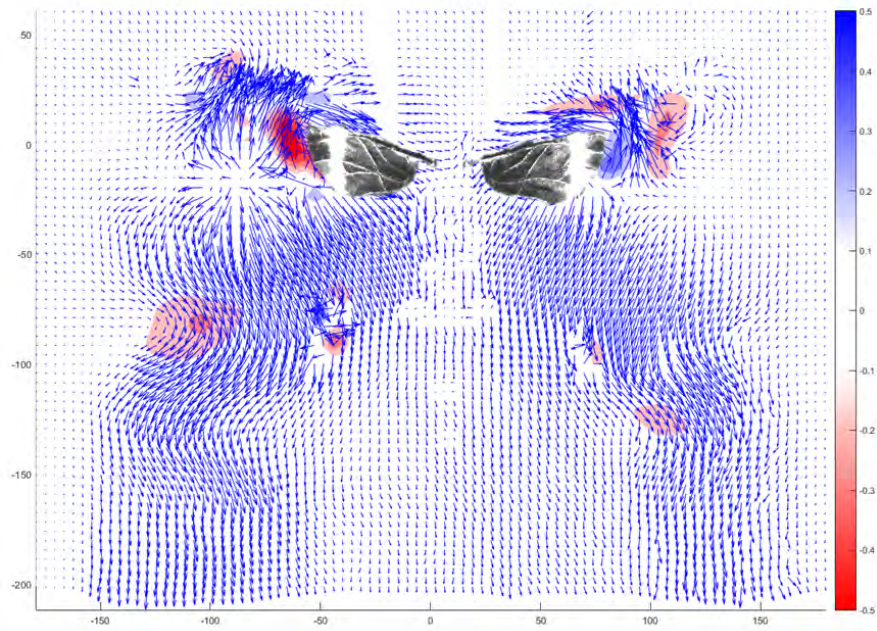


Figure 5.29: PIV 15° in 120 Amplitude Vorticity

As the wings come closer to one another the flow field begins to come into view. Significant flow is occurring near both wings and is possibly traveling over the leading edge of each wing.

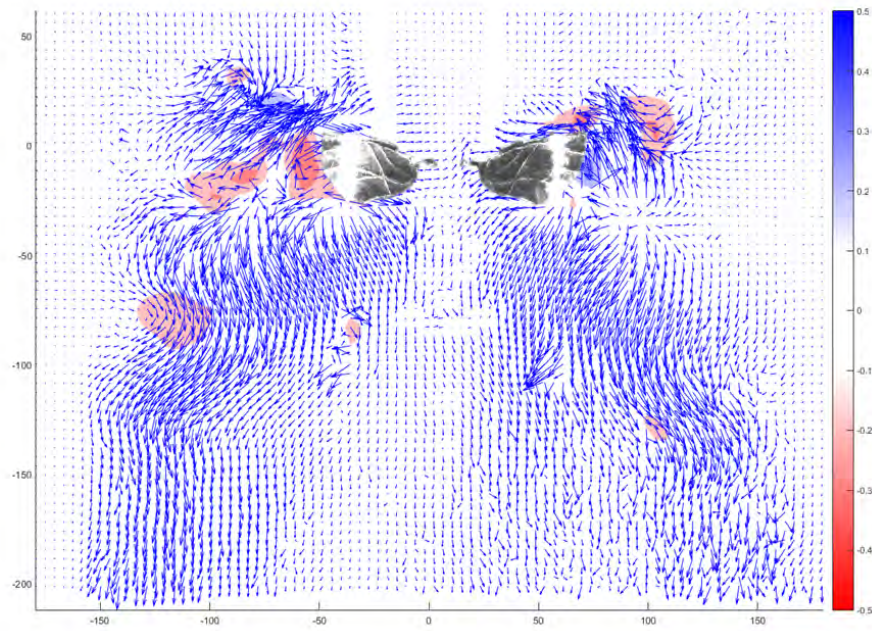


Figure 5.30: PIV 0° in 120 Amplitude Vorticity

Flow in Figure 5.30 is increasingly strong near the left wing. The general 2D flow pattern is strong towards the leading edge and possibly even above the leading edge. Strong flows maintain relative separation below the vehicle.

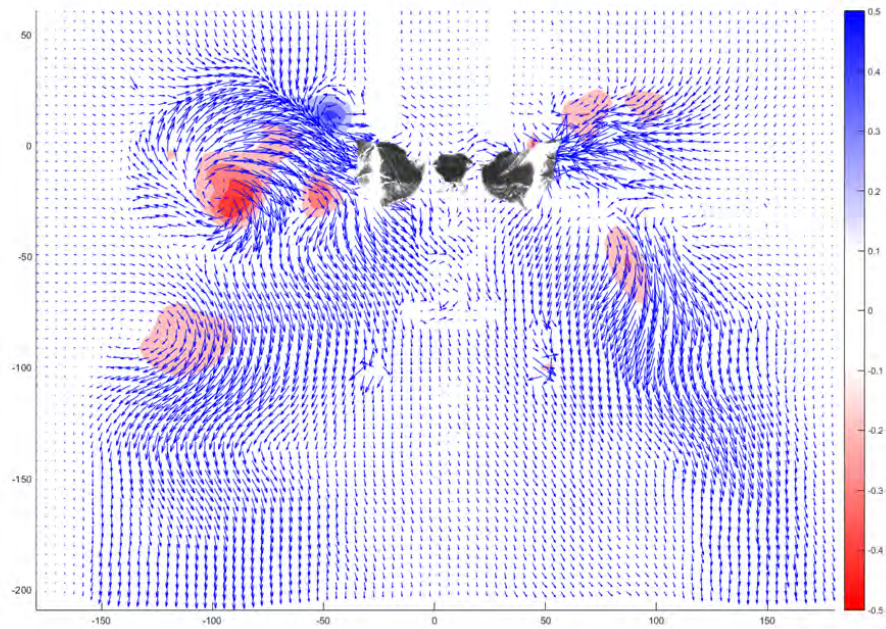


Figure 5.31: PIV 0° out 120 Amplitude Vorticity

A large vortex comes into the 2D measurement in Figure 5.31. No longer does the flow field appear to be moving past the leading edge of the wing but directly into the wing itself. The vortex direction indicates a trailing edge vortex from the previous half stroke. The left wing is capturing a vortex while the right wing appears to primarily be capturing the wake of the previous stroke.

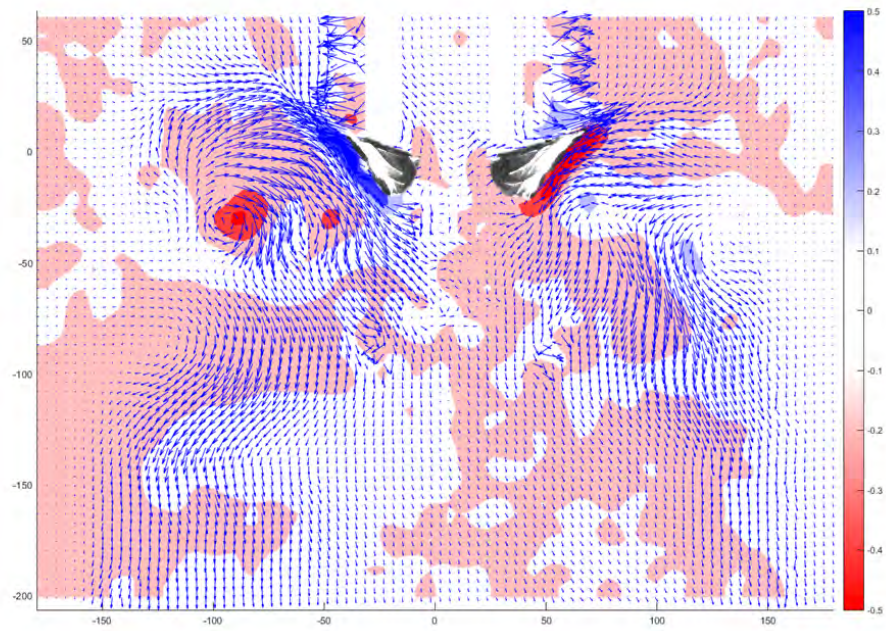


Figure 5.32: PIV 15° out 120 Amplitude Vorticity

Figure 5.32 shows the wings as they begin to move out into the next stroke. The vortex is captured by the left wing and begins to move downward. The right wing continues to catch the wake of the previous stroke in which a small vortex is present. The left wing is pressing firmly on the vortex and both wings are showing good wing deflections as they begin this stroke.

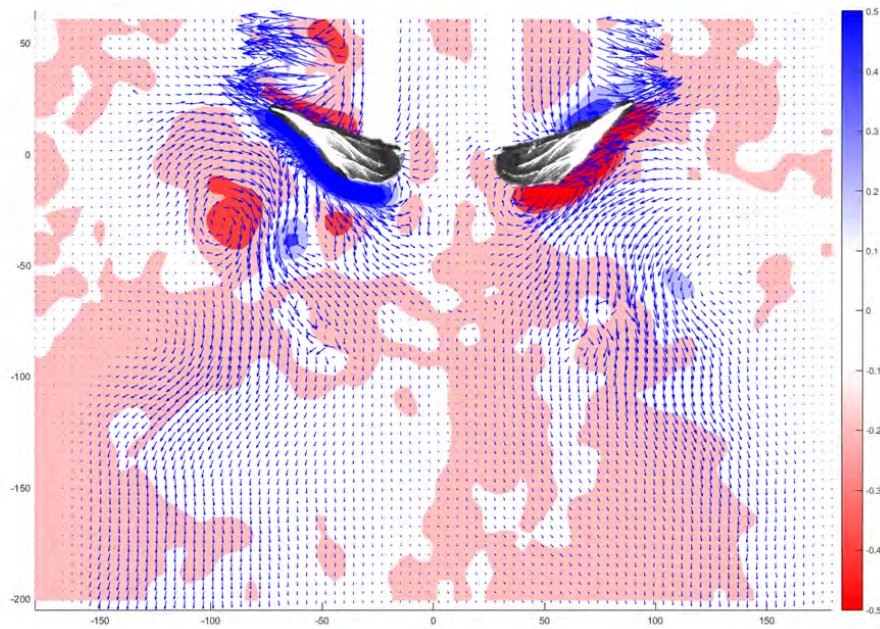


Figure 5.33: PIV 30° out 120 Amplitude Vorticity

The last outward measurement in Figure 5.33 shows the continuing capture of the vortex by the left wing and wake capture by the right wing. The wings are just beginning to generate the trailing edge vortices as they begin the stroke. Inflow from the top of the wings is minimal, but maintains its downward direction. Flow characteristics are similar for all three amplitudes even though a strong vortex was not measured as being captured on the 150 degree amplitude mechanism. The y direction flows give some insight into the general down-wash characteristics and flow interactions between the left and right wings. The absence of a strong right wing vortex is possibly due to a mechanism or wing imbalance. The mechanism had to be disassembled to change the flapping amplitude, lending toward a potential subtle difference with the wings themselves. In addition to the vorticity plots, the Y-velocity was contour plotted to look for differences due to the amplitude change. The following figures discuss this data.

Figure 5.34 shows all six plots on a single page to visualize the progression of flow.

The large arrows represent general flow patterns.

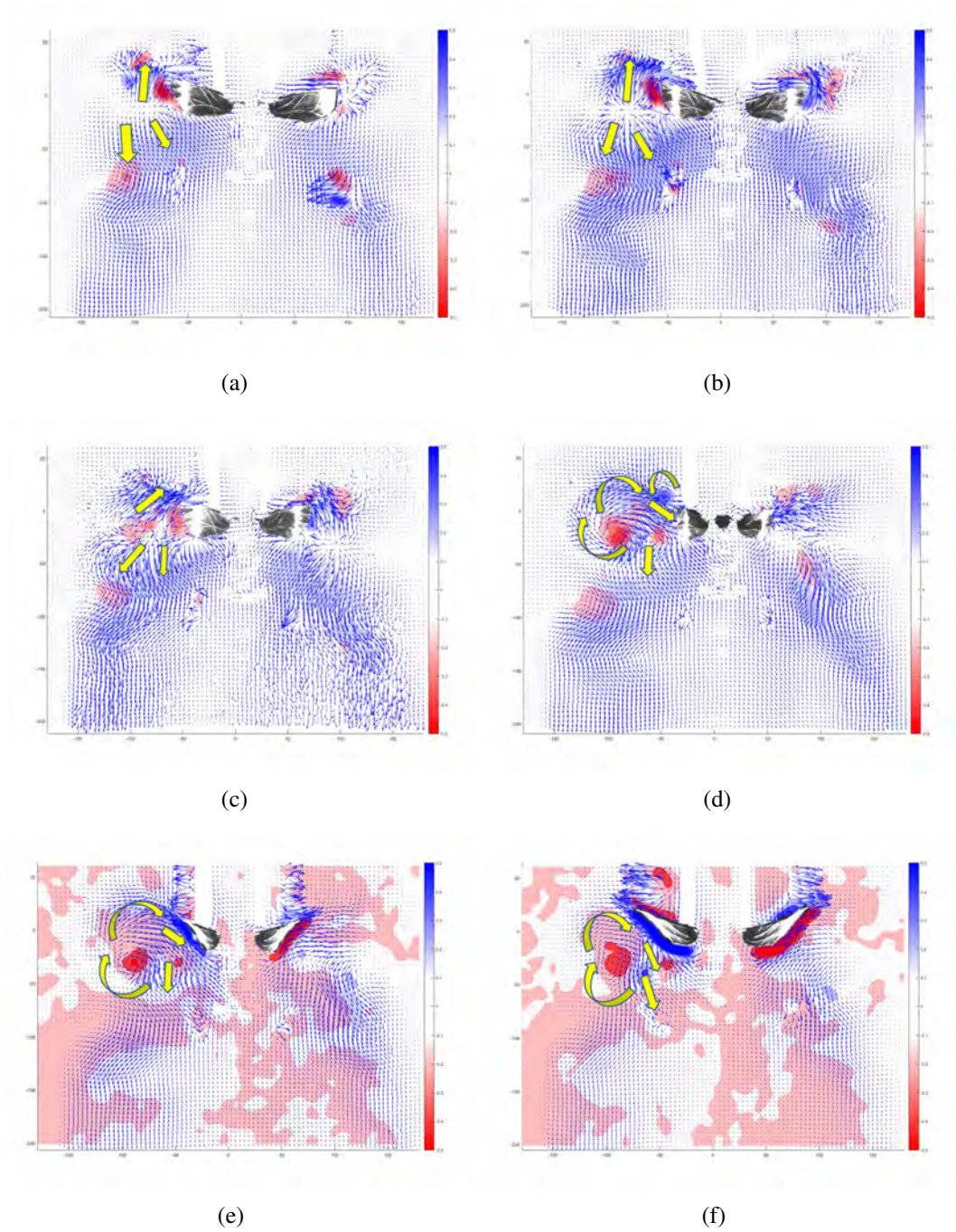


Figure 5.34: PIV 120 Amplitude Quiver Plot

The velocity scale ranges from -5 to +5 meters per second (m/s) for both the y and x velocity plots in Figures 5.35 through 5.37 and Figures A.6 through A.8. The x direction

velocity plots can be found in Appendix A. Red denotes down-flow and blue up-flow, velocities having a magnitude less than 1 m/s are left white for the y and x direction velocities. At a constant velocity, a single particle could traverse the vertical direction of the plot in one full cycle if it were traveling at 3 m/s for the 180 degree amplitude flapping at 11 Hz, 3.6 m/s for the 150 degree at 13.2 Hz and 4.5 m/s for the 120 degree at 16.5 Hz.

Figure 5.35 plots the y velocity of the flow through the wing reversal of the 180 degree amplitude. The 180 amplitude flow has little separation between the flows that is believed to be a result of measurement error from mechanism reflections. The flow is dissipating from Figure 5.35(a) until Figure 5.35(d). As the wing begins to move on the next stroke the flow field grows stronger through the remaining measurements. The lower end of the measurement may be coming from the vehicle side of the measurement plane. 150 amplitude has the least downward flow. Although the lift was the same as the 180 degree mechanism, less flow is measured at the wing reversal. This could be a result of missing the vortex capture or poor coupling for wing inertial and aerodynamic forces for the given frequency. Furthermore, the flow between the wings is separated most for the 120 amplitude compared with the 150 and 180 amplitude mechanisms and the 150 amplitude is separated more than the 180 amplitude that has flow interactions between the wings. Gaps between the flows are incorrect due to the mechanisms reflections and poor contrast for the PIV processor.

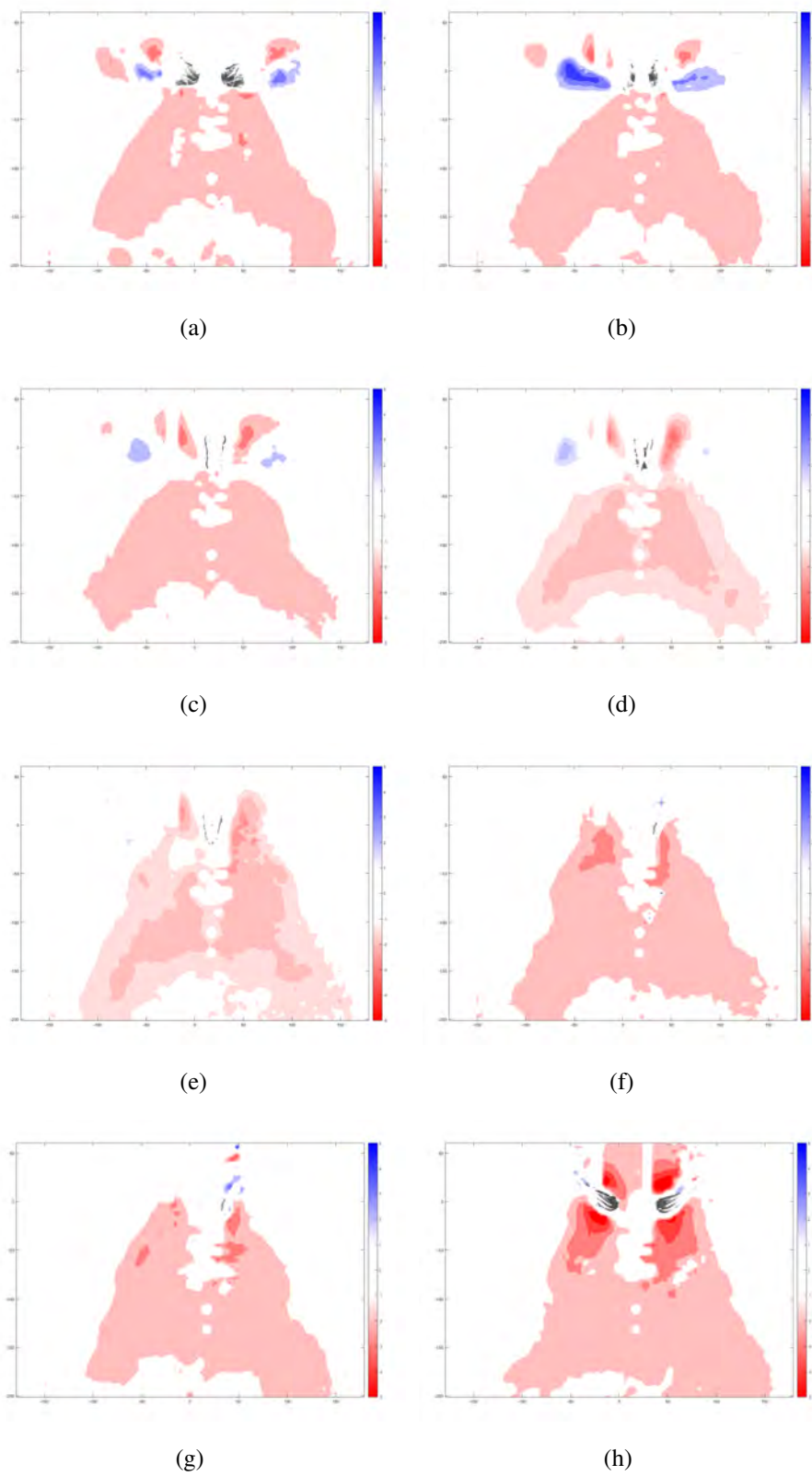
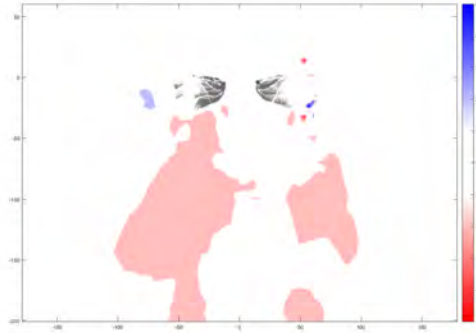
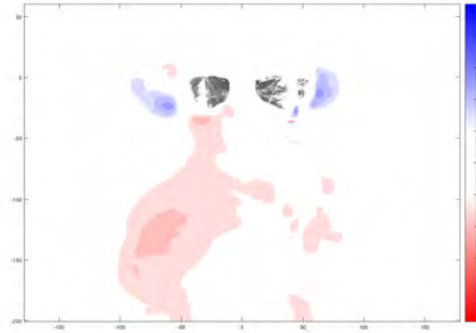


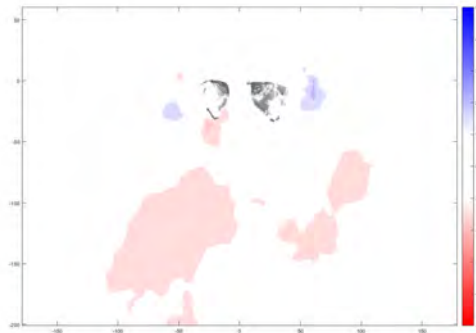
Figure 5.35: PIV 180 Amplitude Y Velocity



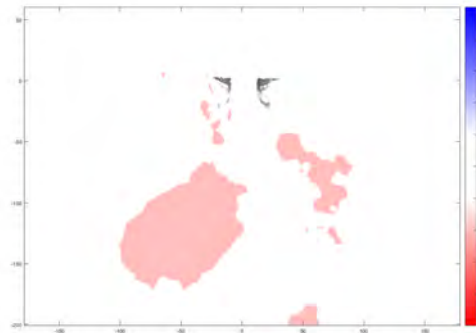
(a)



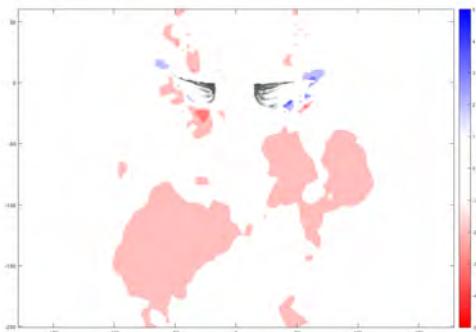
(b)



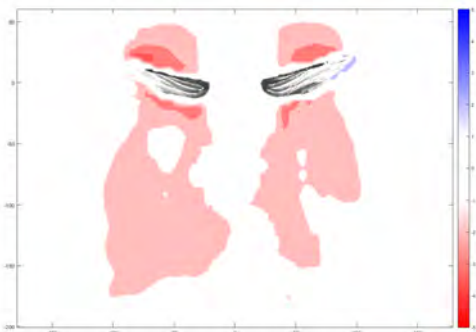
(c)



(d)

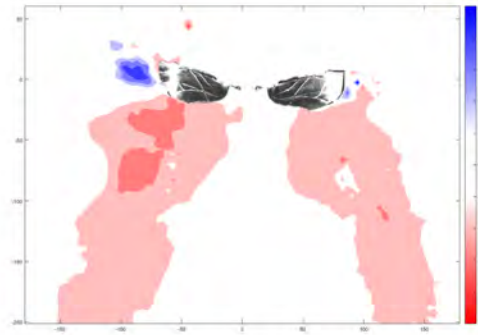


(e)

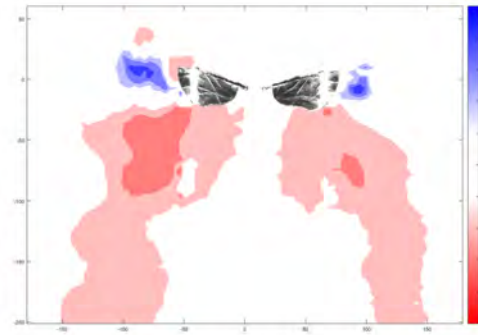


(f)

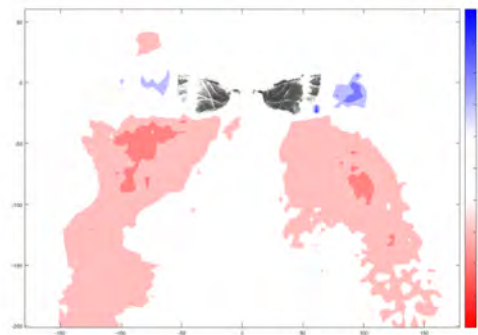
Figure 5.36: PIV 150 Amplitude Y Velocity



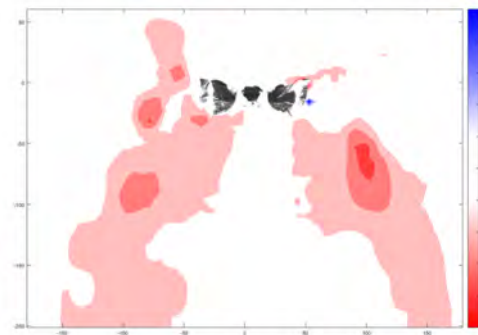
(a)



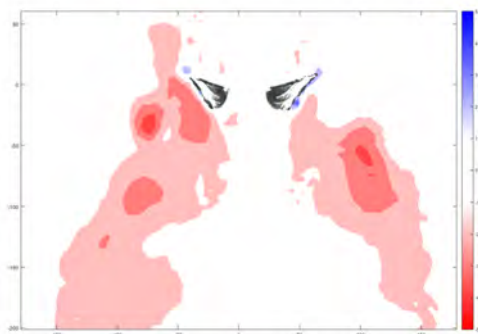
(b)



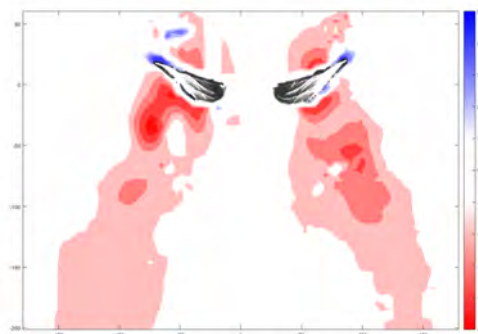
(c)



(d)



(e)



(f)

Figure 5.37: PIV 120 Amplitude Y Velocity

The general assumption of the flow field generated by the fling mechanism is that a low pressure is generated by the wings rapidly opening from one another generating an inflow between the wings. During this time lift is produced and circulation is generated around the leading edge of the wing essentially preparing the flow field for the next stroke. While the results do point to certain signs of such flow patterns, they are far from dominant. Very little flow is generated above any of the wings for all of the wing amplitudes tested. All flapping amplitudes show large down-flow when the left and right vortices combine. The advantage of the 180 degree mechanism is the angle at which the two flows interact. The closer the wings come to one another, the more direct the flows will interact and the stronger the interaction will be. The flow field for the 180 degree amplitude shows relatively homogeneous flow from both sides of the vehicle as evident in Figure 5.35. Possibly the most novel effect that can be seen in the data is the presence of a vorticity that is rotating into the wing. The direction of this vortex indicates that it was shed from the trailing edge of the wing. The 120 mechanism shows the vortex clearly after the wing has stopped its dwell in Figure 5.31. The vortex is not present in the 75% span of the wing until the wing has stopped the previous stroke. Presumably the vortex is shed from the inner span and is not seen in the measurement until this point but it is also possible that the vortex is not formed until this point. A second smaller vortex can be seen in the opposite direction that is being formed around the leading edge for both the 120 and 180 mechanisms indicating that wing interaction is not the reason for either vortex. The complete origin of this vortex will require more locations of PIV testing, possibly to include the use of 3D PIV methods.

Mid-Stroke Measurements

In addition to the end of stroke measurements, three mid-stroke measurements were made to evaluate changes in performance where the flows should be similar for each flapping amplitude. The wing velocity at the mid-stroke using idealized kinematics are equal. Figure 5.38 shows the raw images of the wing locations. All scales are equal for vorticity intensity plots. Scales for Y and X velocities are also made equal across all wing amplitudes. X velocity plots can be found in Appendix A.

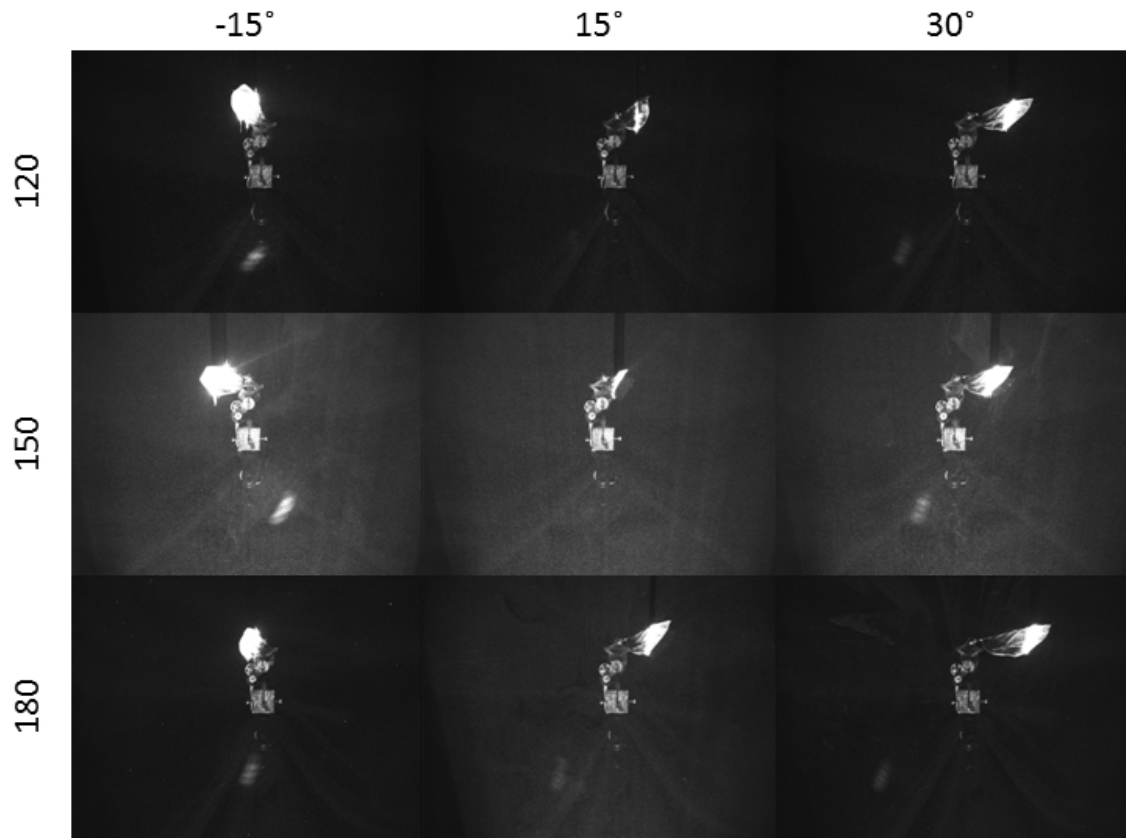


Figure 5.38: Wing Positions at Mid-Stroke

All three flapping amplitudes map flow strongest trailing the wing. A large flow in the y direction is present leading the wing in both the 180 and 150 amplitude flapping strokes found in Figures 5.42 and 5.43. The flow leading the wing appears to be remnant from the previous flapping stroke as large amounts of flow are still present throughout the viewing area.

The measurement being planar shows some of the story occurring at the midstroke of the flow. There is a vortex that appears to be shed by the trailing edge. Why this is shed just before the midstroke cannot be determined. It is possible that this vortex was strengthened by the wake capture which disappears as the wing continues through its stroke. It is possible that the measurement cannot detect the vortex as it rotates with the wing and becomes less normal to the measurement plane. A more comprehensive PIV measurement, whether more

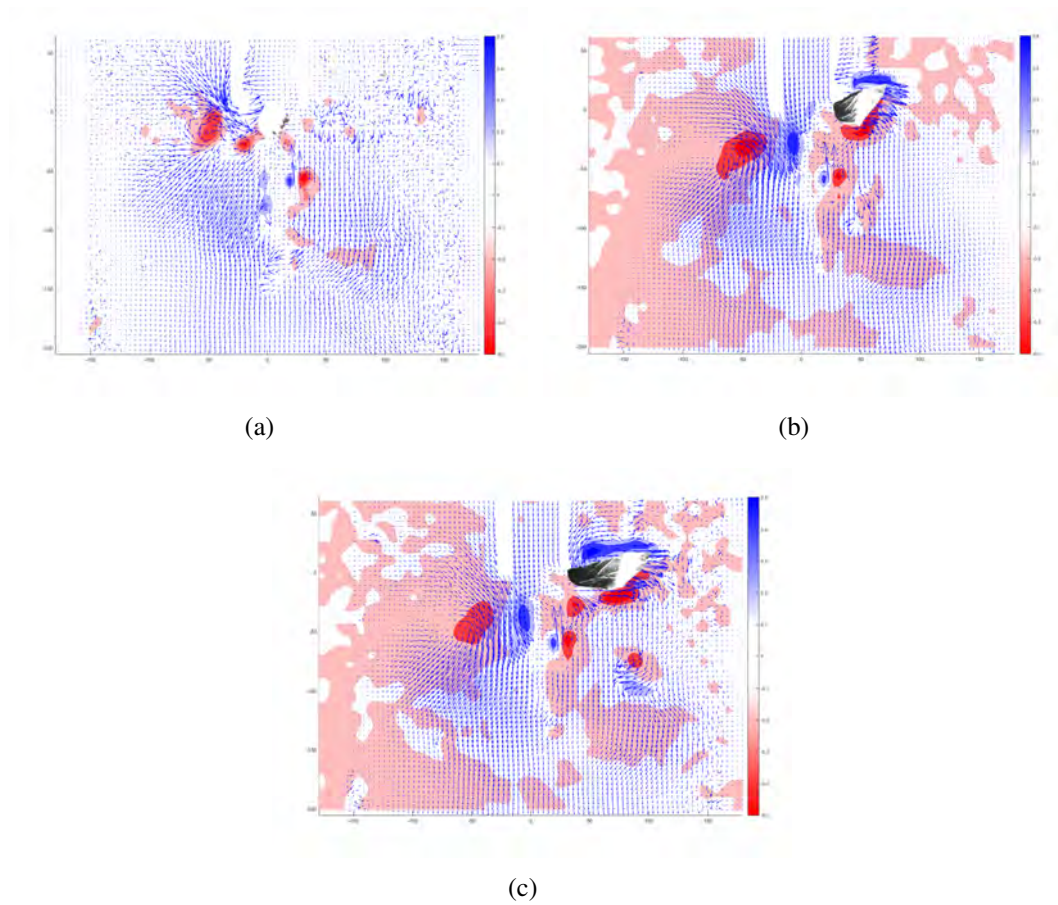


Figure 5.39: PIV Mid-Stroke 180 Amplitude Vorticity

plane locations or 3D PIV, would be necessary to understand what flow phenomena is occurring.

The 150 degree measurements show similar flow patterns to the 180 degree at mid-stroke. Strong downward flow is prevalent with the trailing edge vortex staying near the middle left of the measurement through the three measurements.

The 120 degree measurements have two distinct vortices present. The first is the same direction as the previous two amplitudes, however, an additional vortex rotating in the opposite direction is also present. Both meet near the midstroke and dissipate as the wing travels. Even though the wings are traveling at the same average velocity, the 120 degree amplitude has 50% shorter flapping cycles than the 180 degree amplitude. The flow field from the previous stroke has 50% less time to dissipate and may have more interaction

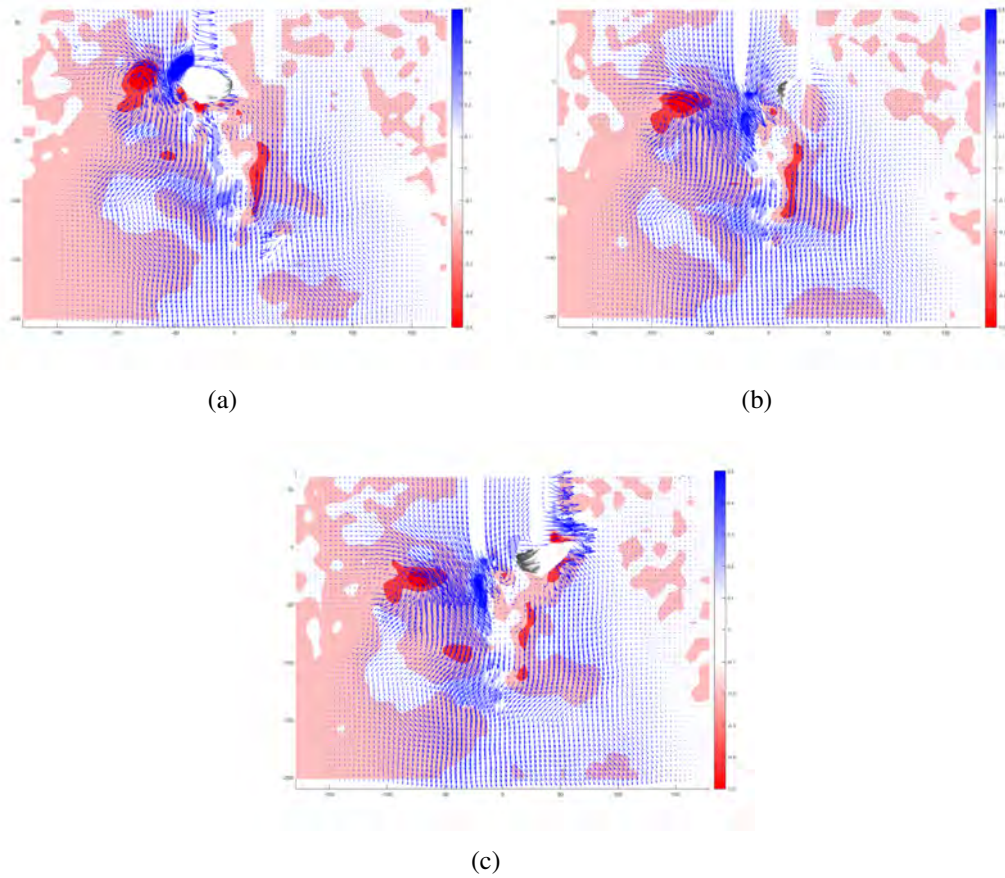


Figure 5.40: PIV Mid-Stroke 150 Amplitude Vorticity

during the midstrokes.

The y velocity plots for the midstroke show flow in the downward direction across the most plane measured for all measurements. This indicates that a general down-flow pattern is induced during flapping. The flapping frequency is fast enough that flow effects from the previous stroke is still effecting the current stroke. While not a groundbreaking observation, it is certainly confirmed by the data. In general the flow field is greater than 1 m/s during the measurements which would remain in the measurement field well into the next stroke for all flapping amplitudes.

The 180 degree flapping amplitude has a large measuement in front of the wing which dissipates through the measurements while trailing the wing grows a larger downward velocity as the wing passes through.

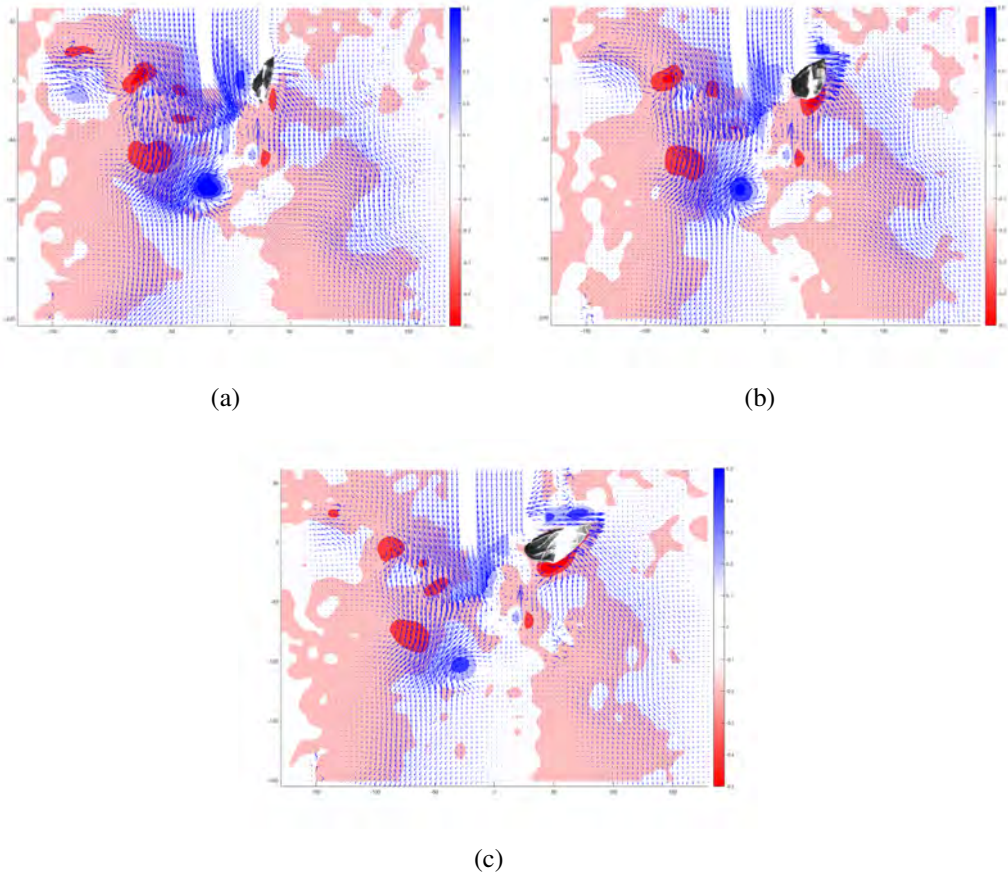
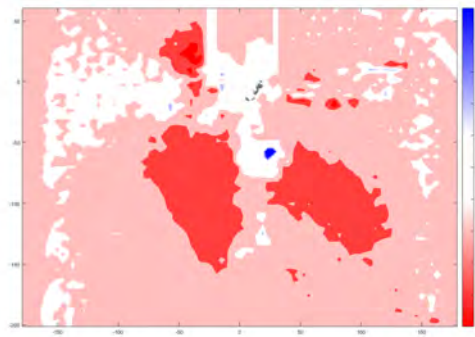


Figure 5.41: PIV Mid-Stroke 120 Amplitude Vorticity

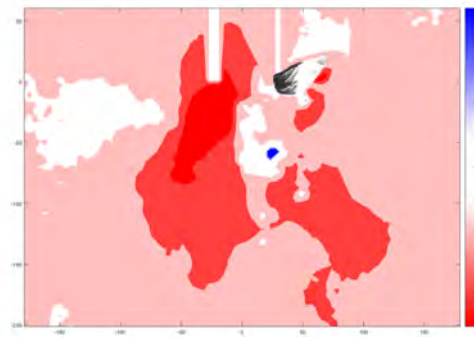
The 150 degree flapping amplitude has a larger area of stronger flow but does not show as widespread of flow as the 180 and 120 degree flapping amplitudes.

The 120 degree flapping amplitude has a widespread velocity field over 1 m/s similar to the 180 degree plots. Strong flows trailing the wing are similar to the 180 but the flow in front of the wing does not appear as strong. Without further measurements the interactions are difficult to judge.

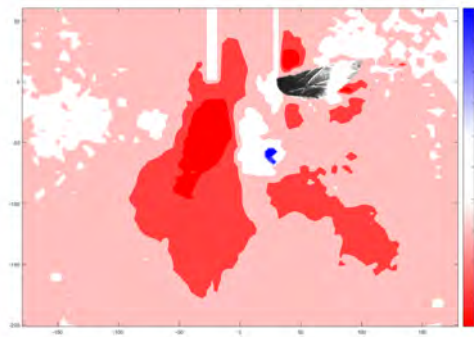
The X velocity plots corresponding to the midstroke measurements can be found in Appendix A in Figures A.9 through A.11.



(a)

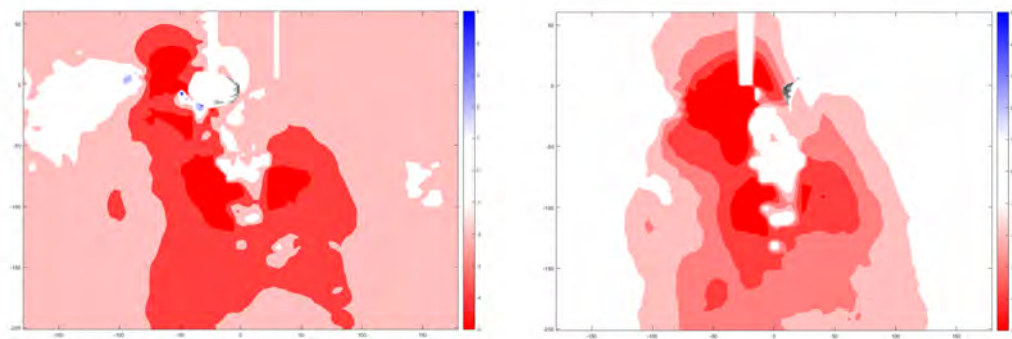


(b)



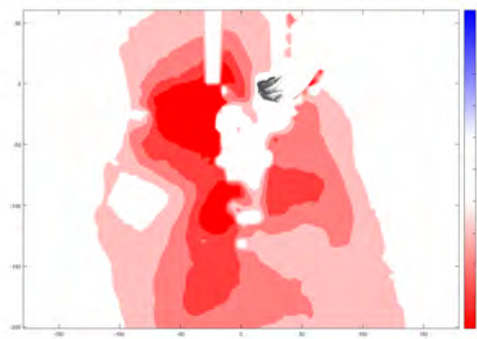
(c)

Figure 5.42: PIV Mid-Stroke 180 Amplitude Y Velocity



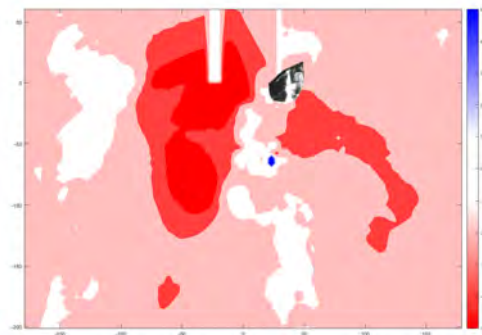
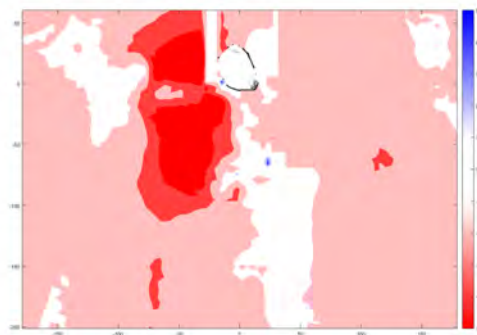
(a)

(b)



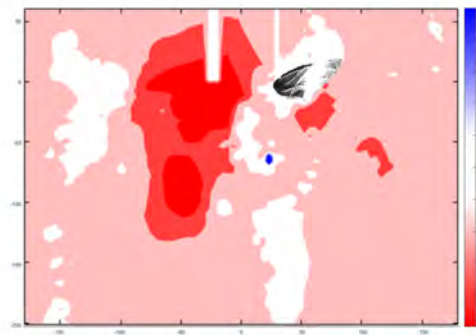
(c)

Figure 5.43: PIV Mid-Stroke 150 Amplitude Y Velocity



(a)

(b)



(c)

Figure 5.44: PIV Mid-Stroke 120 Amplitude Y Velocity

5.3.3 Experimental Conclusions

Flapping wing micro aerial vehicles are highly dynamic from the vehicles to the wings. The wings may be the most difficult problem for MAV designers from repeatability to good performance. The couple between the wing stiffness to its own mass and fluid interactions generates deflections that are difficult to measure much less accurately predict with analysis. Wing iteration, lift testing and flow measurement are the stepping stones to understanding the flow fields and resulting lift enhancements due to wing interactions and wake interactions. Reaching the theoretical maximum lift wing angle of attack of 45 degrees and a greater velocity will not guarantee the greatest lift and will most certainly not achieve a good flapping efficiency. The data presented suggests that the wake capture may be the single most important feature for a flapping wing vehicle. Without the induced flow of the previous stroke the wings would perform more similarly to conventional aerodynamics. In addition to the capturing the wake of the previous stroke, data shows that in two specific cases what appears to be a trailing edge vortex is captured. The capture of the vortex may provide an even greater lift enhancement, utilizing the stability of the vortex to gain extra lift. The data gathered, particularly the PIV flow measurements, suggest an enhancement to wake capture of trailing edge vortex capture.

CONCLUSION

Flapping wing aerodynamics have been of interest to humans for as long as we have seen the fruit fly flying around our apple to the eagles flying majestically through the skies. While the bird-like fliers are largely understood and have been replicated in many instances, bridging the gap to insect fliers has proven difficult. Low Reynolds numbers, light weight and dynamic interactions have proven to be complex and hard to predict, measure and understand. The desire of flapping wing micro air vehicles is to learn from nature and develop vehicles capable of sustained flight, control and maneuverability to provide access to areas too small, dangerous, or obvious for the user. Many options are available for their manufacture and will typically require several methods to make an efficient, robust vehicle. The advances in additive manufacturing have provided the perfect means for cheap and fast turnaround for parts due to the size of FWMAVs. As this technology matures, it will surely provide even better tools for MAV designers to provide more strength, better turnaround time and better repeatability. An advancement that provides additive manufacturing for wings may be the single most useful machine for researchers as designs could be modified precisely and repeatably. Repeatably wings are necessary for learning more about flow fields and interactions under highly dynamic conditions. Designing a mechanism to minimize quick return and maximize flapping amplitude is the first step toward a successful vehicle. Minimizing the cycle averaged acceleration by increasing flapping amplitude will generate more lift for less motor effort. Control methods for FWMAVs typically are done by three methods, manipulating the wing at an additional point, manipulating the amplitude and bias of the flapping stroke or manipulating the wing velocity through the stroke. The design of a robust, flexible wing is necessary to capture the added aerodynamic effects typically associated with insect fliers. Experimental testing is key to determining lift curves

for wings and mechanisms. PIV testing can be used to capture the flow fields and high speed imagery can be used to capture wing shapes.

6.1 Research Contributions

FWMAV require extensive amounts of experience designing, building and testing to create desirable vehicles for research and flight. This experience cannot be translated through a paper, however, several lessons have been learned and can be utilized for future work. The first is the general tools that are desirable for MAV manufacture from AM to milling and turning parts. When using a four bar mechanism to drive the wings, an amplification method must be used to avoid the quick return inherent to this drive style. A large angle four bar mechanism will generate too large of stroke imbalance causing very detrimental effects on the mechanism, wings and flow fields. Large flapping amplitudes drive the cycle averaged wing acceleration down for a given cycle averaged velocity, directly correlating to either the ability to achieve greater cycle averaged velocity or less motor effort for similar lift values. Wing design and manufacture is the most important and difficult problem to solve for FWMAVs. Subtle differences in wings can cause significant differences in lift capability and efficiency. The method demonstrated in this paper does provide wings sufficiently strong to withstand repeated cycling and desired strain levels to achieve large deflections. Wake capture is a significant contributor to the lift enhancing mechanisms. Most notably, the trailing edge vortex can be captured under the correct conditions. The impinging vortex on the wing upon reversal may provide the significant lift increase not explainable by conventional aerodynamics. The data collected does show clap and fling flow effects, but does not indicate significant flows and potential lift enhancements relative to the wake capture found in all three flapping amplitudes. Performance benefit for large flapping amplitudes appears to be consistent with the reduction in cycle averaged acceleration allowing a more efficient flapping cycle.

6.2 Recommendations for Future Work

Although great strides were made in development of mechanisms and wings, several different areas require further research to push the technologies further and understand the specific aerodynamic effects. As the COTS items continue to be made smaller, more efficient and more functional, the FWMAV designer will have an easier time producing the lift to weight ratios to provide flight and extend flight time. Developments in battery technology, motors, and electronics are the largest drivers for these specifications that are crucial for a deployable FWMAV. The massive research effort that has many unknowns is the aerodynamics associated with the dynamic nature of FWMAVs and insects. Data captured by PIV shows flow phenomena, namely trailing edge wake capture, occurring at wing reversal that has not been found in literature. This phenomena may be a result of the aerodynamic and inertial coupling that occurs with a flexible wing. More data covering larger ranges and preferably 3D PIV could be very useful in determining the extent of this effect and its potential lift enhancing capability. Interesting flows occur during the mid-stroke as well indicating that unsteady effects could effect more than just wing reversal. Efforts must first be put into developing wings which can withstand the extreme forces and fatigue cycles that plague them. Repeatability in the manufacture of wings is crucial to the advancement of understanding the phenomena found in flapping wing flight. Additive manufacturing may provide the repeatability needed to provide the researchers and engineers the ability to pass on designs and results to others for further investigation and testing. Solving these issues can lead to flow measurements that will explain the aerodynamic phenomena that give flapping wings the potential edge on conventional rotor-craft.

Bibliography

- [1] “AFRL Strategic Vision,” *Air Force Research Laboratory*, 31 July 2007.
- [2] Mueller, T. J., *Fixed and Flapping Wing Aerodynamics for Micro Air Vehicle Applications*, Vol. 195, AIAA, 2001.
- [3] Barut, A., Das, M., and Madenci, E., “Nonlinear Deformations of Flapping Wings on a Micro Air Vehicle,” *47th AIAA/ASME/ASCE/AHS/ASC Structures, Structural Dynamics, and Materials Conference*, AIAA 2006-1662, May 2006.
- [4] *Micro Flier Radio*, www.microflierradio.com (accessed 12/9/16).
- [5] *ParkZone Vapor BNF*, www.parkzone.com/Products/Default.aspx?ProdID=PKZ3380 (accessed 12/9/16).
- [6] Zufferey, J., Klapotocz, A., Beyeler, A., Nicoud, J., and Floreano, D., “A 10-gram Microflyer for Vision-based Indoor Navigation,” *Intelligent Robots and Systems*, IEEE 3267-3272, October 2006.
- [7] *Blade Scout CX RTF 3-Ch Heli*, <http://www.bladehelis.com/Products/Default.aspx?ProdID=BLH2700> (accessed 12/9/16).
- [8] *Air Hogs Pocket Copter*, <http://www.rcmania.com/air-hogs-pocket-copter/> (accessed 12/9/16).
- [9] *University of Pennsylvania GRASP Website*, <https://www.grasp.upenn.edu/> (accessed 12/9/16).

- [10] *Robot Quadrotors Perform James Bond Theme*, http://www.youtube.com/watch?v=_sUeGC-8dyk (accessed 12/9/16).
- [11] *Raffaello D'Andrea*, <http://raffaello.name/projects/flying-machine-arena/> (accessed 12/9/16).
- [12] *Raffaello D'Andrea: The astounding athletic power of quadcopters*, <http://www.youtube.com/watch?v=w2itwFJCgFQ> (accessed 12/9/16).
- [13] *AR Parrot Drone*, <http://cheesycam.com/parrot-ar-drone-video-equipped-remote-quadricopter/> (accessed 12/9/16).
- [14] *Blade Nano QX*, <http://www.bladehelis.com/Products/Default.aspx?ProdID=BLH7680> (accessed 12/9/16).
- [15] *AR Parrot Drone 2.0*, <http://ardrone2.parrot.com/> (accessed 11/12/13).
- [16] Hsu, C., Evans, J., Vytla, S., and Huang, P. G., "Development of Flapping Wing Micro Air Vehicles - Design, CFD, Experiment and Actual Flight," *48th AIAA Aerospace Science Meeting*, AIAA-2010-1018, January 2010.
- [17] "Delfly Demonstration Videos," www.delfly.nl, Delft University of Technology.
- [18] Mueller, D., Bruck, H. A., and Gupta, S. K., "Measurement of Thrust and Lift Forces Associated With Drag of Compliant Flapping Wing for Micro Air Vehicles Using a New Test Stand Design," *Experimental Mechanics*, Vol. 50, No. 6, 2010, pp. 725–735, ID: 00144851/v50i0006/725_motalfuantsd.
- [19] Tan, X., Zhang, W., Ke, X., Chen, W., Zou, C., Liu, W., Cui, F., and Wu, X., "Development of Flapping-wing Micro Air Vehicle in Asia," *Proceedings of the 10th World Congress on Intelligent Control and Automation*, IEEE, July 2012, pp. 3939–3942.
- [20] Ang, H., Xiao, T., and Duan, W., "Flight Mechanism and Design of Biomimetic Micro Air Vehicles," *Science in China Series E: Technological Sciences*, Vol. 52(12), 2009, pp. 3722–3728.

- [21] Fenelon, M. A. and Furukawa, T., “Design of an Active Flapping Wing Mechanism and a Micro Aerial Vehicle using a Rotary Actuator,” *Mechanism and Machine Theory*, Vol. 45, No. 2, 2010, pp. 137–146, ID: 0094114x/v45i0002/137_doaafwavuara.
- [22] Pornsinsirak, T., Tai, Y. C., Nassef, H., and Ho, C. M., “Titanium-alloy MEMS wing technology for a micro aerial vehicle application,” *Sensors and Actuators A: Physical*, Vol. 89, No. 1-2, 2001, pp. 95–103, ID: 09244247/v89i1-2/95_tmwtfamava.
- [23] Mazaheri, K. and Ebrahimi, A., “Experimental Investigation of the Effect of Chord-wise Flexibility on the Aerodynamics of Flapping Wings in Hovering Flight,” *Journal of Fluids and Structures*, Vol. 26, No. 4, 2010, pp. 544–558, ID: 08899746/v26i0004/544_eioteoofwihf.
- [24] Mazaheri, K. and Ebrahimi, A., “Experimental Study on Interaction of Aerodynamics with Flexible Wings of Flapping Vehicles in Hovering and Cruise Flight,” *Archive of Applied Mechanics*, Vol. 80, No. 11, 2010, pp. 1255–1269, ID: 09391533/v80i0011/1255_esoioavihacf.
- [25] Galiński, C. and Żbikowski, R., “Insect-like Flapping Wing Mechanism Based on a Double Spherical Scotch Yoke,” *Journal of The Royal Society Interface*, Vol. 2, No. 3, 2005, pp. 223–235, ID: 17425689/v02i0003/223_ifwmboadssy.
- [26] Galiński, C. and Żbikowski, R., “Materials Challenges in the Design of an Insect-Like Flapping Wing Mechanism Based on a Four-Bar Linkage,” *Materials and Design*, Vol. 28, No. 3, 2007, pp. 783–796, ID: 02613069/v28i0003/783_mcitdomboaf.
- [27] Hu, H., Kumar, A. G., Abate, G., and Albertani, R., “An Experimental Investigation on the Aerodynamic Performances of Flexible Membrane Wings in Flapping Flight,” *Aerospace Science and Technology*, Vol. 14, No. 8, 2010, pp. 575–586, ID: 12709638/v14i0008/575_aeiotafmwiff.
- [28] Peng, S., Chen, W., and Zhang, W., “Co-simulation and experimental study for wingspan of flapping wing micro aerial vehicle,” *Journal of Shang-*

- hai Jiaotong University (Science), Vol. 14, No. 2, 2009, pp. 252–256, ID: 10071172/v14i0002/252_caesfwofwmav.
- [29] Yang, W., Song, B., Song, W., and Wang, L., “The Effects of Span-Wise and Chord-Wise Flexibility on the Aerodynamic Performance of Micro Flapping-Wing,” *Chinese Science Bulletin*, Vol. 57, No. 22, 2012, pp. 2887–2897, ID: 10016538/v57i0022/2887_teosactapomf.
- [30] Keenon, M., Klingebiel, K., and Won, H., “Development of the Nano Hummingbird: A Tailless Flapping Wing Micro Air Vehicle,” *50th AIAA Aerospace Sciences Meeting*, AIAA 2012-0588, January 2012.
- [31] Dickinson, M. H., Lehmann, F., and Sane, S. P., “Wing Rotation and the Aerodynamic Basis of Insect Flight,” *Science*, Vol. 284, No. 5422, June 1999, pp. 1954–1960.
- [32] Wood, R. J., Steltz, E., and Fearing, R. S., “Optimal Energy Density Piezoelectric Bending Actuators,” *Sensors and Actuators A: Physical*, Vol. 119, 2005, pp. 476–488.
- [33] Wood, R. J., “The First Takeoff of a Biologically Inspired At-Scale Robotic Insect,” *IEEE Transactions on Robotics*, Vol. 24, No. 2, 2007, pp. 341–347.
- [34] Wood, R. J., “Fly, Robot Fly,” *IEEE Spectrum*, March 2008, pp. 25–29.
- [35] Wood, R. J., “The First Takeoff of a Biologically Inspired At-Scale Robotic Insect,” *IEEE Transactions on Robotics*, Vol. 24, No. 2, April 2008, pp. 341–347.
- [36] Arabagi, V., Hines, L., and Sitti, M., “Design and Manufacturing of a Controllable Miniature Flapping Wing Robotic Platform,” *The International Journal of Robotics Research*, Vol. 31, No. 6, 2012, pp. 785–800, ID: 02783649/v31i0006/785_damoacmfwrp.
- [37] Yoon, S., Kang, L., and Jo, S., “Development of Air Vehicle with Active Flapping and Twisting of Wing,” *Journal of Bionic Engineering*, Vol. 8, No. 1, 2011, pp. 1–9, ID: 16726529/v08i0001/1_doavwafatow.

- [38] Ellington, C. P., “Insect versus Birds: The Great Divide,” *44th AIAA Aerospace Sciences Meeting*, AIAA Paper 2006-35, January 2006.
- [39] Venkata, S. K., *Unsteady Low Reynolds Number Aerodynamics of a Rotating Wing*, Master’s thesis, University of Maryland, 2012.
- [40] Dawson, J. and Huang, P. G., “Figure-8 Flapping Micro Air Vehicle,” *49th AIAA Aerospace Sciences Meeting*, AIAA 2011-551, January 2011.
- [41] “Slow Motion Butterfly in Flight,” *UltraSlo*, www.youtube.com/watch?v=CoInyfsySD0 (accessed 12/9/16).
- [42] Dong, H., Koehler, C., Liang, Z., Wan, H., and Gaston, Z., “An Intergrated Analysis of a Dragonfly in Free Flight,” *28th AIAA Applied Aerodynamics Conference*, AIAA 2010-4390, June 2010.
- [43] Goslow, G. E., Dial, K. P., and Jenkins, F. A., “Bird Flight: Insights and Complications,” *Biological Sciences Faculty Publications*, 1990, pp. 108–115.
- [44] *SmartBird - Bird Flight Deciphered*, <https://www.festo.com/group/en/cms/10238.htm> (accessed 12/9/16).
- [45] Weis-Fogh, T., “Quick Estimates of Flight Fitness in Hovering Animals, Including Novel Mechanisms for Lift Production,” *Journal of Experimental Biology*, Vol. 59, 1973, pp. 169–230.
- [46] Ellington, C. P., “The Novel Aerodynamics of Insect Flight: Applications to Micro Air Vehicles,” *Journal of Experimental Biology*, Vol. 202, 1999, pp. 3439–3448.
- [47] Shyy, W., Aono, H., Chimakurthi, S. K., Trizila, P., Kang, C. K., Cesnik, C. E. S., and Liu, H., “Recent Progress in Flapping Wing Aerodynamics and Aeroelasticity,” *Progress in Aerospace Sciences*, Vol. 46, No. 7, 2010, pp. 284–327, ID: 03760421/v46i0007/284_rpfwaaa.

- [48] Usherwood, J. R. and Ellington, C. P., “The Aerodynamics of Revolving Wings I. Model Hawkmoth Wings,” *Journal of Experimental Biology*, Vol. 205, 2002, pp. 1547–1564.
- [49] Usherwood, J. R. and Ellington, C. P., “The Aerodynamics of Revolving Wings II. Propeller Force Coefficients from Mayfly to Quail,” *Journal of Experimental Biology*, Vol. 205, 2002, pp. 1565–1576.
- [50] DeLuca, A., *Aerodynamic Performance and Particle Image Velocimetry of Piezo Actuated Biomimetic Manduca Sexta Engineered Wings Towards the Design and Application of a Flapping Wing Flight Vehicle*, Ph.D. dissertation, Air Force Institute of Technology, December 2013.
- [51] Smith, T. J., Dawson, J. C., Huang, P. G., and Doman, D. B., “Figure-8 Flapping Micro Air Vehicle,” *29th AIAA Applied Aerodynamics Conference*, AIAA 2011-3792, June 2011.
- [52] Lehmann, F., Sane, S. P., and Dickinson, M., “The Aerodynamic Effects of Wing-Wing Interaction in Flapping Insect Wings,” *Journal of Experimental Biology*, Vol. 208, 2005, pp. 3075–3092.
- [53] Miller, L. A. and Peskin, C. S., “A Computational Fluid Dynamics of “Clap and Fling” in the Smallest Insects,” *Journal of Experimental Biology*, Vol. 208, 2004, pp. 195–212.
- [54] Walker, J. A., “Rotation Lift: Something Different or More of the Same?” *Journal of Experimental Biology*, Vol. 205, 2002, pp. 3783–3792.
- [55] Wan, H., Dong, H., and Gai, K., “Computational Investigation of Cicada Aerodynamics in Forward Flight,” *J. R. Soc. Interface*, Vol. 12, No. 20141116, 2015.
- [56] Broering, T. M. and Lian, Y.-S., “The Effect of Phase Angle and Wing Spacing on Tandem Flapping Wings,” *Acta Mechanica Sinica*, Vol. 28, No. 6, 2012, pp. 1557–1571, ID: 05677718/v28i0006/1557_teopaawsotfw.

- [57] Dileo, C. and Deng, X., “Design of and Experiments on a Dragonfly-Inspired Robot,” *Advanced Robotics*, Vol. 23, No. 7-8, 2009, pp. 1003–1021, ID: 01691864/v23i7-8/1003_doeoadr.
- [58] Combes, S. A. and Daniel, T. L., “Into Thin Air: Contributions of Aerodynamic and Inertial-Elastic Forces to Wing Bending in the Hawkmoth *Manduca Sexta*,” *Journal of Experimental Biology*, Vol. 206, May 2003, pp. 2999–3006.
- [59] Combes, S. A. and Daniel, T. L., “Flexural Stiffness in Insect W Wing I. Scaling and the Influence of Wing Venation,” *Journal of Experimental Biology*, Vol. 206, June 2003, pp. 2979–2987.
- [60] Combes, S. A. and Daniel, T. L., “Flexural Stiffness in Insect W Wing II. Spatial Distribution and Dynamic Wing Bending,” *Journal of Experimental Biology*, Vol. 206, June 2003, pp. 2989–2997.
- [61] Yin, B. and Luo, H., “Effect of Wing Inertia on Hovering Performance of Flexible Flapping Wings,” *Physics of Fluids*, Vol. 22, No. 11, 2010, pp. 111902–111902, ID: 10706631/v22i0011/111902_eowiohpoffw.
- [62] Doman, D. B. and Regisford, S., “Wing Sizing, Trim, and Control Consideration in the Design of Hover-Capable Flapping Wing Micro Air Vehicles,” AIAA Paper 2010-7629, Aug. 2010.
- [63] Orłowski, C. T., *Flapping Wing Micro Air Vehicles: An Analysis of the Importance of the Mass of the Wings to Flight Dynamics, Stability, and Control*, Ph.D. dissertation, The University of Michigan, 2011.
- [64] O’Hara, R. P., *The Characterization of Material Properties and Structural Dynamics of the Manduca Sexta Forewing for Application to Flapping Wing Micro Air Vehicle Design*, Ph.D. dissertation, Air Force Institute of Technology, September 2012.
- [65] Hu, Z. and Deng, X., “Design and Performance of Insect Inspired High Frequency Flapping Wing Robots,” *Stainless steel*, Vol. 8, 2013, pp. 0–32.

- [66] Dawson, J., Smith, T. J., Elhindi, M., Huang, P. G., Beran, P., and Parker, G., “Flapping Micro Air Vehicle: Wing Fabrication and Analysis,” *51st AIAA Aerospace Sciences Meeting*, AIAA 2013-0760, January 2013.
- [67] Agrawal, A. and Agrawal, S. K., “Design of Bio-inspired Flexible Wings for Flapping-Wing Micro-sized Air Vehicle Applications,” *Advanced Robotics*, Vol. 23, February 2009, pp. 979–1002.
- [68] Mountcastle, A. M. and Daniel, T. L., “Aerodynamic and Functional Consequences of Wing Compliance,” *Experiments in Fluids*, Vol. 46, No. 5, 2009, pp. 1–10873–882.
- [69] *Homefly*, Orlando FL, www.homefly.com (accessed 12/9/16).
- [70] *Horizon Hobby*, horizonhobby.com (accessed 12/9/16).
- [71] *Spektrum Website*, spektrumrc.com (accessed 12/9/16).
- [72] “High-Power Series Lithium Polymer (Li-Po) Batteries,” http://www.e-fliterc.com/ProdInfo/Files/EFL_LiPo_Battery_Guide.pdf (accessed 12/9/16).
- [73] Tsai, B. and Fu, Y., “Design and Aerodynamic Analysis of a Flapping-Wing Micro Aerial Vehicle,” *Aerospace Science and Technology*, Vol. 13, No. 7, 2009, pp. 383–392, ID: 12709638/v13i0007/383_daaaoafmav.
- [74] Han, J., Lee, J., and Kim, D., “Bio-inspired Flapping UAV Design: A University Perspective,” *Health Monitoring of Structural and Biological Systems*, Vol. 7295, 2009, pp. I–1 thru I–12.
- [75] *Linkage Four Bar*, https://en.wikipedia.org/wiki/Four-bar_linkage/media/File:Linkage_four_bar_fixed.svg (accessed 12/9/16).
- [76] Shyy, W., Lian, Y., Tang, J., Viieru, D., and Liu, H., *Aerodynamics of Low Reynolds Number Flyers*, Vol. 22, Cambridge University Press, New York, 2007.
- [77] Oppenheimer, M. W., Sigthorsson, D. O., Weintraub, I. E., Doman, D. B., and Perseghetti, B., “Wing Velocity Control System for Test Body Motion Control Meth-

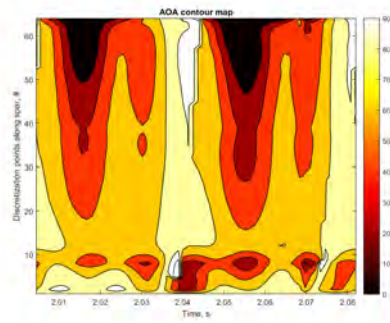
- ods for Flapping Wing MAVs,” *51st AIAA Aerospace Sciences Meeting including the New Horizons Forum and Aerospace Exposition*, AIAA 2013-0332, January 2013.
- [78] Sane, S. P. and Dickinson, M. H., “The Control of Flight Force by a Flapping Wing: Lift and Drag Force Production,” *Journal of Experimental Biology*, Vol. 204, 2001, pp. 2607–2626.
- [79] Oppenheimer, M. W., Sigthorsson, D. O., Weintraub, I. E., Smith, T. J., Dawson, J. C., and Doman, D. B., “Development of a Flapping Wing Mechanism That Can Produce Lift Greater Than Weight,” *AIAA Guidance, Navigation and Control Conference*, AIAA 2013-5106, August 2013.
- [80] *Insect Wing Venation Characterization*, http://commons.wikimedia.org/wiki/File:Venation_of_insect_wing.svg (accessed 12/03/14).
- [81] Johnson, N. F. and Triplehorn, C. A., *Borrow and Delong’s Introduction to the Study of Insects*, Brooks/Cole, 2005.
- [82] Yih-Nen Jeng, P.G. Huang, Y.-C. C., “Decomposition of One-Dimensional Waveform using Iterative Gaussian Diffusive Filtering Methods,” *Proceedings of the Royal Society*, Vol. 464, 2008, pp. 1673–1695.
- [83] Weintraub, I., Smith, T., Oppenheimer, M., Sigthorsson, D., Doman, D., and Huang, G., “Design and Testing of Flexible Wings for Flapping Wing MAVs,” *DCASS 2014 Science Symposium*, 2014.
- [84] Sigthorsson, D. O., Oppenheimer, M. W., Doman, D. B., and Weintraub, I. E., “Wing Flexibility Induced Control Reversal For Flapping Wing Vehicles: Observation and Evaluation,” *AIAA Guidance, Navigation, and Control Conference*, 2017.
- [85] Huang, S. K., *An Experimental Investigation on the Micro Air Vehicle*, Master’s thesis, Wright State University, 2014.

Appendix A

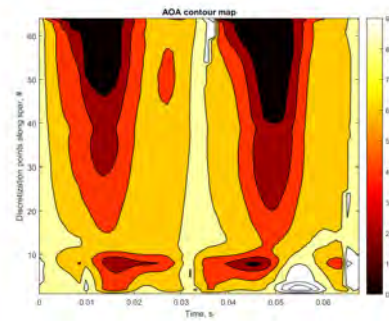
A.1 Wing AOA Tracking Plots

All figures in Section [A.1](#) show one flapping cycle duration along the x-axis and is linear with respect to time. The y-axis begins at the root and moves linearly toward the tip of the wing from the bottom to the top of the y-axis for every figure this section. The darker the color the less AOA that is measured. Black is an AOA of less than 10 deg. White is an AOA greater than 80 deg.

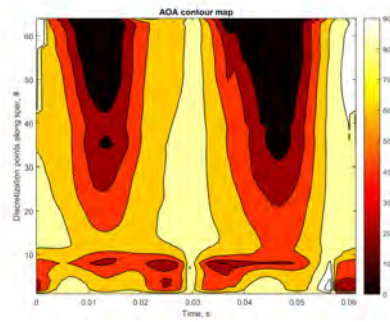
Wing 4E has an obvious dwell in the stroke for both fore and aft strokes at the 19 gram load level. By the 22 gram load it is barely noticeable and immeasurable by the 25 gram load. The 4E wing does get more time in the large AOA but also seems to drive the AOA deeper towards the root of the wing. While this is expected and far from unusual, keep in mind that too large of a deflection cannot make large lift. A very soft wing would make a very low AOA through all of the stroke but would have very limited lift capability.



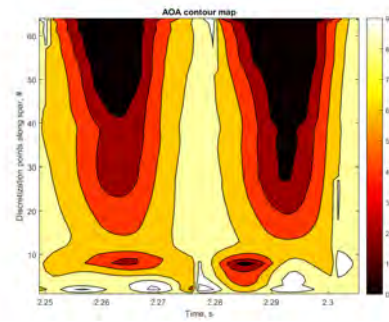
(a) 19.2g Lift



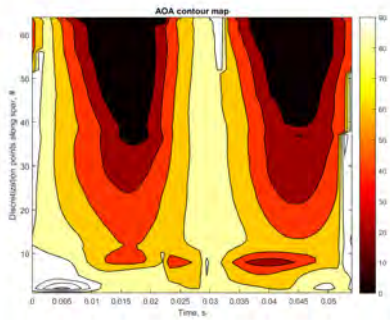
(b) 22.4g Lift



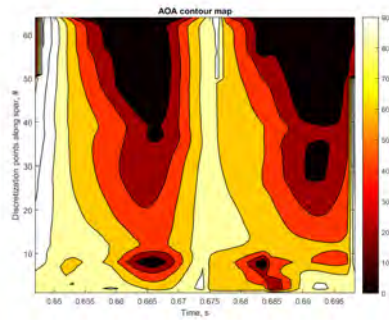
(c) 25.6g Lift



(d) 28.8g Lift



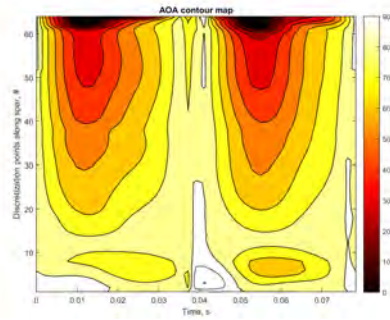
(e) 32.0g Lift



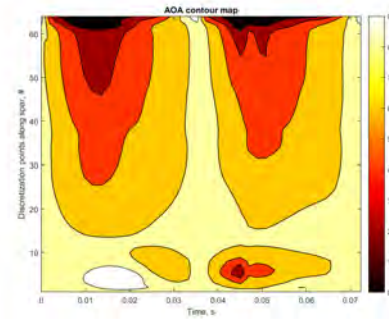
(f) 35.2g Lift

Figure A.1: Wing 4E AOA Mapping

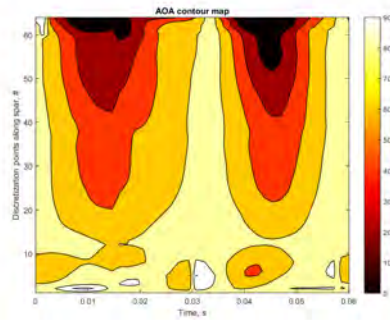
Wing 4F can only lift 32 g before the motor hits saturation. The wing shows no oscillation at any of the measured lift values found in Figure A.2. The wing is too stiff to reach larger lift levels. AOA levels lower than 10 degrees are less prevalent than the 2E, 4E and 2F wings and has similar deflection to that of wing 2D, 4G and 4H.



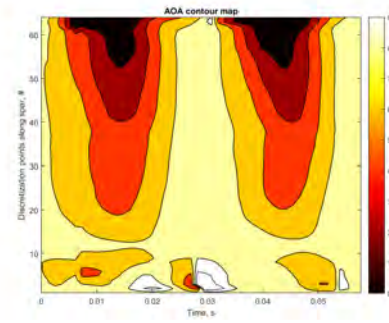
(a) 19.2g Lift



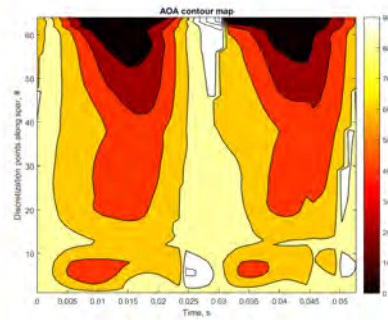
(b) 22.4g Lift



(c) 25.6g Lift



(d) 28.8g Lift



(e) 32.0g Lift

Figure A.2: Wing 4F AOA Mapping

Wing 2G is an example of a stiff wing. Notice the amount of AOA in Figure A.3 less than 20 deg at the low lift levels. The mechanism could not drive the wing above the 28 g lift level. Although not obvious from the shown plots, the leading edge stiffness is significantly larger in this wing. Very little bending is occurring which causes an inertial force that is too large to generate large deflections throughout the entire stroke. Large deflections are quickly dissipated. Even though the wing is flapping faster and the leading edge is stiffer, the wing cannot twist to provide large deflections as a result of the structure.

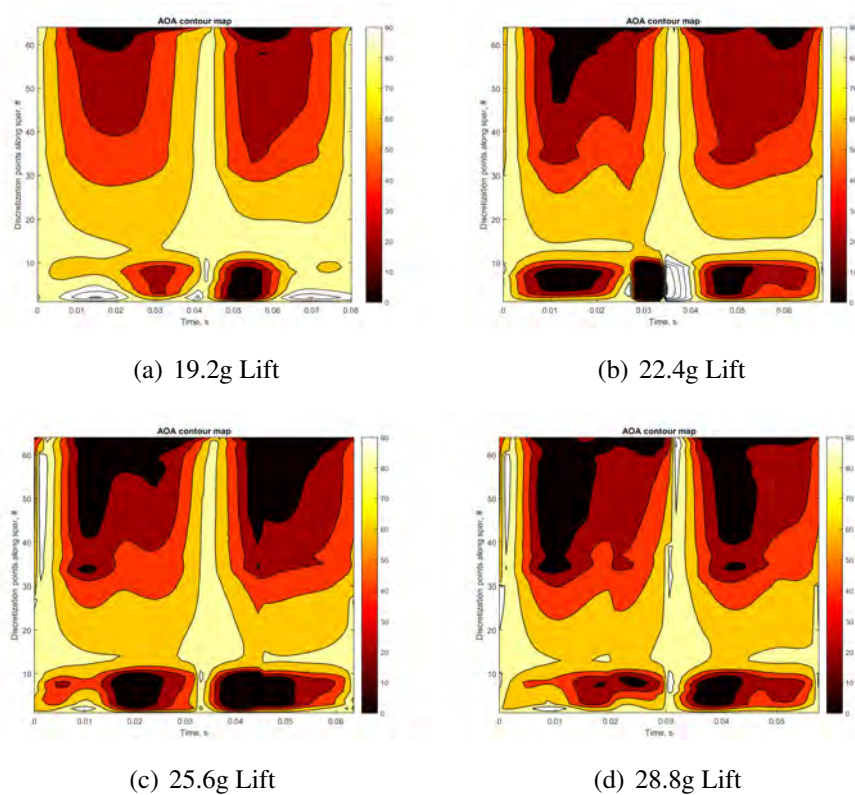
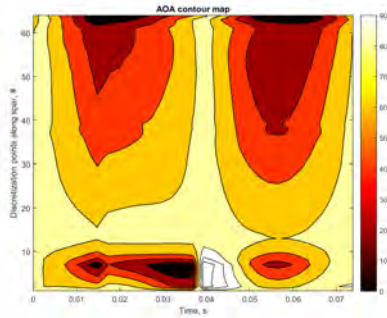
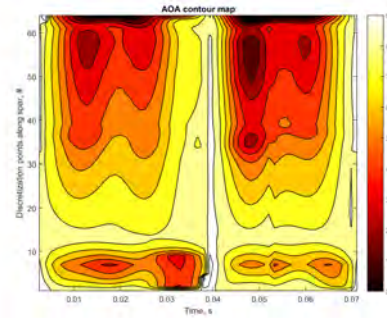


Figure A.3: Wing 2G AOA Mapping

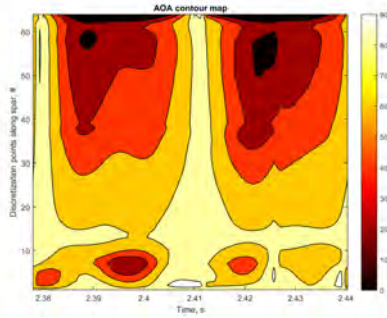
Wing 4G also has a stiff leading edge similar to the 2G wing. The 4G wing was able to lift the 32 g mass with the increased voltage level of 8.4 V. Deflections are relatively low as depicted by Figure A.4.



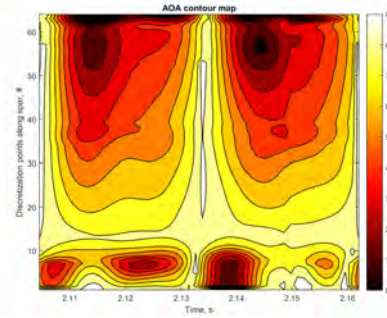
(a) 19.2g Lift



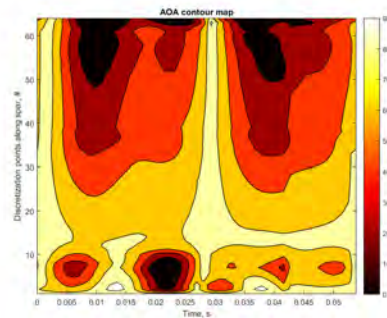
(b) 22.4g Lift



(c) 25.6g Lift



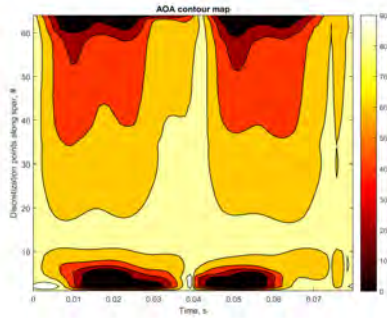
(d) 28.8g Lift



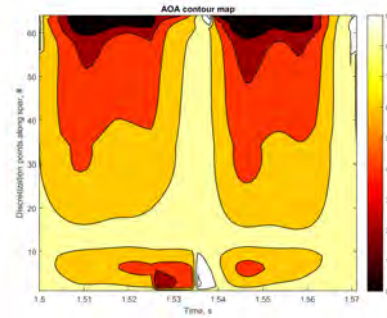
(e) 32.0g Lift

Figure A.4: Wing 4G AOA Mapping

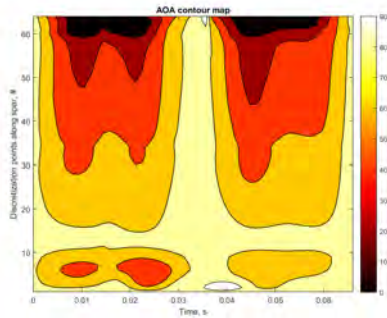
Wing 4H has a stiff leading edge similar to other G and H wings. The AOA is near 45 degrees for the 32 g lift. The frequency while lifting 32 g is 17.9 Hz. This indicates that this wing has the capability to lift more but the stiffness was too large for the mechanism.



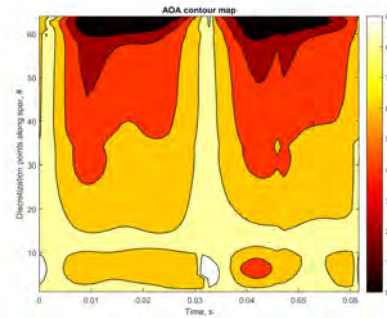
(a) 19.2g Lift



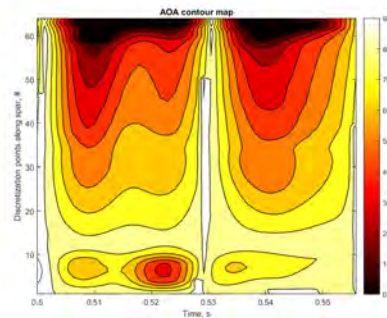
(b) 22.4g Lift



(c) 25.6g Lift



(d) 28.8g Lift

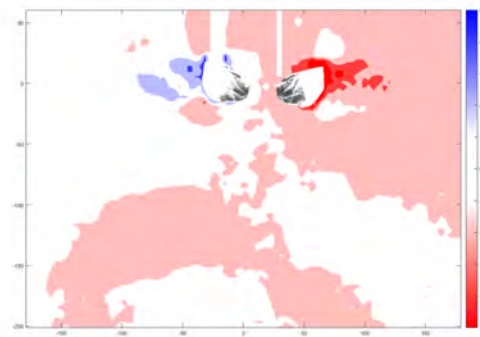


(e) 32.0g Lift

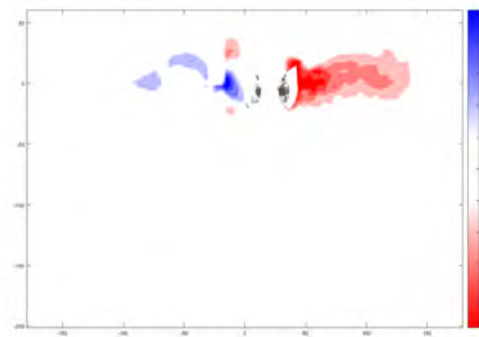
Figure A.5: Wing 4H AOA Mapping

A.2 Wing Velocity Plots

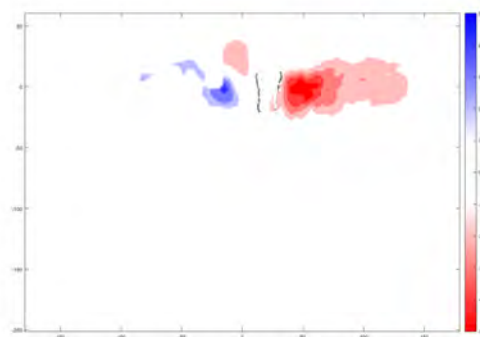
Figure A.6 shows the x velocity map for the 180 degree flapping amplitude at stroke reversal, ranging from -5 (blue) to +5 (red) m/s on the color scale. The extents of the image are equal to those found in Chapter 5 of 368 mm in the x, horizontal direction and 275 mm in the y, vertical direction.



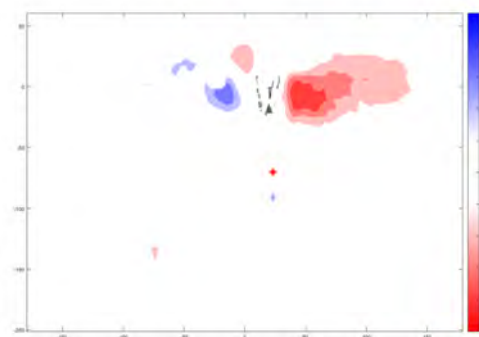
(a)



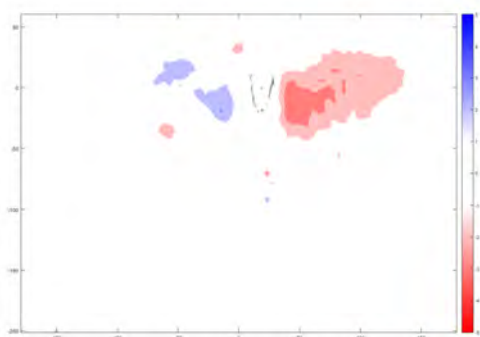
(b)



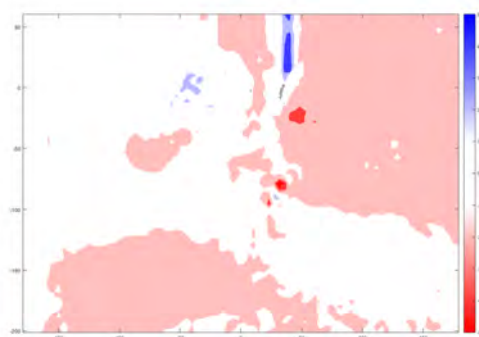
(c)



(d)



(e)



(f)

Figure A.6: PIV 180 Amplitude X Velocity

Figure A.7 shows the x velocity map for the 150 degree flapping amplitude ranging from -5 (blue) to +5 (red) m/s on the color scale. The extents of the image are equal to those found in Chapter 5 of 368 mm in the x, horizontal direction and 275 mm in the y, vertical direction.

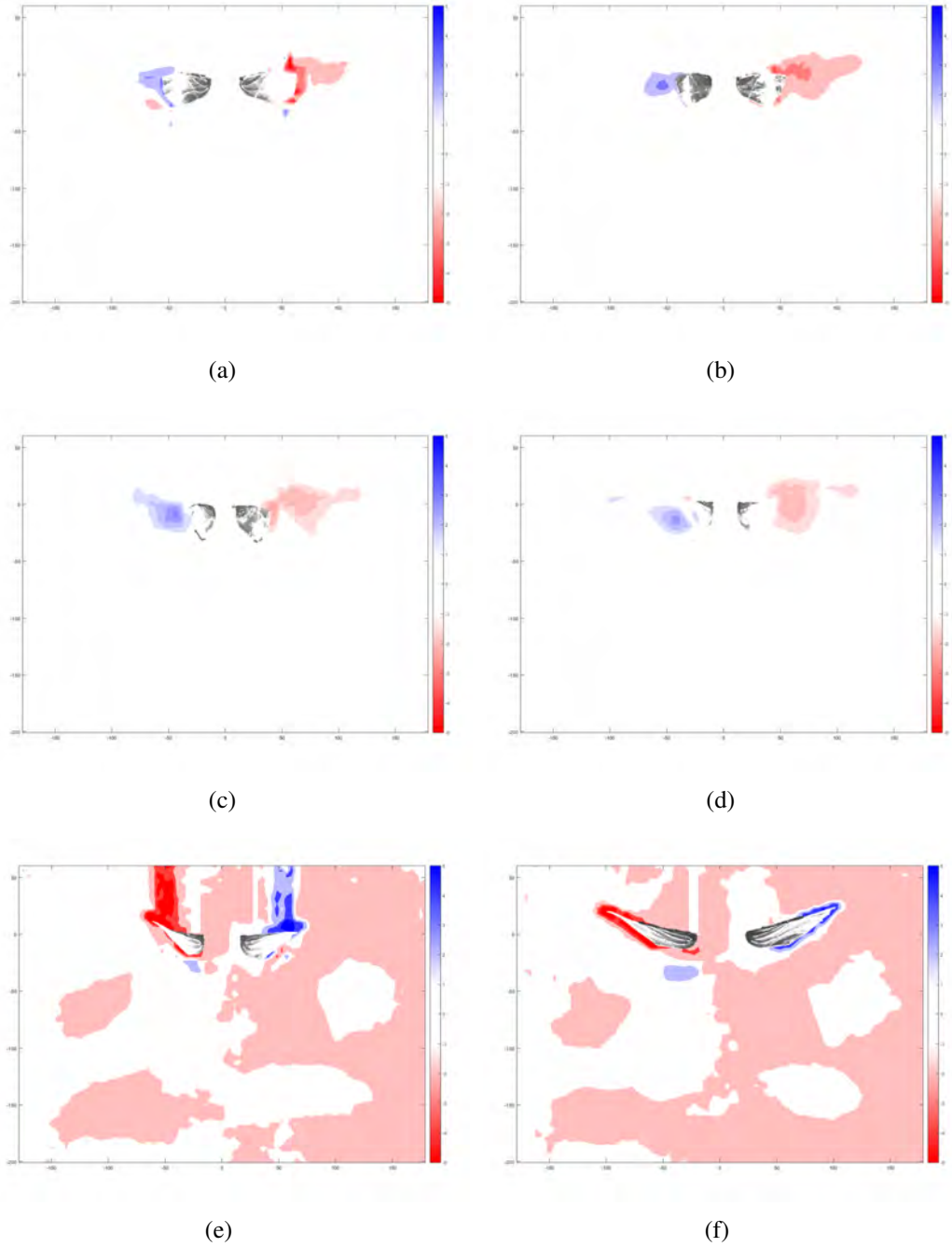


Figure A.7: PIV 150 Amplitude X Velocity

Figure A.8 shows the x velocity map for the 120 degree flapping amplitude ranging from -5 (blue) to +5 (red) m/s on the color scale. The extents of the image are equal to those found in Chapter 5 of 368 mm in the x, horizontal direction and 275 mm in the y, vertical direction.

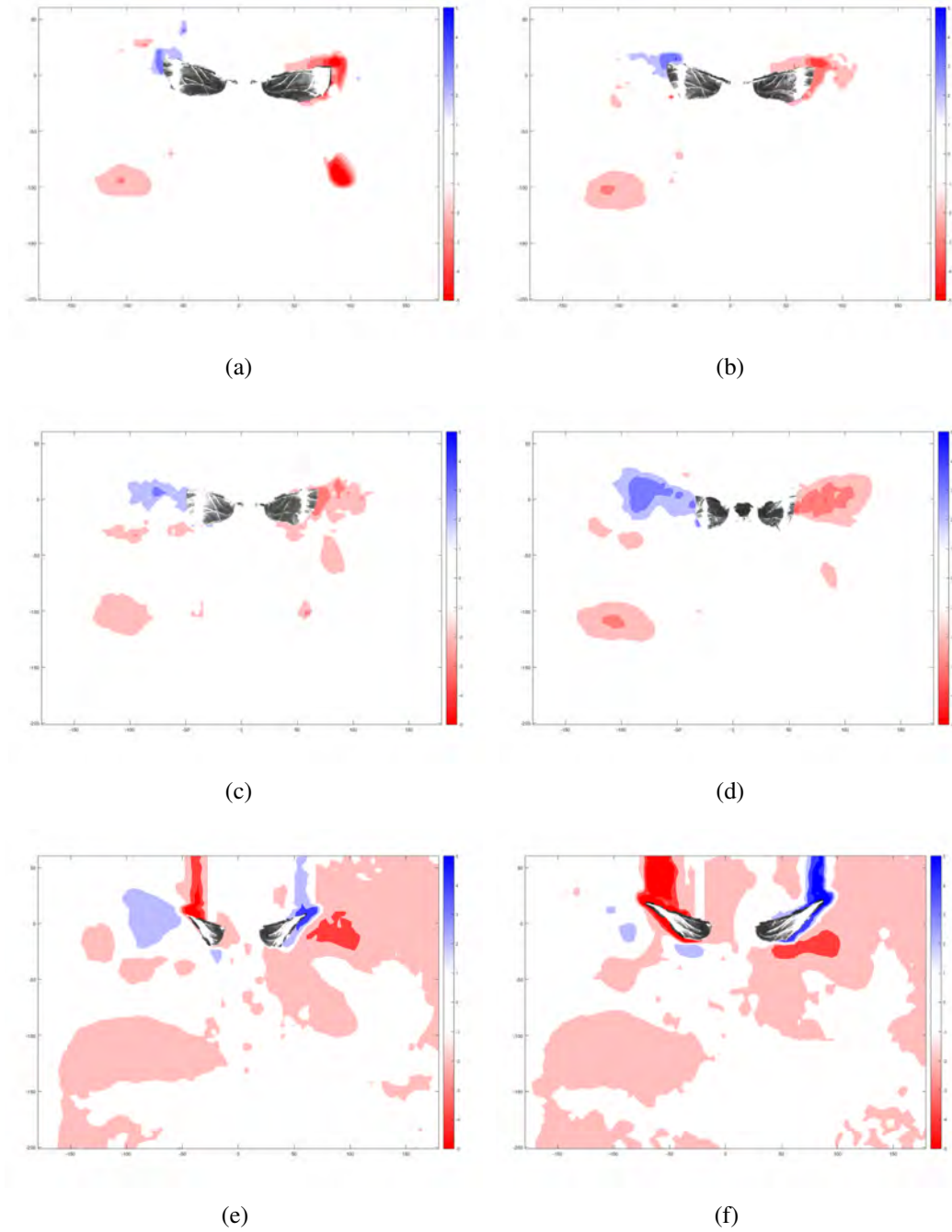


Figure A.8: PIV 120 Amplitude X Velocity

Figure A.9 shows the x velocity map for the 180 degree flapping amplitude at mid-stroke ranging from -5 (blue) to +5 (red) m/s on the color scale. The extents of the image are equal to those found in Chapter 5 of 368 mm in the x, horizontal direction and 275 mm in the y, vertical direction.

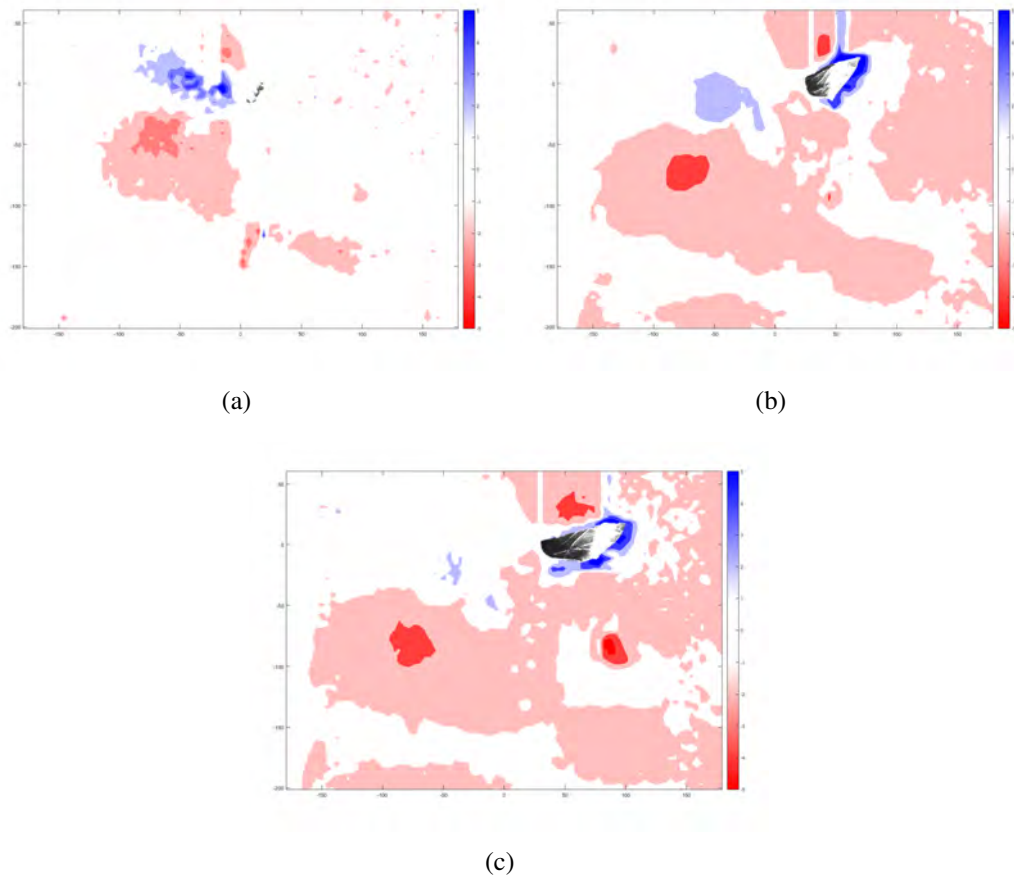


Figure A.9: PIV Mid-Stroke 180 Amplitude X Velocity

Figure A.10 shows the x velocity map for the 150 degree flapping amplitude at mid-stroke ranging from -5 (blue) to +5 (red) m/s on the color scale. The extents of the image are equal to those found in Chapter 5 of 368 mm in the x, horizontal direction and 275 mm in the y, vertical direction.

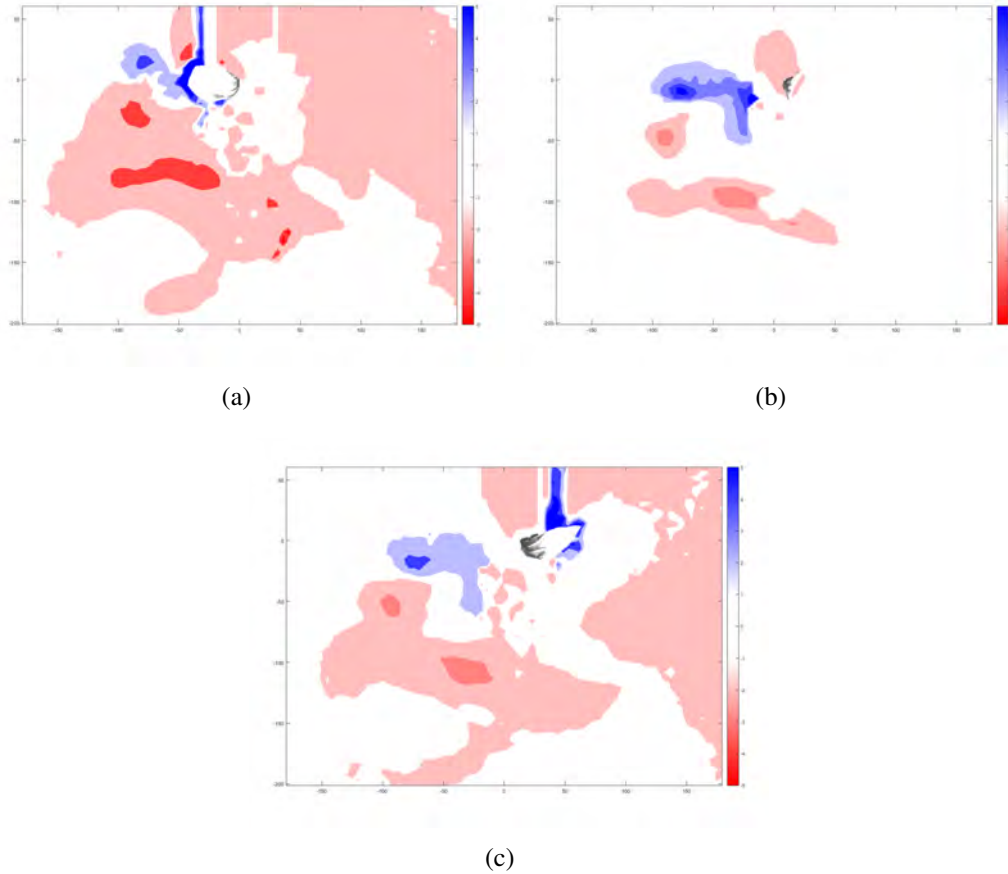


Figure A.10: PIV Mid-Stroke 150 Amplitude X Velocity

Figure A.11 shows the x velocity map for the 120 degree flapping amplitude at mid-stroke ranging from -5 (blue) to +5 (red) m/s on the color scale. The extents of the image are equal to those found in Chapter 5 of 368 mm in the x, horizontal direction and 275 mm in the y, vertical direction.

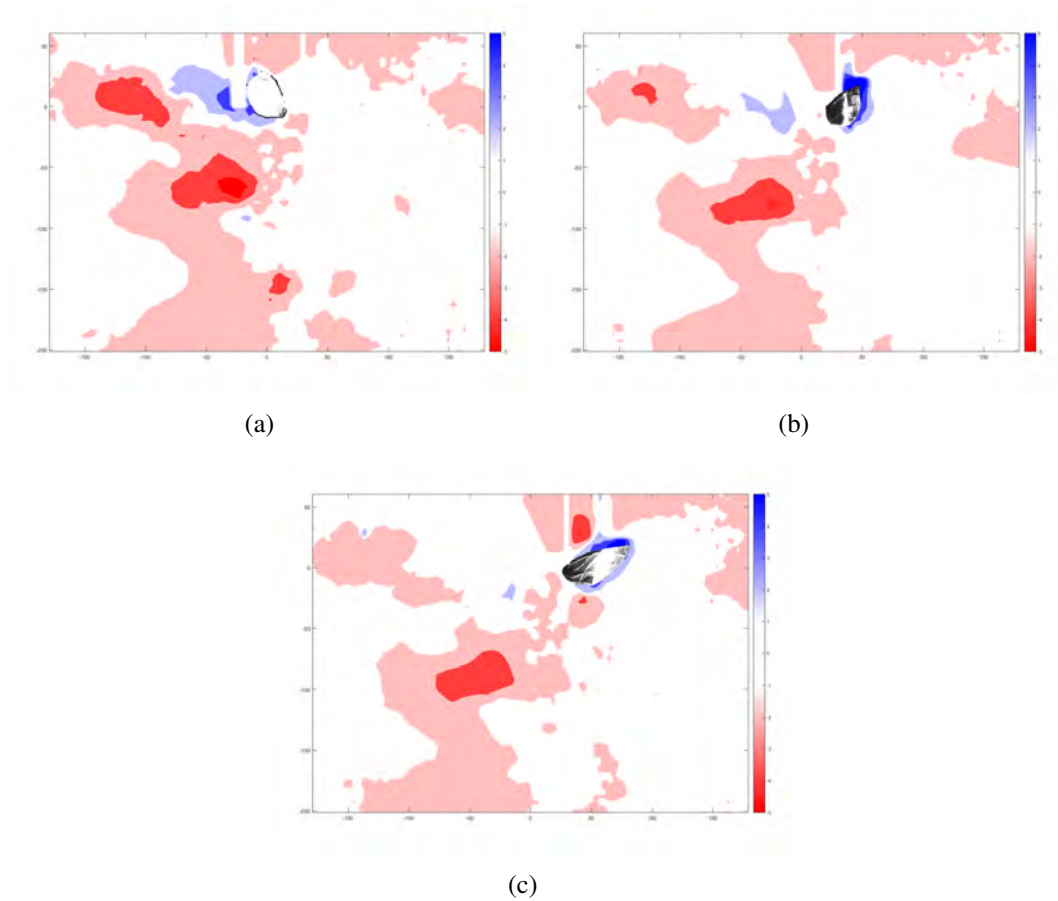


Figure A.11: PIV Mid-Stroke 120 Amplitude X Velocity

Appendix B

B.1 Four-Bar MATLAB Code

```
1  % Todd Smith
2  % 10-31-2013
3
4  clc
5  clear all
6  close all
7
8  % This program is intended to plot the four bar kinematics of various
9  % transmission linkages
10 GearAmp = 242/20; %242/20    this is the bevel gear set ratio ...
    (wing angle amplification)
11
12 crank = 2.5;      %mm      2.50
13 rocker = 21.8;    %mm      21.80
14 crod = 15.6;      %mm      15.60
15 ground = 20.523; %mm      20.523
16
17 baseangle = 107;  %angle to upright the mechanism about the ...
    rocker pivot point in degrees
18
19 for i = 1:360
20
21     thetacrank(i) = i-1;
```

```

22
23 if thetacrank(i) == 0
24
25     l1 = ground - crank;
26     l2 = crod;
27     l3 = rocker;
28     rockerangle(i) = acosd((l1^2+l3^2-l2^2)/(2*l1*l3));
29
30 %%The following calculations are for plotting
31     crankptx(i) = ground*cosd(baseangle);
32     crankpty(i) = ground*sind(baseangle);
33     couplerptx(i) = l1*cosd(baseangle);
34     couplerpty(i) = l1*sind(baseangle);
35     rockerptx(i) = rocker*cosd(baseangle-rockerangle(i));
36     rockerpty(i) = rocker*sind(baseangle-rockerangle(i));
37
38
39 elseif thetacrank(i) < 180
40
41     lprime = ...
42         sqrt(ground^2+crank^2-2*ground*crank*cosd(thetacrank(i)));
43     angle1 = asind(crank/lprime*sind(thetacrank(i)));
44     angle2 = acosd((lprime^2-crod^2+rocker^2)/(2*rocker*lprime));
45     rockerangle(i) = angle1+angle2;
46
47 %%The following calculations are for plotting
48     crankptx(i) = ground*cosd(baseangle);
49     crankpty(i) = ground*sind(baseangle);
50     couplerptx(i) = lprime*cosd(baseangle-angle1);
51     couplerpty(i) = lprime*sind(baseangle-angle1);
52     rockerptx(i) = rocker*cosd(baseangle-rockerangle(i));
53     rockerpty(i) = rocker*sind(baseangle-rockerangle(i));
54
55
56 elseif thetacrank(i) == 180
57
58     l1 = ground + crank;

```



```

57     l2 = crod;
58     l3 = rocker;
59     rockerangle(i) = acosd((l1^2+l3^2-l2^2)/(2*l1*l3));
60
61     %%The following calculations are for plotting
62     crankptx(i) = ground*cosd(baseangle);
63     crankpty(i) = ground*sind(baseangle);
64     couplerptx(i) = l1*cosd(baseangle);
65     couplerpty(i) = l1*sind(baseangle);
66     rockerptx(i) = rocker*cosd(baseangle-rockerangle(i));
67     rockerpty(i) = rocker*sind(baseangle-rockerangle(i));
68
69     elseif thetacrank(i) < 360
70
71         theta(i) = 360-thetacrank(i);
72         lprime = sqrt(ground^2+crank^2-2*ground*crank*cosd(theta(i)));
73         angle1 = asind(crank/lprime*sind(theta(i)));
74         angle2 = acosd((lprime^2-crod^2+rocker^2)/(2*rocker*lprime));
75         rockerangle(i) = angle2-angle1;
76
77         %%The following calculations are for plotting
78         crankptx(i) = ground*cosd(baseangle);
79         crankpty(i) = ground*sind(baseangle);
80         couplerptx(i) = lprime*cosd(baseangle+angle1);
81         couplerpty(i) = lprime*sind(baseangle+angle1);
82         rockerptx(i) = rocker*cosd(baseangle-rockerangle(i));
83         rockerpty(i) = rocker*sind(baseangle-rockerangle(i));
84     end
85
86     xpts(:,i) = [0 crankptx(i) couplerptx(i) rockerptx(i) 0];
87     ypts(:,i) = [0 crankpty(i) couplerpty(i) rockerpty(i) 0];
88
89     end
90     figure(1)
91     hold on
92     for i = 1:10:360

```

```

93 plot(xpts(1:2,i),ypts(1:2,i),'g')
94 plot(xpts(2:3,i),ypts(2:3,i),'b')
95 plot(xpts(3:4,i),ypts(3:4,i),'r')
96 plot(xpts(4:5,i),ypts(4:5,i),'k')
97 end
98 axis equal
99 axis([-20 15 -9 31])
100 %axis([-15 15 -2 27])
101 title('Four Bar Stepwise Geometric Layout')
102 xlabel('Distance (mm)')
103 ylabel('Distance (mm)')
104
105
106 figure(2)
107 plot(thetacrank,rockerangle)
108 title('Crank Angle vs. Rocker Angle')
109 % Normalize the rocker angle
110
111 midpoint = (max(rockerangle)+min(rockerangle))/2;
112
113 rockerangleM = rockerangle-midpoint;
114
115 figure(3)
116 plot(thetacrank,rockerangleM)
117 title('Crank Angle vs. Shifted Rocker Angle')
118
119
120 min(rockerangleM);
121 max(rockerangleM);
122
123 % Convert the kinematics to wing angle
124
125 wingangle = rockerangleM*GearAmp;
126
127 figure(4)
128 plot(thetacrank,wingangle)

```

```

129 title('Crank Angle vs. Wing Angle')
130
131 max(wingangle)
132 min(wingangle)
133
134 for i = 1:360
135
136 if i < 10
137 winganglezero(i) = wingangle(351+i);
138 crankanglezero(i) = thetacrank(351+i);
139 else
140 winganglezero(i) = wingangle(i-9);
141 crankanglezero(i) = thetacrank(i-9);
142 end
143 end
144
145 x = [180, 180];
146 y = [-90, 90];
147 x1 = [0, 360];
148 y1 = [0, 0];
149
150 figure(5)
151 plot(winganglezero)
152 hold on
153 plot(x,y,'r',x1,y1,'r')
154 title('Crank Angle vs. Wing Angle')
155 xlabel('Crank Angle (deg)')
156 ylabel('Wing Position (deg)')
157
158 maxwingang = max(winganglezero)
159 for i = 1:360
160 normwingangzero(i) = winganglezero(i)/maxwingang;
161 end
162
163 x = [180, 180];
164 y = [-1, 1];

```

```

165 x1 = [0,360];
166 y1 = [0,0];
167
168 figure(6)
169 plot(normwingangzero)
170 hold on
171 plot(x,y,'r',x1,y1,'r')
172 title('Crank Angle vs. Normalize Wing Angle')
173 axis([0 360 -1 1])
174 xlabel('Crank Angle (deg)')
175 ylabel('Normalized Wing Position')
176
177 % Now lets calculate some idealized velocities
178
179 hz = 11; %enter the wing frequency%%%%%%%%%%%%%%%%%%%%%%%%
180
181 crankvelocity = hz*360; %in deg/s
182
183 dt = 1/crankvelocity; %s/deg
184
185 % because the step was 1deg dt is in sec per deg
186
187 for i = 1:359
188 wingvelocity(i) = (winganglezero(i+1)-winganglezero(i))/dt; %deg/s
189 end
190
191 figure(7)
192 plot(wingvelocity)
193 title('Crank Angle vs. Wing Velocity (deg/s)')
194 xlabel('Crank Angle (deg)')
195 ylabel('Wing Velocity (deg/s)')
196
197 for i = 1: 358
198     wingacceleration(i) = (wingvelocity(i+1)-wingvelocity(i))/dt; ...
        %deg/s/s.
199 end

```

```

200
201 maxacc = max(abs(wingacceleration))
202 meanacc = mean(abs(wingacceleration))
203
204 for i = 1: 357
205     wingaccnorm(i) = abs(wingacceleration(i))/maxacc;
206 end
207
208 hold off
209 figure(8)
210 plot(wingacceleration)
211 title('Crank Angle vs. Wing Acceleration (deg/s^2)')
212 xlabel('Crank Angle (deg)')
213 ylabel('Wing Angular Acceleration (deg/s^2)')
214
215 figure(12)
216 plot(wingaccnorm)
217 title('Crank Angle vs. Normalize Angular Wing Acceleration')
218 xlabel('Crank Angle (deg)')
219 ylabel('Normalized Wing Angular Acceleration')
220
221 for i = 1:359
222     if i < 92
223         wingvelocityzero(i) = wingvelocity(268+i);
224     else
225         wingvelocityzero(i) = wingvelocity(i-91);
226     end
227 end
228
229 maxwingvel = max(wingvelocityzero);
230 for i = 1:359
231     normwingvel(i) = wingvelocityzero(i)/maxwingvel;
232 end
233
234 figure(11)
235 plot(abs(normwingvel))

```

```

236 title('Crank Angle vs. Normalized Wing Velocity')
237 xlabel('Crank Angle (deg)')
238 ylabel('Normalized Angular Wing Velocity')
239
240 figure(9)
241 plot(abs(wingvelocityzero))
242 title('Crank Angle vs. Absolute Wing Velocity')
243 xlabel('Crank Angle (deg)')
244 ylabel('Absolute Wing Velocity (deg/s)')
245
246 figure(10)
247 plot(abs(wingacceleration))
248 title('Crank Angle vs. Absolute Wing Acceleration (deg/s^2)')
249 xlabel('Crank Angle (deg)')
250 ylabel('Absolute Wing Angular Acceleration (deg/s^2)')
251 XMIN = 0;
252 XMAX = 400;
253 YMIN = 0;
254 YMAX = 800000;
255
256 AXIS([XMIN XMAX YMIN YMAX]);

```